Astronomy Reports, Vol. 48, No. 10, 2004, pp. 787–794. Translated from Astronomicheskiĭ Zhurnal, Vol. 81, No. 10, 2004, pp. 867–875.

Galactic Systems Against the Background of the Cosmic Vacuum: Structure and Evolution of the Zero-Acceleration Surface

V. P. Dolgachev[1], L. M. Domozhilova[1], and A. D. Chernin[1,2,3]

[1] *Sternberg Astronomical Institute, Universitetskiĭ pr. 13, 119992 Moscow, Russia*

[2] *Tuorla Observatory, Turku University, Turku, Finland*

[3] *University of Oula, Finland*

Received January 15, 2004; in final form, March 15, 2004

Abstract—The structure and evolution of the zero-acceleration surface around wide triple systems of galaxies are studied in detail. (The zero-acceleration surface is the boundary separating regions in which (i) the Newtonian gravitational attraction of the galactic matter and (ii) the Einsteinian universal repulsion of the cosmic vacuum dominate.) For a typical system, this surface is spherical in shape and several megaparsecs in size, and remains nearly unchanged throughout the lifetime of the system. The concept of a boundary surface can also be extended to systems on the largest possible scales, and its general properties are discussed in relation to clusters, superclusters, and voids. © *2004 MAIK "Nauka/Interperiodica".*

1. INTRODUCTION

The zero-acceleration surface is a new concept in cosmology and extragalactic astronomy that arises [1–4] due to the recent discovery of the cosmic vacuum energy [5, 6]. This surface is the boundary between regions of space with opposite signs for their gravitational fields: on one side, "ordinary" Newtonian gravitation created by the mutual attraction of the matter dominates, while on the other side, the Einsteinian "universal repulsion" of the cosmic vacuum dominates. For example, suppose we consider a sphere of matter with mass M and radius R_0 against the background of the vacuum; the zero-acceleration surface is then a sphere with some radius $R_V > R_0$, within which the mutual attraction of the mass M dominates, and outside of which the repulsive field of the cosmic vacuum dominates. The net attractive force inside this spherical surface is directed toward the center of the sphere of matter, while the net repulsive force outside the surface is directed away from the center. The acceleration at the surface itself is therefore equal to zero, so that this can be considered a "zero-attraction" surface.

The concept of a zero-acceleration surface formulated in [1–4] for the vicinity of the Local Group of galaxies can be extended in a natural way to other groups of galaxies and to clusters and superclusters of galaxies, as well as to voids.

The cosmic vacuum, discovered in the analysis of observations of distant supernovae [5, 6], forms an ideal uniform medium whose density has the same numerical value in any reference frame. In general relativity theory, it is described by Einstein's cosmological constant. According to the most recent accumulated observational data on the cosmological expansion of the Universe, the anisotropy of the cosmic-background radiation, the structure and dynamics of large-scale structures in the Universe, etc. (see the recent review [7]), the density of the cosmic vacuum comprises approximately 70% of the total density of the Universe, and therefore exceeds by more than a factor of two the total density of all other forms of cosmic energy, including that of invisible dark matter. This contrast is made even more dramatic by the fact that, according to general-relativity theory, the effective gravitating density is represented by the sum $\rho_{eff} = \rho + 3p$, where p is the pressure of the medium. For a vacuum, $p_V = -\rho_V$, so that its effective density is $\rho_{eff} = -2\rho_V$, or twice as large in magnitude as its density. The effective density of the vacuum is negative—this means that it creates a universal repulsion. For example, two test particles in a vacuum whose initial relative velocity is zero will begin to move away from each other with an exponentially growing speed under the action of the vacuum.

The dominance of the repulsion of the cosmic vacuum over the attraction of nonvacuum forms of energy is manifest in the observed Universe on large cosmological scales of hundreds or thousands of Mpc, where the universal repulsion of the vacuum causes galaxies and systems of galaxies to accelerate away from each other. The role of the vacuum is also substantial on comparatively small spatial scales, where the possibility of a boundary between regions with opposite signs of attraction

1063-7729/04/4810-0787$26.00

arises. For example, the Local Group of galaxies is entirely contained within a closed, nearly spherical zero-radial-acceleration surface located no more than 2 Mpc from the barycenter of the group [4]. This surface encloses a system of galaxies that is bound by the mutual gravitation of its members, while directly outside the surface begins the local Hubble flow, in which galaxies move in the repulsive force field of the cosmic vacuum.

The main bodies in the Local Group are our own Galaxy and the Andromeda Galaxy, which are separated by a distance of 0.7 Mpc and approach each other with a relative speed of 120 km/s. This wide system is in a state of gravitational collapse, which began after its isolation from the general cosmological expansion 12–13 Gyr ago. The dynamics of the collapse are governed by the attraction of the nonvacuum matter of the system—both the dark matter (hidden mass) and the baryonic matter of the galaxies. The gravitational potential well in which the collapse of the Local Group is occurring has a finite radial size, which determines the zero-radial-acceleration surface.

In our earlier study [4], we presented an exact solution for the structure and evolution of the zero-radial-acceleration surface around the Local Group. This solution showed that the cross section of this surface in its symmetry plane forms an asymmetric oval that can be contained within two circles with radii of 1.4 and 1.8 Mpc at the current epoch, or radii of 2 and 1.7 Mpc 12.5 Gyr ago. The common center of these circles lies at the barycenter of the system. This demonstrates that the shape of this critical surface is not very different from spherical, and that it has not varied strongly over the lifetime of the Local Group (three-quarters of the lifetime of the Universe).

These two new circumstances—the near sphericity and near stationarity of the dynamical background surrounding the Local Group—together with the dominance of the antigravity of the cosmic vacuum in this region, have probably determined the structure and kinematics of the local Hubble flow on scales from 2 to 3–9 Mpc. It is possible that this flow itself arose due to the ejection (or "evaporation") of dwarf galaxies from within the volume of the Local group into the region beyond the zero-radial-acceleration surface [8]. If they had nonnegative radial velocities when they crossed the critical surface ($v \geq 0$), small bodies could then acquire effective radial accelerations due to the antigravity of the cosmic vacuum beyond the surface.

Our work extends our analysis to relatives of the Local Group—wide triple systems of galaxies. Like the Local Group, these systems have characteristic sizes of about 1 Mpc and relative speeds of about 100 km/s. They are also in a state of collapse, and have crossing times, on average, comparable to their ages. We also briefly discuss the zero-acceleration surfaces around clusters and superclusters of galaxies. Section 2 presents the main observational data on wide triple systems of galaxies. Section 3 presents an exact solution for the structure and evolution of the zero-acceleration surfaces of typical systems of this type. In Section 4, we discuss the general properties of the critical surfaces of systems of galaxies of various types and masses—from groups to clusters, superclusters, and voids.

2. WIDE TRIPLE SYSTEMS OF GALAXIES AND MODELS FOR THESE SYSTEMS

The first (and thus far only) list of wide triple systems of galaxies was published in [9] nearly ten years ago. This list contains data on 108 systems, 38 of which are "probable physical systems" according to the statistical criterion of Anosova [10]. The characteristic sizes of these systems ($\simeq$1 Mpc) are much larger than the sizes of the compact triple galaxies studied by Karachentsev and his colleagues at the Special Astrophysical Observatory ($\simeq$0.05 Mpc) [11]. This is the sense in which we have named systems in our list "wide" and the triplets of Karachentsev "compact." A detailed comparative analysis of wide and compact triple galaxies is given in the review [12]. We restrict our description here to a brief summary of information about wide systems and dynamical models for such systems.

A dynamical system consisting of three bodies is characterized by the following main parameters:

—the mean radial velocity

$$\langle V\rangle = \sum V_k/3, \quad k = 1,2,3, \tag{1}$$

where V_k is the radial velocity of a component of the triple corrected for the solar motion;

—the mean square projection of the velocity of a triple component after subtraction of the mean velocity

$$\sigma_r = [(1/3)\sum (V_k - \langle V\rangle)^2]^{1/2}, \quad k = 1,2,3; \tag{2}$$

—the projection of the distance betwen two galaxies in the system

$$R_{ik} = x_{ik}\langle V\rangle H^{-1}, \tag{3}$$

where x_{ik} is the angular distance between the components and H is the Hubble constant;

—the mean harmonic distance (in projection) between the components

$$r_h = (1/3)\sum R_{ik}^{-1}, \quad i,k = 1,2,3; \quad i \neq k. \tag{4}$$

These data can be used to define the dimensionless crossing time normalized to the Hubble time (H^{-1}):

$$\tau = 2H(r_h/\sigma_r). \quad (5)$$

The projected quantities σ_r and r_h are statistically related to the three-dimensional parameters σ and r by the relations

$$\sigma = \sqrt{3}\sigma_r, \quad r = (2/\sqrt{3})r_h. \quad (6)$$

The numerical values for these characteristic quantities for the sample of 38 probable physical systems are (the Hubble constant is normalized so that $h = H/75$ km s^{-1} Mpc^{-1}):

$$\sigma_r = 84 \text{ km/s}, \quad r_h = 556h^{-1} \text{ kpc}, \quad \tau = 0.96,$$
$$\sigma = 143 \text{ km/s}, \quad r = 668h^{-1}.$$

The wide triple systems (like the compact systems) are dominated by giant galaxies with baryonic masses of $M_h = (1-2) \times 10^{11}\ M_\odot$, comparable to the baryonic mass of the two main galaxies of the Local Group. The mass of dark matter appreciably exceeds the baryonic mass. According to our models [13–15], the total mass of a typical triple system is close to $10^{12}\ M_\odot$.

The models of [13–15] fall into two classes. In one, the dark nonbaryonic matter is assumed to be spread throughout the volume of the system, forming a spherically symmetrical common halo obeying an isothermal density law. In the other class of models, the dark matter is assumed to be concentrated in individual spherical halos around the member galaxies of the system, with the size of these halos being about an order of magnitude smaller than the typical distances between the centers of the galaxies. Both types of models reproduce the observed kinematic characteristics of the probable physical systems roughly equally well. The two types of model can be distinguished based on X-ray observations of these systems [15]. At present, we can only suggest that the close analogy between these wide systems and the Local Group (where the dark matter is located primarily in the individual coronas of the two main galaxies) gives some preference to models with individual dark halos. Below, we consider the zero-acceleration surfaces for both classes of models.

3. THE ZERO-RADIAL-ACCELERATION SURFACE

The solution for the zero-acceleration surface is simple in the case of models with a common spherical halo. If the mass of the system is M and its size is R_0, we have for a radial trajectory at a distance $r > R_0$ from the barycenter of the system

$$\ddot{R} = -GM/r^2 + \frac{8\pi G}{3}\rho_V r, \quad (7)$$

where ρ_V is the density of the vacuum and G is the gravitational constant. We can see that the acceleration vanishes on a sphere with radius

$$r = R_V = [3M/(8\pi\rho_V)]^{1/3}. \quad (8)$$

For the typical mass for models of this type, $M = 9 \times 10^{12}\ M_\odot$, and a density $\rho_V = 4 \times 10^{-30}$ g/cm^3, we obtain $R_V \simeq 2.8$ Mpc. We can see that this radius is close to the size of the zero-acceleration surface of the Local Group (see Section 1).

In models with individual galactic halos, there is no overall spherical symmetry, making the solution much more complicated. We will find this solution by considering the motion of a passive gravitating body (this may be a dwarf galaxy, for example) P in a cosmic vacuum. The dynamical picture on the scales of triple systems of galaxies is then described by two quantities: the repulsive force created by the vacuum at some distance r from the barycenter of the system and the attractive force created by the three masses in the system at this same location. In the terminology of celestial mechanics, we have in this case a restricted four-body problem—against the background of the antigravity of the vacuum (this problem is not enountered among the celestial-mechanics problems in [4]).

Let M_i $(i = 1, 2, 3)$ be the masses of the system's components, and the repulsive force of the vacuum at some distance r from the barycenter be given, as above, by the expression

$$F_V = \frac{8}{3}\pi G\rho_V r. \quad (9)$$

As usual, we take the Newtonian gravitational force due to the masses M_1, M_2, and M_3 to have the form

$$F_i = G\frac{M_i}{r_i^2} \quad (i = 1, 2, 3), \quad (10)$$

where $r_i^2 = (x - x_i)^2 + (y - y_i)^2 + (z - z_i)^2$; x_i, y_i, z_i are the barycentric coordinates of the body M_i and x, y, z are the barycentric coordinates of the body P. The force field in which the four-body system moves then has the form

$$F(x, y, z) = G\left(\frac{8}{3}\pi\rho_V r + \sum_{i=1}^{3}\frac{M_i}{r_i^2}\right). \quad (11)$$

This force field has the force function

$$V(x, y, z) = G\left(\frac{4}{3}\pi\rho_V r^2 + \sum_{i=1}^{3}\frac{M_i}{r_i}\right). \quad (12)$$

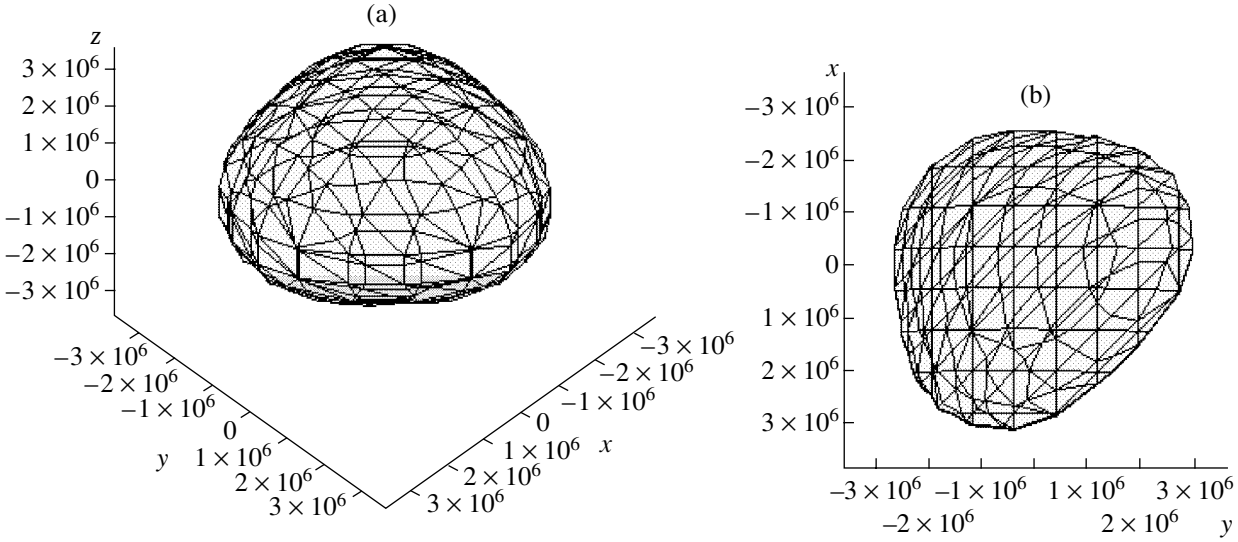

Fig. 1. Two views of the zero-acceleration surface for model A at the initial time.

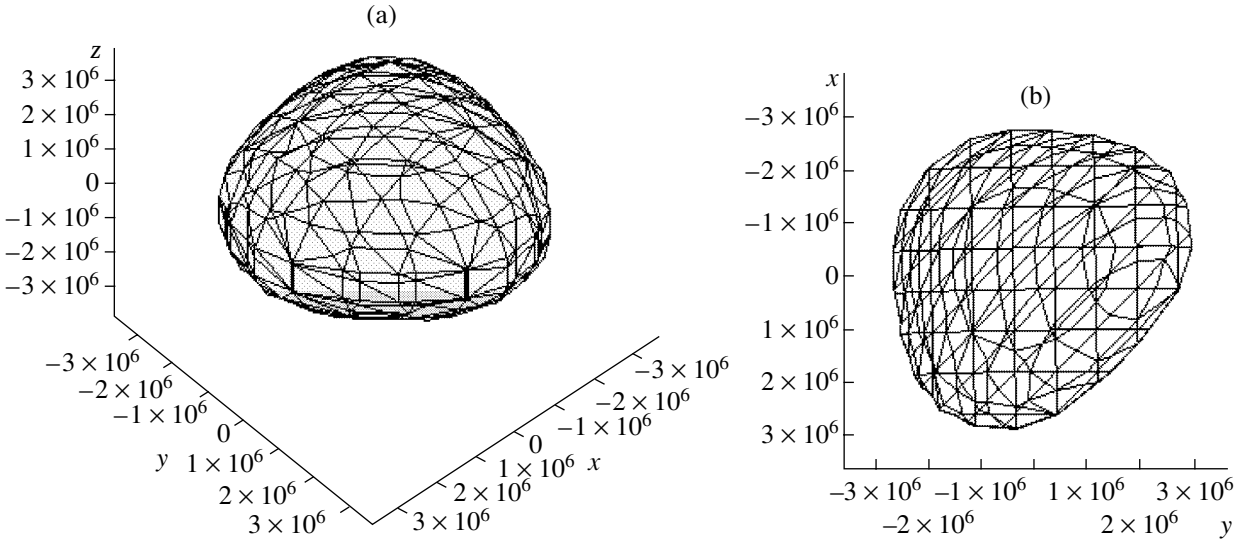

Fig. 2. Two views of the zero-acceleration surface for model A at the current time.

The equations of motion of the dwarf galaxy (test body) in this gravitational field have the form

$$\left.\begin{aligned}\frac{d^2x}{dt^2} &= \frac{\partial U}{\partial x}\\ \frac{d^2y}{dt^2} &= \frac{\partial U}{\partial y}\\ \frac{d^2z}{dt^2} &= \frac{\partial U}{\partial z}\end{aligned}\right\}. \qquad (13)$$

To determine the boundaries of regions of space $Oxyz$ in which the motion has different dynamical properties, we obtain the equation for the surface on which the radial component of the acceleration of the force field is zero. In other words, we must obtain the equation for the geometrical locus of points for which the scalar product of the acceleration vector and the radius vector of the test particle is equal to zero. If we take the coordinates of the vector acceleration to be $\left\{\frac{d^2x}{dt^2}, \frac{d^2y}{dt^2}, \frac{d^2z}{dt^2}\right\}$ and the coordinates of the radius vector to be x, y, the scalar product of the two can be expressed

$$x\frac{d^2x}{dt^2} + y\frac{d^2y}{dt^2} + z\frac{d^2z}{dt^2} = 0. \qquad (14)$$

Note that the quantities $\frac{d^2x}{dt^2}$, $\frac{d^2y}{dt^2}$, and $\frac{d^2z}{dt^2}$ in this relation are given by the right-hand sides of our sys-

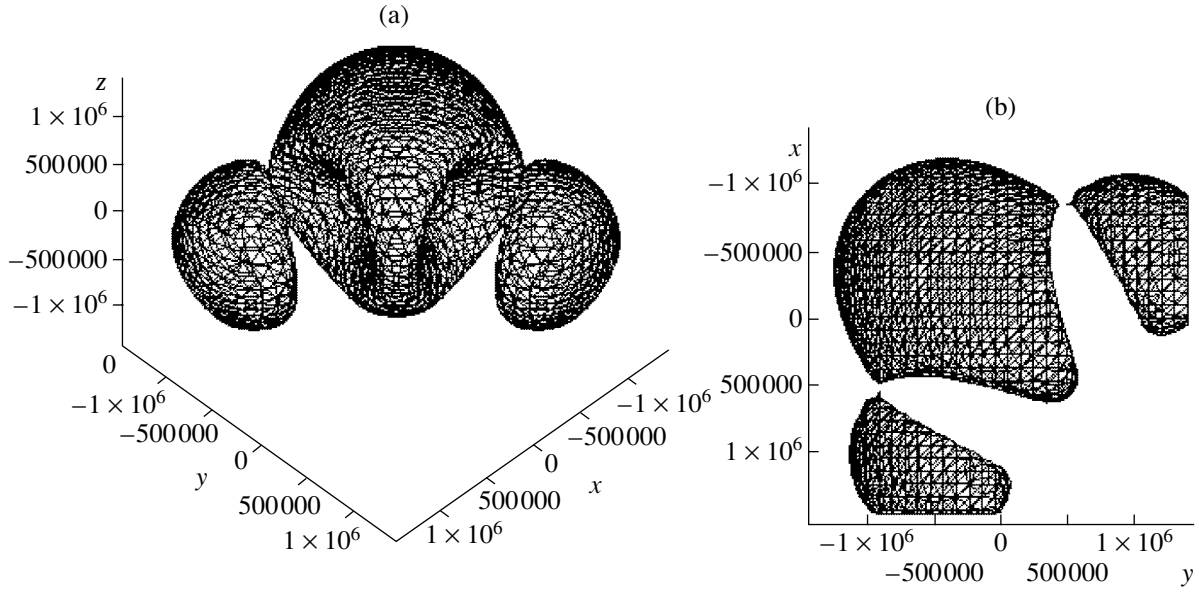

Fig. 3. Same as Fig. 1 for model B.

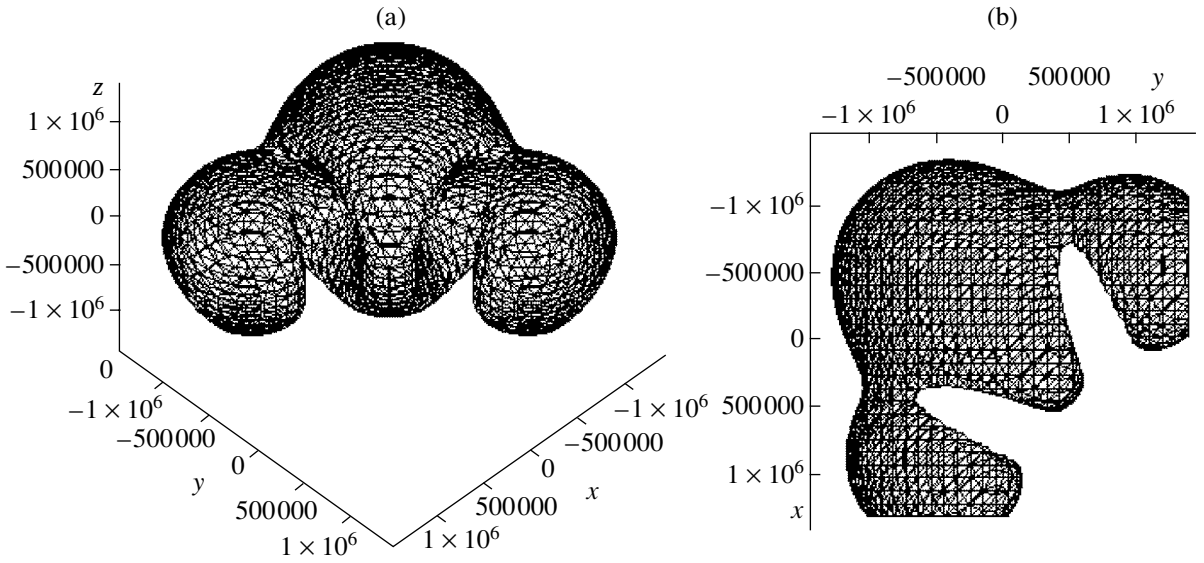

Fig. 4. Same as Fig. 2 for model B.

tem. Thus, the problem reduces to finding the surface specified by the expression

$$F(x,y,z) = x\frac{\partial U}{\partial x} + y\frac{\partial U}{\partial y} + z\frac{\partial U}{\partial z} = 0. \qquad (15)$$

We will take a selection of computer models for triple systems developed by us earlier [15] as characteristic examples. Let the system's components have zero velocity at the initial time (in this case, we will have planar motion of all three bodies) and equal masses, $M_i = M \quad (i = 1, 2, 3)$. We will consider three models, for which $M = (0.3; 3; 4) \times 10^{12}\ M_\odot$. The second of these models (which we will call model A) corresponds to a typical mass for a wide system, while the first (model B) and last (model C) have appreciably lower and somewhat higher masses, respectively. At the initial time, the components of the system form an isosceles right triangle with sides $S = (1.438; 2; 3)$ Mpc.

The numerical solution of this problem can be used to construct the zero-acceleration surfaces surrounding the systems described by these models for the states corresponding to the initial time, $T = 12.5$ Gyr ago, and the current epoch. Figures 1–6 present two

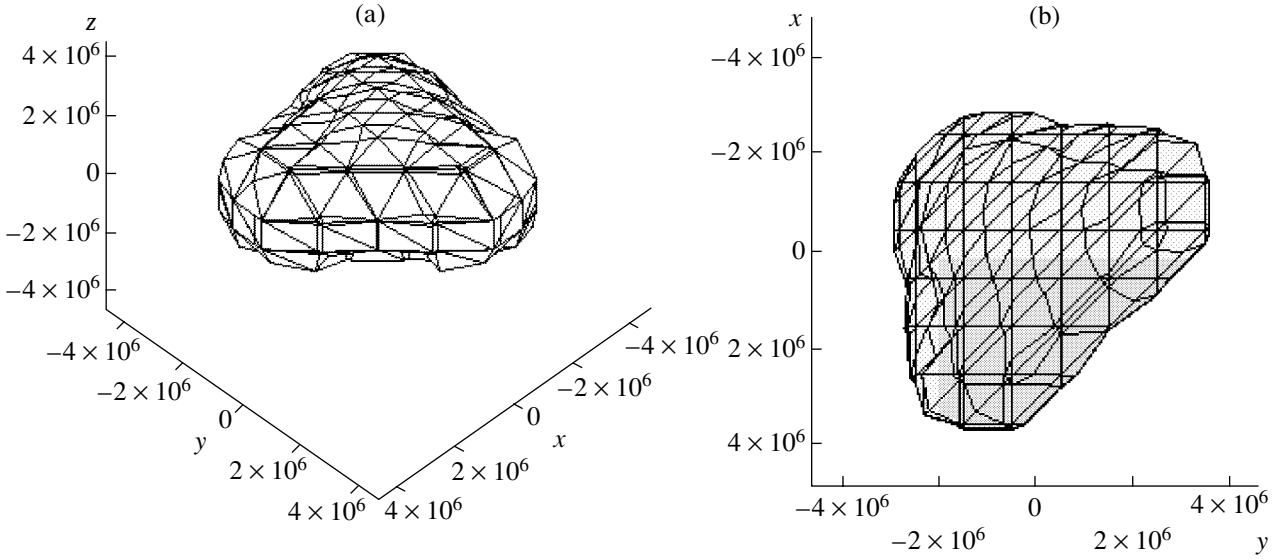

Fig. 5. Same as Fig. 1 for model C.

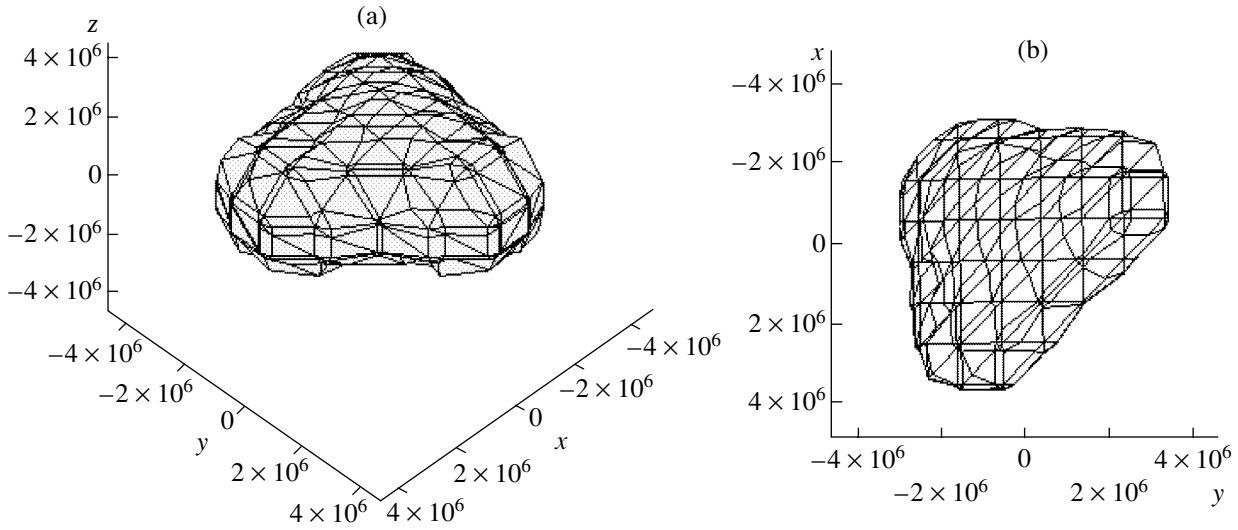

Fig. 6. Same as Fig. 2 for model C.

views of the zero-acceleration surfaces for each of the models at two times. For example, the surface for model A (a typical system) for the initial time is shown in Figs. 1a and 1b and for the current time in Figs. 2a and 2b. Comparing Figs. 1 and 2, we note that this surface has evolved only very weakly over the time the triple system has existed: the shape of the zero-acceleration surface remains nearly the same, and its dimensions have changed by no more than 10%. The surface has retained its rounded shape over this entire time interval. This result is clearly related to the fact that the characteristic time for the evolution of typical wide systems is comparable to, or even slightly greater than, their age (we encounter a similar situation for the Local Group).

Nearly the same is true of model C (Figs. 3, 4). In contrast, model B has a surface that is not singly connected in the initial state (Fig. 5)—there are three separate surfaces surrounding the three components of the system. Although the three masses are equal, the central mass gives rise to a larger surface, since it is located closer to the barycenter of the system. The evolution of the zero-acceleration surface for model B is clearly visible: it has become singly connected by the current epoch, although it remains far from rounded.

4. DISCUSSION: FROM GROUPS OF GALAXIES TO SUPERCLUSTERS

In the presence of spherical symmetry (as, for example, in the case of triple systems with a common dark-matter halo—see Section 3), the radial motion of a test body can, in general, be treated like one-dimensional motion in a field with the effective potential

$$\varphi(r) = -GM/r - \frac{4\pi G}{3}\rho_V r^2 + \frac{1}{2}K^2/r^2, \quad (16)$$

where K is the angular momentum of the body (per unit mass) relative to the center of the system. The potential approaches $+\infty$ when the radial distance approaches zero, and approaches $-\infty$ when the distance grows in unbounded fashion from the center. This latter property is due to the antigravity of the cosmic vacuum.

For reasonable values of the angular momentum and mass, the potential exhibits first a minimum, $\varphi_{\min}$, and then a maximum $\varphi_{\max}$ in the domain of negative values (Fig. 7). The motion is infinite when the total energy is $E = \frac{1}{2}\dot{r}^2 - GM/r - \frac{4\pi G}{3}\rho_V r^2 \geq \varphi_{\max}$. We see that the antigravity of the vacuum makes it possible for the motion to be infinite even if the energy is appreciably negative. When $E < \varphi_{\max}$, the motion is finite. The trajectories of finite motions are not closed.

In the special case of a radial trajectory ($K = 0$), the potential has only a maximum, located on the zero-acceleration sphere, $r = R_V$:

$$\varphi_{\max} = \varphi(R_V) = -\frac{1}{2}GM/R_V, \quad (17)$$

where, as above in Section 3, $R_V = [3M/(8\pi\rho_V)]^{1/3}$.

An can use this last formula to estimated the size of the finite surface—not only for triple systems with a common dark-matter halo, but also, for example, for large, regular clusters such as the Coma Cluster, in which the dark matter is distributed approximately spherically symmetrically. The estimated masses of such clusters are 10^{14}–$10^{16}\ M_\odot$, and the corresponding radii of their zero-acceleration surfaces are $R_V \simeq 5$–30 Mpc, which is not very different from the observed sizes of such systems. We expect similar values for the critical radii of (the very rare) quasi-spherical superclusters of galaxies.

Generally speaking, the geometry of the zero-acceleration surfaces for systems that do not possess even approximate spherical symmetry will be far from spherical. However, it turns out that the critical surface for the clearly nonspherical Local Group, which we considered in [4], is, in fact, nearly spherical; for a total mass for the Local Group of $2.5 \times 10^{12}\ M_\odot$, the critical radius given by our formula is $R_V \simeq 1.8$ Mpc,

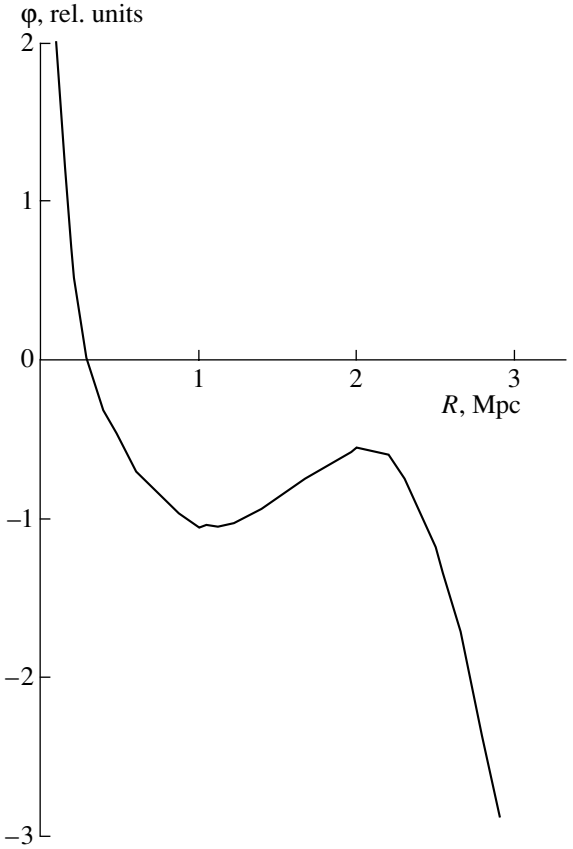

Fig. 7. Effective potential when the cosmic vacuum is present.

which is close to the corresponding size of the precise nonspherical critical surface (see Section 1).

The example of the Local Group enables us to suggest with some confidence that, for example, the characteristic sizes of the critical surfaces of irregular clusters of galaxies, such as the Virgo Cluster, can also be approximated using our simple formula. For a mass of 10^{13}–$10^{14}\ M_\odot$ this size will be $\simeq$(3–6) Mpc.

Substantial deviations from a spherical geometry are expected for superclusters that are very flattened (such as the Local Supercluster) or elongated (like the supercluster filaments). It is obvious that the zero-acceleration surfaces of flat systems should be likewise more or less planar (in their central regions). The characteristic distance to the zero-acceleration surface in directions perpendicular to the plane of a "pancakelike" supercluster, will be approximately

$$X_V \simeq 3\sigma/(8\pi\rho_V). \quad (18)$$

Here, σ is the characteristic surface density of the supercluster. If, say, $\sigma \simeq 10^{-3}$–10^{-2} g/cm^2, then $X_V \simeq 1$–10 Mpc, which is quite close to the typical half-thickness of a supercluster layer. In precisely the

same way, we will have for directions perpendicular to the axis of a filamentary system

$$R_V \simeq [3\Sigma/(8\pi\rho_V)]^{1/2}, \qquad (19)$$

where Σ is the characteristic linear density of the filament. For $\Sigma \simeq 10^{20}-10^{21}$ g/cm, we will have $R_V \simeq 1-3$ Mpc, which is very similar to the result for a supercluster "pancake."

Finally, note that the surfaces of zero gravity delineate the basic cells of which the overall structure of the Universe is composed. Each of these cells is almost constant in size, and all of them are in a state of accelerating cosmological expansion. Therefore, cosmological expansion is a phenomenon that is actually observed not only on the largest spacial scales, but, in fact, on all scales starting from several Mpc, i.e., from the distances between the centers of the smallest cells of zero gravity.

ACKNOWLEDGMENTS

The authors thank Yu.N. Efremov, I.D. Karachentsev, and D.I. Makarov for valuable discussions of the problem considered here.

REFERENCES

1. A. D. Chernin, Usp. Fiz. Nauk **171**, 1153 (2001).
2. A. D. Chernin, P. Teerikorpi, and Yu. V. Baryshev, Adv. Space Res. **31**, 459 (2003).
3. Yu. V. Baryshev, A. D. Chernin, and P. Teerikorpi, Astron. Astrophys. **378**, 729 (2001).
4. V. P. Dolgachev, L. M. Domozhilova, and A. D. Chernin, Astron. Zh. **80**, 792 (2003) [Astron. Rep. **47**, 728 (2003)].
5. A. G. Riess, A. V. Filippenko, P. Challis, *et al.*, Astron. J. **116**, 1009 (1998).
6. S. Perlmutter, G. Aldering, G. Goldhaber, *et al.*, Astrophys. J. **517**, 565 (1999).
7. P. J. E. Peebles and B. Ratra, Rev. Mod. Phys. **75**, 559 (2003).
8. A. D. Chernin, I. D. Karachentsev, M. J. Valtonen, *et al.*, Astron. Astrophys. **415**, 19 (2004); astro-ph/0310048.
9. A. V. Trofimov and A. D. Chernin, Astron. Zh. **72**, 308 (1995) [Astron. Rep. **39**, 272 (1995)].
10. Zh. P. Anosova, Astrofizika **26–27**, 653 (1988).
11. I. D. Karachentsev, V. E. Karachentseva, and V. S. Lebedev, Izv. Spets. Astrofiz. Obs. **27**, 67 (1989).
12. A. D. Chernin and M. J. Valtonen, New Astron. **42**, 41 (1998).
13. V. P. Dolgachev and A. D. Chernin, Astron. Zh. **74**, 328 (1997) [Astron. Rep. **41**, 284 (1997)].
14. V. P. Dolgachev, L. M. Domozhilova, and A. D. Chernin, Astron. Zh. **79**, 291 (2002) [Astron. Rep. **46**, 259 (2002)].
15. A. D. Chernin, V. P. Dolgachev, and L. M. Domozhilova, Mon. Not. R. Astron. Soc. **319**, 851 (2000).

Translated by D. Gabuzda

Astronomy Reports, Vol. 48, No. 10, 2004, pp. 795–799. Translated from Astronomicheskiĭ Zhurnal, Vol. 81, No. 10, 2004, pp. 876–880.

Estimate of the Evolution of the Galactic Gas Component for the z Interval from 0 to 3.6

A. F. Dravskikh

St. Petersburg Branch of the Special Astrophysical Observatory, Russian Academy of Sciences, St. Petersburg, Russia

Received June 15, 2003; in final form, March 15, 2004

Abstract—The absorbers giving rise to features in the absorption spectra of quasars can be used to study the evolution of the dimensions of the galactic gas component and of gas clouds over substantial intervals of z. The evolution of the linear dimensions L of these objects is estimated for the z range from $\sim$0 to 3.6. A total of 265 quasars with redshifts z from 0.288 to 3.803 and 809 absorbers with z from $\sim$0 to 3.5575 were used for the analysis, which yields the relation $L = L_0(1+z)^{1.73\pm0.07}$. © *2004 MAIK "Nauka/Interperiodica".*

1. INTRODUCTION

The absorption lines of heavy elements observed in quasar spectra carry information about the distances of galaxies and gas clouds (primarily, galaxies) in a very large interval of redshift z from 0 to $\sim$6. These distances can be used to estimate the cosmological parameters of the Universe, but evolutionary effects associated with the absorbers must be taken into account, and these effects have been little studied thus far. Earlier analysis indicates that, even if such evolutionary effects are known, the cosmological parameters cannot be determined accurately in this way. On the other hand, the evolution of the dimensions of the absorbers for a specified model of the Universe can be determined much more accurately. Fortunately, as was shown in the review [1], an appropriate model for the Universe and its cosmological parameters have now been established with reasonable certainty. Therefore, we shall use these cosmological parameters to study the evolution of the dimensions of the absorbers.

Such estimates could potentially be based on spectral measurements conducted in various studies. We used the combined quasar catalog [2], which contains information about the redshifts z of the absorbers giving rise to features in the quasar spectra (z_{abs}). In the future, when spectral measurements for a large number of objects will be available from the Sloan Digital Sky Survey (SDSS), it should be possible to estimate cosmological parameters in the same way using these data.

The dimensions of the absorbers giving rise to ultraviolet hydrogen lines (the Lyα forest) increase with time (i.e., their sizes increase with decreasing z) [3–5]. The evolution of the dimensions of galaxies can be studied using observations of the galaxies' emitting regions. As was shown in [6–8], galaxies evolve in accordance with the expectations of cold, dark matter models, so that their dimensions likewise increase with decreasing z.

Our estimates of the evolution of the sizes of galaxies based on the absorption lines of heavy elements in quasar spectra differ from the results of the above studies; however, this is quite natural, since the authors of [6–8] measured the distribution of the stellar population of the galaxies, while we are measuring the distribution of the ionized gas component.

2. METHOD FOR ESTIMATING THE EVOLUTION OF THE ABSORBER DIMENSIONS FROM THE z DISTRIBUTION OF THE ABSORBERS

It is well known [9] that the absorbers giving rise to absorption lines of heavy elements in quasar spectra can be associated with both galaxies and gas clouds (primarily, galaxies). The positions of the spectral lines are determined by the redshifts z of the absorbers. These data can be used to obtain the distribution of the absorber density as a function of z.

The idea of deriving cosmological parameters from the z distribution of the absorbers (assuming a specified evolution for the absorber size) or, vice versa, studying the evolution of the sizes of the absorbers themselves (assuming specified cosmological parameters) is based on the assumption that the Universe is uniform and isotropic. In this case, the mean density of matter in a comoving dimensionless coordinate system depends only on time, and does not depend on the coordinates in any model of the Universe.

1063-7729/04/4810-0795$26.00

To carry out such calculations, we must know the emission redshifts (z_{em}) of the quasars whose absorption spectra we are analyzing, as well as the absorption redshifts (z_{abs}) of the absorbers giving rise to features in the quasar spectra. Of course, the information on the quasar absorption spectra used must be sufficiently complete (although completeness of the quasar catalog is not required).

In our subsequent calculations, the absorbers will be made "depersonalized"; i.e., we will not take into account the fact that an absorber has given rise to lines in the spectrum of some particular quasar. The computational region is a sphere with its center at $z = 0$ and with its radius z_{abs} equal to the redshift of the most distant absorber. We ordered the list of N absorbers according to increasing z_{abs}. The entire list was then subdivided into roughly $\sqrt{N}$ bins, with approximately $\sqrt{N}$ absorbers in each bin. The bins form spherical layers of thickness $(z_{abs\,\max(i)} - (z_{abs\,\max(i-1)})$, where $z_{abs\,\max(i)}$ is the maximum value of z_{abs} in bin i.

If the observing conditions for the absorbers were all the same, the density of the absorbers in a bin could be calculated simply by dividing the number of absorbers in the bin by its volume. In fact, the observing conditions depend on z_{abs}. This can be taken into account as follows.

An absorber with redshift z_{abs} can potentially be in the line of sight of any quasar possessing an emission redshift $z_{em} > z_{abs}$. Therefore, each detected absorber can be characterized by its detection rate, equal to $1/m$, where m is the number of quasars with absorption features for which $z_{em} > z_{abs}$. This detection rate is distorted: even if the absorbers have the same size, those located closer to the observer will be detected more often, since their apparent angular size will be greater than for distant absorbers. To exclude this dependence in the case of a statistically uniform distribution of quasars over the sky, we must divide $1/m$ by the solid angle Θ^2 subtended by the absorber. In addition, we must take into consideration the possible evolutionary dependence of the absorber size on z. Then, $1/m\Theta^2$ will represent an estimate of the true detection rate of the absorber per quasar, and this quantity will be proportional to the number of absorbers at redshift $z_{abs} \pm \Delta z$. The number of absorbers in the bin from z_i to $z_{(i+1)}$ will be proportional to the sum of the quantities $1/m_k\Theta_k^2$ in the bin:

$$\sum_{k=1}^{n} \frac{1}{m_k\Theta_k^2},$$

where k runs over all values from unity to the total number of absorbers in the bin, n.

According to [10], the comoving distance along the line of sight from the observer to the object will be

$$\chi(z) = cH_0^{-1} \int_0^z [\Omega_m(1+z')^3 + \Omega_k(1+z')^2 + \Omega_q(1+z')^{3(1+\omega_q)}]^{-1/2} dz', \quad (1)$$

where z is the object's redshift, c is the speed of light, and H_0 is the Hubble constant at the present time. The quantities $\Omega_{m,k,q}$ represent fractions of the critical energy density: Ω_m corresponds to matter without pressure, or dust, Ω_k to the curvature of space, and Ω_q to the quintessence (a liquid medium with negative pressure; the pressure p of such a medium is related to its density ρ by the formula $p = \omega_q\rho$, where $\omega_q < 0$). When the cosmological constant Λ is used, $\omega_q = -1$. Since we shall use Λ, we will replace Ω_q with Ω_Λ. The sum of the three densities is $\Omega_m + \Omega_k + \Omega_\Lambda = 1$.

The angular diameter Θ of an object in a uniform, isotropic model with cosmological constant Λ is defined to be $\Theta = L/r(\chi)$, where L is the linear size of the object and $r(\chi)$ is the angular-diameter distance of the object, which is equal to [11]

$$\begin{gathered} r(\chi) = K^{-1/2}\sin(K^{1/2}\chi) \\ \text{for a closed model,} \\ r(\chi) = \chi \quad \text{for a flat model,} \\ r(\chi) = (-K)^{-1/2}\,\mathrm{sh}((-K)^{1/2}\chi) \\ \text{for an open model,} \end{gathered} \quad (2)$$

where $K = (\Omega_m - 1)c^{-2}H_0^2$.

The evolution of the linear size of the absorber L is given by

$$L = L_0(1+z)^\beta. \quad (3)$$

It has now been established [1] that the Universe is expanding with acceleration and with the cosmological parameters $\Omega_m \approx 0.3$, $\Omega_\Lambda \approx 0.7$, and $\Omega_k \approx 0$. We will use precisely this model of the Universe, corresponding to flat space ($\Omega_m + \Omega_\Lambda = 1$), below.

Let us rewrite all expressions in dimensionless form and take into account the fact that $\Omega_k = 0$. A dimensionless comoving distance S will then take the form

$$S = \int_0^z [\Omega_m(1+z')^3 + \Omega_\Lambda]^{-1/2} dz'. \quad (4)$$

The angular size of the source is

$$\Theta = \frac{(1+z)^\beta}{R}, \quad (5)$$

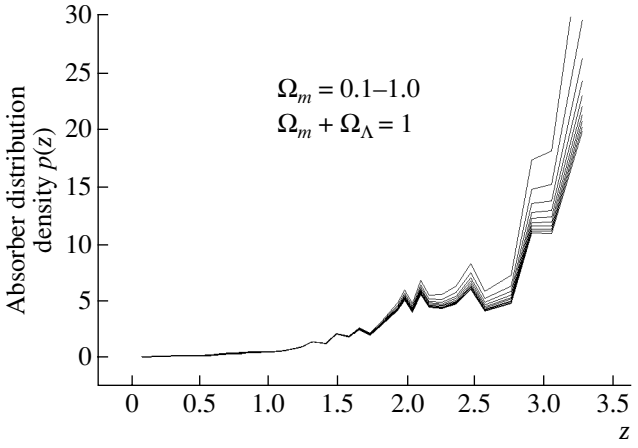

Fig. 1. Distribution of the absorber density over z neglecting evolution of the absorbers.

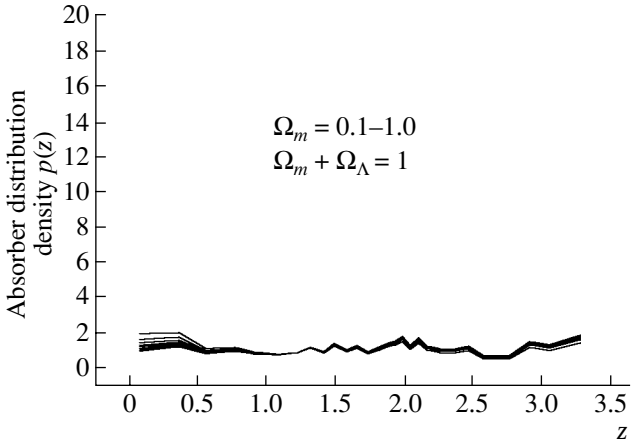

Fig. 2. Same as Fig. 1 for the case when evolution of the absorbers is taken into account in the form $L = L_0(1 + z)^{1.7}$.

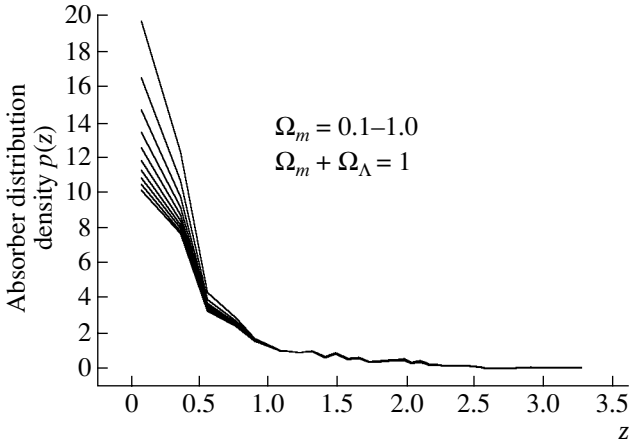

Fig. 3. Same as Fig. 1 for the case when evolution of the absorbers is taken into account in the form $L = L_0(1 + z)^{3.5}$.

where we have disregarded a constant coefficient that is not important in relative measurements, and the dimensionless angular-diameter distance R in the flat model is equal to the comoving distance, $R = S$.

The volume of a bin in the comoving coordinate system will be

$$v_i = (s^3_{\max(i)} - s^3_{\max(i-1)}), \qquad (6)$$

where we have disregarded the constant coefficient $4/3\pi$, and $s_{\max(i)}$ and $s_{\max(i-1)}$ are the dimensionless comoving distances to the more distant boundaries of bins i and $i - 1$.

The density of absorbers p_i in bin i will then be

$$p_i = \left(\sum_{k=1}^{n} \frac{1}{m_k \Theta_k^2}\right) / v_i. \qquad (7)$$

We must next calculate the absorber densities over all bins for various values of the exponent β determining the evolution of the absorber size. The z distributions of the density of absorbers for various β can be approximated by straight lines, and we must find the tangents of the angles α of these lines to the z axis: the value of β for which $\tan\alpha = 0$ is the required solution.

Of course, the same method can be used to determine the cosmological parameters if β is fixed and the calculations are carried out for various cosmological parameters. However, as has already been noted, the resulting accuracy of the cosmological parameters in this case is not very high.

3. ESTIMATED EVOLUTION OF THE LINEAR SIZE OF THE ABSORBERS

We estimated the exponent β [see (3) and (5)] determining the evolution of the absorber size using the combined quasar catalog [2], which is the only catalog in which values of z_{abs} are presented. The catalog includes 7315 quasars, ∼10% of which possess absorption spectra. We chose only those quasars for which sufficiently accurate values of z_{abs} (three or more digits after the decimal point) are available.

This criterion identified 265 quasars suitable for subsequent analysis, which involved absorption features due to 809 absorbers. The emission redshifts of the quasars are in the range $z_{em} = 0.288$–3.803, whereas the values of z_{abs} are distributed from ∼0 to 3.5575. These data were analyzed using the method described.

This yielded 28 redshift bins (spherical layers in z), with each bin except for the last containing 29 absorbers; the last bin contained 26 absorbers. The

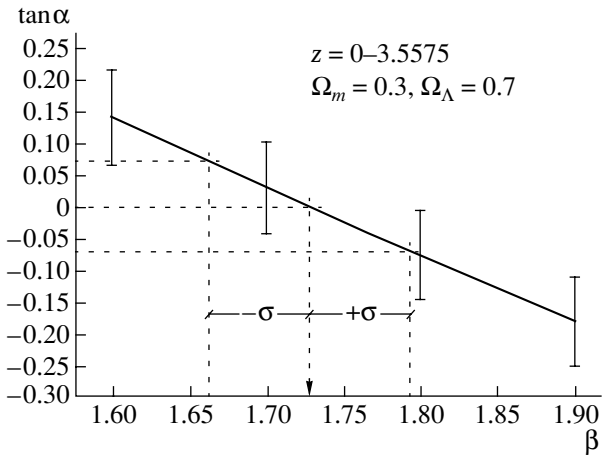

Fig. 4. Tangent of the angle of the absorber density-distribution line to the z axis as a function of β for the case when the absorber size evolves as $L = L_0(1 + z)^{1.73\pm0.07}$.

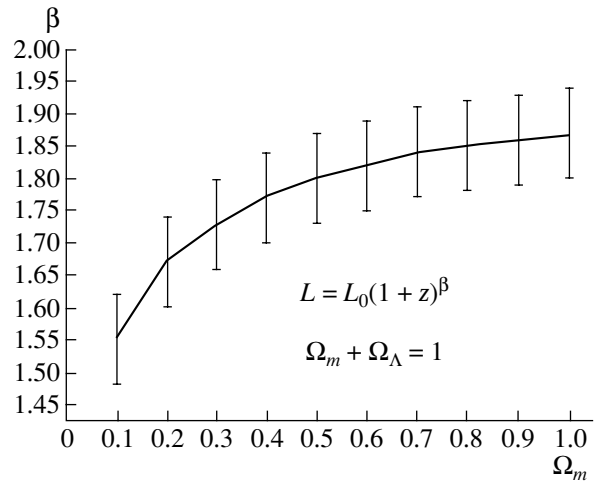

Fig. 5. Dependence of β on Ω_m, illustrating that the evolution of the absorbers is not appreciably affected by the model of the Universe.

density of the absorbers over the bins was calculated for various β.

The z distributions of the absorber density are presented in Figs. 1–3 for ten models of the Universe ($\Omega_m = 0.1$–1.0, $\Omega_m + \Omega_\Lambda = 1$) for no absorber evolution (Fig. 1), evolution according to the law $L = L_0(1 + z)^{1.7}$ (Fig. 2), and evolution according to the law $L = L_0(1 + z)^{3.5}$ (Fig. 3).

It is obvious that none of the models provide a satisfactory description in the case of nonevolving (Fig. 1) or rapidly evolving (Fig. 3) absorbers. On the other hand, evolution of the absorbers in accordance with the law $L = L_0(1 + z)^{1.7}$ (Fig. 2) is close to the required dependence. The specific value of β for the model with $\Omega_m = 0.3$ and $\Omega_\Lambda = 0.7$ was obtained by varying the exponent β about $\beta = 1.7$.

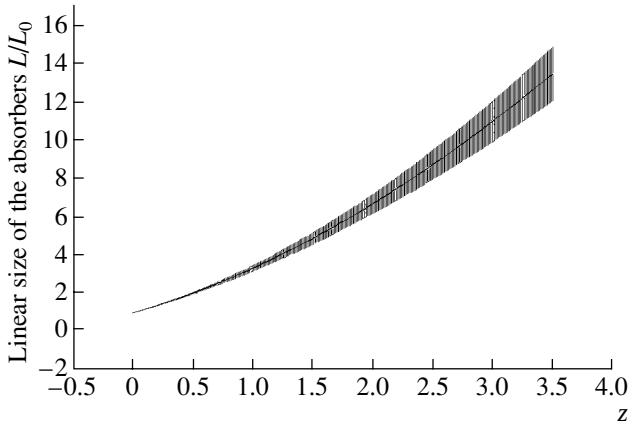

Fig. 6. Evolution of the linear size of the absorbers according to $L = L_0(1 + z)^{1.73\pm0.07}$.

The tangent of the angle of the absorber density-distribution line to the z axis as a function of β is presented in Fig. 4.

We obtain $\tan\alpha = 0$ when $\beta = 1.73$; i.e., the density of absorbers in a comoving coordinate system does not depend on the coordinates. Consequently, this is the required value of β. The figure also shows the random errors. The formal measurement errors are fairly small: $\beta = 1.73 \pm 0.07$. For comparison, the errors in the cosmological parameter Ω_m in the case of evolution of the absorbers with $\beta = 1.73$ are $\Omega_m = 0.3^{+0.2}_{-0.1}$ ($\Omega_m + \Omega_\Lambda = 1$).

We also carried out the analysis for all the quasars in the catalog [2] with absorption features in their spectra, without placing restrictions on the accuracy of the z_{abs} values. In this case, the total number of quasars was 392; and the number of absorbers was 1286. This yielded $\beta = 1.78 \pm 0.07$, almost the same as before. This agreement can be explained by the fact that selecting quasars with accurate z_{abs} values leads to a relative decrease in the errors, but the random errors increase due to the smaller amount of data used in the analysis.

We determined the evolution of the absorber sizes for various models of the Universe. The value of Ω_m was varied within 0.1 to 1.0, with $\Omega_m + \Omega_\Lambda = 1$. A plot of the dependence of β on Ω_m is presented in Fig. 5.

Figure 6 shows the linear sizes of the absorbers as a function of z in the cosmological model with $\Omega_m = 0.3$ and $\Omega_\Lambda = 0.7$ together with the corresponding errors.

4. CONCLUSION

We emphasize again that the z dependence of the absorber sizes we have obtained describes the evolution of the linear sizes of the ionized gas component in galaxies and clouds. This dependence indicates a very rapid loss of gas in the course of the evolution. This is quite natural, since gas is consumed by star formation, and also disappears when black holes and dwarf stars are formed.

On the other hand, the obtained absorber evolution, with their sizes varying as $(1+z)^{1.73}$, involves a number of other evolutionary changes as well (e.g., in the degree of ionization, the matter density, etc.). Therefore, this is actually the evolution of some effective size of the absorbers.

The increase in the sizes of the emitting regions of galaxies with decreasing z is due to the propagation of star formation from the centers of the galaxies to their peripheries [6]. The increase in the sizes of the absorbers with decreasing z observed in the Lyα lines probably indicates an absence of star formation in these gas clouds.

It would be very interesting to study the evolution of the absorbers observed in quasar Lyα lines in more detail.

ACKNOWLEDGMENTS

We are grateful to Yu.N. Pariĭskiĭ and V.K. Dubrovich for fruitful criticism, and to Z.V. Dravskikh and A.V. Temirova for assistance in the preparation of the manuscript.

REFERENCES

1. V. Sahni and A. Starobinsky, astro-ph/9904398 (1999).
2. A. Hewitt and G. Burbidge, Astrophys. J., Suppl. Ser. **87**, 451 (1993).
3. N. Dinshaw, C. B. Foltz, C. D. Impey, *et al.*, Astrophys. J. **494**, 567 (1998).
4. T.-S. Kim, R. F. Carswell, S. Cristiani, *et al.*, Mon. Not. R. Astron. Soc. **335**, 555 (2002).
5. M. Bernardi, R. Sheth, M. SubbaRao, *et al.*, Astron. J. **125**, 32 (2003).
6. N. Roche, K. Ratnatunga, R. E. Griffiths, *et al.*, Mon. Not. R. Astron. Soc. **293**, 157 (1998).
7. F. Poli, E. Giallongo, N. Menci, *et al.*, Astrophys. J. **527**, 662 (1999).
8. E. Giallongo, N. Menci, F. Poli, *et al.*, Astrophys. J. **530**, L73 (2000).
9. W. L. W. Sargent, A. Boksenberg, and C. C. Steidal, Astrophys. J., Suppl. Ser. **68**, 539 (1988).
10. P. J. E. Peebles, *Principles of Physical Cosmology* (Princeton Univ. Press, Princeton, 1993).
11. Hui Lam, astro-ph/9902275 (1999).

Translated by Yu. Dumin

Astronomy Reports, Vol. 48, No. 10, 2004, pp. 800–812. Translated from Astronomicheskiĭ Zhurnal, Vol. 81, No. 10, 2004, pp. 881–894.

Models of Astrophysical Decretion–Accretion Diffusional Disks

A. V. Tutukov and Ya. N. Pavlyuchenkov

Institute of Astronomy, Russian Academy of Sciences, ul. Pyatnitskaya 48, Moscow, 109017 Russia

Received January 12, 2004; in final form, March 15, 2004

Abstract—The formation of gaseous diffusional accretion–decretion disks is an important stage in the evolution of numerous astronomical objects. Matter is accreted onto the object in the accretion part of these disks, while the angular momentum of the accreted matter is transported from the central region to the periphery in the decretion part. Here, we consider general questions connected with the formation and evolution of diffusive accretion–decretion disks in various astrophysical objects. Such disks can be described using nonstationary diffusion models. The phenomenological parameters of these models are the coefficients in the relations for the characteristic turbulent velocity and mean free path of diffusion elements in the disk. We have developed a numerical technique to compute the disk evolution for a number of models (a massive disk, a disk with continuous accretion, a purely decretion disk). Analytical expressions estimating the basic parameters of accretion–decretion disks are presented. We discuss the relationship between the models considered and the classical α model of an accretion disk. © *2004 MAIK "Nauka/Interperiodica".*

1. INTRODUCTION

The first astronomical disk, the Milky Way, was detected in ancient times with the naked eye. Galileo was the first to observe a second example of a disk in space in 1609—the ring of Saturn. The third such object was the protoplanetary gas–dust circumsolar disk introduced by Kant and Laplace to explain the origin of the solar system [1]. Whereas Kant did not speculate about the origin of this disk, Laplace [2] suggested that it originated from the rapidly rotating, comparatively compact young Sun. He assumed that the solar material moved away from the Sun in the equatorial plane due to viscosity, gradually forming an extended protoplanetary gas–dust disk. Thus, in essence, the first theoretical model of an astronomical disk involved a purely decretion disk. One possible origin of the viscosity in protoplanetary disks, associated with their magnetic fields, was pointed out by Hoyle [3]. Another efficient source of viscosity in a gaseous disk is turbulence.

Accretion disks appeared in modern astrophysics in the 1930s to 1950s, when they were introduced by observers studying cataclysmical and Algol-type close binaries [4, 5, 6]. In such systems, one of the stars fills its Roche lobe, providing a continuous gas flow toward the secondary. The high orbital angular momentum of this gas prevents it from being accreted directly, and it replenishes a gaseous ring around the accretor. The viscosity of the gaseous ring results in the development of a accretion–decretion disk.

Active studies of accretion disks did not begin until it was realized that a potentially large amount of energy could be released in the course of accretion onto very compact neutron stars and stellar-mass black holes [7, 8] and supermassive black holes in the cores of galaxies [9]. The identification of several bright X-ray sources with close binaries gave rise to studies of the structure of accretion disks with the aim of explaining the X-ray spectra of X-ray binaries detected in the late 1960s. The theoretical foundations for this problem were laid by Shakura [10] and others [11, 12]. The well known α model for accretion disks [10] assumed a circular Keplerian gaseous disk in which radial motions (the accretion of gas) were governed by the turbulent viscosity. The velocity U of the turbulent elements in the disk were determined in terms of the local sound speed in the gas, V_s, and the quantity $U = \alpha V_s$, where α is a dimensionless parameter; the mean free path was assumed to be equal to the disk thickness. In recent years, progress in computing technology and numerical gas-dynamical methods have made it possible to develop two- and three-dimensional models for the accretion disks surrounding the accreting components of close binaries [13, 14].

Studies of the late stages of the evolution of close binaries suggest a possible mechanism for the formation of massive accretion–decretion disks. Such disks may arise during the evolution of semidetached close binaries, due to the dynamical collapse of the component that fills its Roche lobe [15]. Two basic possibilities for the formation of such disks have been suggested. These are associated with the filling of the Roche lobe of either a degenerate companion

1063-7729/04/4810-0800$26.00

or a fully convective low-mass star (with a mass lower than 0.3 $M_\odot$). Due to their rapid mass loss, such donors expand within the dynamical timescale, while their Roche lobes contract. This results in the development of dynamical instability, leading to the disruption of the donor. Due to the conservation of its orbital angular momentum, the donor is transformed into a massive compact disk around the accretor for a few minutes (a degenerate dwarf) or hours (a fully convective main-sequence star).

The ultimate origin of the angular momentum of stars, the multiplicity of most stars [16], and the existence of circumstellar disks is the rotation of the molecular clouds that are the precursors of stars. The observed maximum angular rotational velocities for the cores of molecular clouds are $\sim 3 \times 10^{-15}$–10^{-13} s^{-1} [17–19]. Such gaseous clouds with solar masses should give birth to multiple systems with semimajor axes of 10^4–10^8 $R_\odot$. However, observations indicate that binaries with semimajor axes exceeding 10^6 $R_\odot$ are very rare [16]. This probably means that such systems disintegrate during the early stages of their evolution into relatively dense young star clusters.

Here, we consider the general problem of the formation and evolution of various types of astrophysical disks in the framework of a unified diffusion approach. We numerically study the evolution of diffusive disks using a one-dimensional nonstationary model. The character of the solutions obtained is determined by the diffusion coefficient D. Since the atomic viscosity cannot provide the observed accretion rates of astrophysical objects, we suggest that the viscosity (diffusion) in these disks is due to the turbulent motion of the gas [20–22]. We normalized the mean free path of turbulent elements to the distance to the accreting object r, and the velocity to the local Keplerian velocity V. Note that some other factors, such as the disk magnetic field or spiral density waves in the disk, may also be sources of viscosity. Spiral density waves occur in spiral galaxies and, probably, in the accretion disks of dwarf novas with superoutbursts [23]. In this case, when using the term "the mean free path of the turbulent elements," we have in mind the characteristic local scale for the transport of angular momentum.

Section 2 of the paper describes basic examples of astrophysical accretion–decretion disks. Section 3 analytically estimates the characteristics and type of evolution of massive accretion–decretion disks. Section 4 considers simulations of the evolution of some types of astrophysical disks obtained with the one-dimensional diffusion model. The main results of our analysis of the evolution of astrophysical accretion–decretion disks are presented in the Conclusion.

2. ASTROPHYSICAL DIFFUSIONAL DECRETION–ACCRETION DISKS

Here, we consider some examples of astrophysical disks of various types, to which the numerical models and analytical formulas that we have obtained in the current study can be applied. All these examples originate from observational and theoretical analyses of the structure and evolution of various astrophysical objects: galaxies, binary and single stars, and planetary systems. Let us consider the basic characteristics of their formation and evolution, together with the observed manifestations of these characteristics.

Massive, compact, gaseous circumstellar disks. As was noted in the Introduction, a compact gaseous disk with a mass comparable to that of the accreting star can form in the course of the evolution of a compact close binary. During the subsequent evolution of this disk, the remaining star accretes most of the disk material, leading to the formation of an extended diffusive accretion–decretion (DAD) disk around the star, which accumulates the angular momentum of the system. Evidence for this scenario is provided by the formation of single millisecond radio pulsars and planets around radio pulsars [16, 24]. Planets around degenerate dwarfs and some main-sequence stars may originate in the same way; in this case, the precursors are contact binaries. When the companion of a W UMa star disintegrates, the relative mass of the disk will be about 0.1. In the coalescence of degenerate components of a close binary (when the components approach due to the radiation of gravitational waves), the tidal disruption of the lower-mass companion results in the formation of compact gaseous disks with a larger relative mass (up to unity).

A similar situation is encountered in connection with the outbursts of dwarf novas and the sources of activity of symbiotic binaries. In a nonstationary regime, the mass transfer between the components is divided into two phases. During the first phase, the matter of the donor accumulates in a gaseous disk (ring) around the accretor. The onset of convection in the disk (the second phase) results in a substantial increase in the gas viscosity, the rapid accretion of most of its material onto the dwarf, and the expansion of the decretion part of the disk to a size limited by its interaction with the secondary.

Circumplanetary asteroid–dust disks. Dust is an important component of cool cosmic matter. The dusty nature of the ring around Saturn was demonstrated in 1659 by Huygens. It is now clear that similar disks exist around all the giant planets in the solar system. Their formation, structure, and evolution have been extensively studied [25–28]. The leading roles in the formation and evolution of circumplanetary rings are played by viscosity associated with

the interaction between the asteroid–dust and gas components, self-gravitation in the asteroid component, collisions between asteroids, and possibly electromagnetic interactions between asteroids [29]. In a number of studies, the evolution of circumplanetary disks and the role of resonances with the motions of the planet's moons are modeled in the framework of the constrained gravitational N-body problem [30, 31]. The mechanism for the formation of asteroid rings remains unclear, and their lifetimes may be substantially shorter than the age of the Sun [32]. Matter is probably continuously supplied to the circumplanetary rings by collisions between asteroids and moons [33]. Indeed, planets with rings have numerous moons.

Accretion disks in cataclysmic binaries. A cataclysmic binary consists of a main-sequence star with a mass lower than that of the Sun that fills its Roche lobe and a compact degenerate accretor. Observations indicate that the accretion disks are either steady-state or periodically accumulate matter at their outer edge (in a gaseous ring), which is then accreted during a short phase during the development of a quasi-steady-state DAD disk. In a cataclysmic system, the donor may also be a nondegenerate helium star with a mass of 0.4–1 $M_\odot$ or a low-mass ($\sim$0.1 $M_\odot$) degenerate dwarf [34]. The presence of a degenerate donor makes the system particularly compact; in this case, the orbital periods reach 10–30 min and the semimajor axes 0.2–0.3 $R_\odot$. In systems such as 4U 0614+09 and 2S 0918–543, the radius of the accretion disk does not exceed 0.1 $R_\odot$ [35].

The accretion of matter by the compact components of cataclysmic systems is possible only if the angular momentum is tranported to the outer edge of the disk. From there, the angular momentum is partially transferred to the orbital motion, probably primarily in the active phase of accretion during outbursts, via spiral shocks in the disk. Some of the angular momentum may be lost from the system together with matter flowing from the outer edge of the disk [36]. Some fraction of the momentum may also be carried away with the magnetic stellar wind generated by the disk.

Accretion disks in dwarf X-ray binaries. A dwarf X-ray binary consists of a main-sequence donor with a mass not exceeding that of the Sun and a relativistic accretor—a black hole or neutron star. The characteristic orbital periods of such systems do not exceed a day. The evolutionary status and main driving forces contributing to the evolution of these systems are similar to those of cataclysmic binaries, but an important difference is the presence of a bright (up to 10^4 $L_\odot$) X-ray source; several percent of its energy is intercepted by the donor, exciting an intense induced stellar wind [37]. The accretor intercepts some fraction of the wind material in the Bondi–Hoyle regime, maintaining its accretional X-ray luminosity. In this case, filling of the Roche lobe by the donor is no longer necessary for mass exchange between the components. However, simulations have shown that the mass exchange will be efficient only if the donor surface remains close to its Roche lobe. The radius of the matter-capture cone is $r \sim (GM/V_w^2)^{0.5}$, where G is the gravitational constant, M is the mass of the accretor, and $V_w = (Gm/R)^{0.5}$ is the velocity of the stellar wind, which is generally close to the parabolic velocity at the donor surface (m and R are the mass and radius of the donor). The initial radius R_d of the disk formed due to the capture of the stellar wind from the donor can be estimated from the condition that angular momentum be conserved, assuming that the axial and orbital rotation of the donor are synchronous:

$$\frac{R_d}{A} = \frac{R^4}{A^4}\frac{(M+m)m^3}{M^4}, \qquad (1)$$

where A is the semimajor axis of the system. Adopting, for example, $R = A/2$ and $M = m$, we obtain $r = 0.1A$, which implies that the initial size of the disk consisting of matter captured from the wind is substantially smaller than the Roche lobe of the accretor, $\sim$0.4A. Such a disk will undergo quasi-steady-state accretion, with the gaseous disk gradually expanding and accumulating the angular momentum of the accreted matter. It is likely that the fate of the periphery of the decretion part of the disk is similar to that of the outer edge of the disk in a cataclysmic system.

Gaseous disks in symbiotic binaries. A classical symbiotic binary consists of a (super)giant with an intense stellar wind that does not fill its Roche lobe and a degenerate dwarf in an orbit with a period of several years [38–40]. As in the case of low-mass X-ray binaries, the degenerate dwarf captures some of the wind from the (super)giant, forming an accretion disk. The initial radius of this disk can be estimated using the above formalism (1). Simulations of the capture of the donor wind by the accretor in a symbiotic system confirm these estimates [41]. The accretion results in various types of activity of the accreting degenerate dwarf, and the angular momentum of the accreted matter is accumulated in the decretion part of the disk. The instability of this part of the disk may (and probably does) contribute to the observed variability of these stars.

In the Bondi–Hoyle regime for the accretion of the stellar wind, the initial radius of the accretion disk depends strongly on the wind velocity. It is easy to show that the accretion rate varies with the wind velocity as V_w^{-4}, while the the initial radius of the disk varies as V_w^{-8}. The velocity of the wind from the donor varies due to a number of natural reasons, leading to

dramatic variations in the brightness and spectrum of the disk. If the velocity of the stellar wind exceeds some limit [which can be determined from (1)], the accretion disk should totally disappear. In this case, the matter captured from the donor's stellar wind will be accreted directly onto the surface of the compact object, with the formation of intense shocks.

Gas–dust disks around T Tauri stars. Observations indicate that young ($\sim 3 \times 10^6$ years) solar-mass T Tauri stars possess extended (several hundreds of AU in size) gas–dust disks [42, 43]. For example, ASR 41—a T Tauri star with an age of $\sim 10^6$ years—accretes matter at a rate of $\sim 3 \times 10^{-6}\ M_\odot$/yr. Its gas–dust disk has a radius of $\sim$200 AU and a mass of $\sim 0.06\ M_\odot$ [42]. If this is an accretion disk, then, given the large specific angular momentum, it becomes unclear what prevented the formation of a binary, or even multiple, system. Therefore, it is logical to suggest that the initial radius of the disk was small, for example, ~ 10–$30 R_\odot$. Then, an extended phase of accretion onto the central star could accumulate the angular momentum in a relatively low-mass, extended decretion disk. The termination of the accretion onto the young star results in the decay of turbulent motions in the gas–dust disk, in turn leading to the separation of the dust component of the disk and the aggregation of planets [1]. Thus, the extended gas–dust disks observed around young stars are, in essence, protoplanetary disks [16].

Decretion disks around Be stars. Classical Be stars are main-sequence stars with masses of 3–$18\ M_\odot$ possessing gaseous circumstellar disks [44, 38]. One possible reason for the presence of the gaseous circumstellar envelope (disk) is the diffusion of angular momentum from the contracting helium-enriched core of the star to the envelope [45–48], which results in steady-state mass loss from the equator of the star and the formation of a purely decretion gaseous disk surrounding it. The mass loss may be facilitated if the star is in a close binary, since the effective gravitational acceleration decreases due to the tidal forces [49]. As a result of the diffusion of angular momentum, matter flows from the contracting core over a time comparable to the star's lifetime on the main sequence, provided the initial rotational velocity of the zero-age main-sequence star exceeded half the limiting velocity [45, 46]. Modeling of the hydrodynamics of decretion disks [47, 48] with a constant temperature [50, 51] has indicated that these disks expand. Three-dimensional modeling has shown that the presence of a close companion (for example, a neutron star) near a Be star restricts the expansion of the disk to a size comparable to that of the Roche lobe [48]. In this case, the development of spiral shocks in the disks generally favors the transformation of the angular momentum of the outer part of the decretion disk into orbital angular momentum. In the case of single Be stars or Be components in very wide systems, the decretion disk may reach protoplanetary size during the lifetime of the star. If the mass of the central star is lower than $\sim 10 M_\odot$ [16], a planetary system may be formed.

Another type of purely decretion disk can be formed around stars that form during the coalescences of the components of W UMa systems, which occur when their components lose orbital angular momentum via the magnetic stellar wind [16]. The masses of such coalescence products are 1.5–$3\ M_\odot$. Since such stars have no convective envelopes, and, hence, no efficient magnetic stellar wind, the only way they can get rid of excess angular momentum is through the formation of an extended decretion disk, in which a planetary system can originate.

Protoplanetary gas–dust disks. It is possible to derive the initial distribution of the specific angular momentum in close binaries from studies of the observed distribution of their orbital periods, taking into account observational selection effects [16]. In particular, the interval of specific angular momentum 3×10^{19}–3×10^{20} cm^2/s contains neither binaries nor single stars: such momenta are too low for binaries but too high for single stars. The fraction of stars with planetary systems can be estimated based on the fact that protostars with such angular momenta form single stars with planetary systems [52]; this fraction turns out to be about one-third. Infrared studies of young stars indeed yield similar estimates for the relative fraction of stars with dust envelopes (disks) [53].

It is important for our modeling that the initial size of the disk derived from the above characteristic specific angular momenta of the precursors of planetary systems does not exceed 0.1 AU. However, the decretion part of a DAD disk gradually reaches several hundreds of AU in size, as is observed for the disks of some young T Tauri stars and is needed for the formation of solar-type planetary systems. Observations of circumstellar disks in CO lines have shown that they are turbularized [54]. The turbulence is probably the main origin of their viscosity and expansion [55]. However, magnetic viscosity may also contribute substantially to the evolution of circumstellar protoplanetary disks [56, 57]. In addition, recall that the gaseous component of an extended protoplanetary gas–dust disk around a young star may gradually dissipate under the action of UV radiation, as well as the stellar wind from the central star. For example, modeling of the IR spectrum of the dust disk in HR 4796A yielded estimates of its size ($\sim$70 AU) and of the mass of dust ($\sim$2 of the Earth's mass) [58]. The mass of the gas in the disk does not exceed that of the dust, clearly due to the dissipation of a large

fraction of the gas in this old disk during its previous evolution.

Outbursts of young stars such as FU Ori stars and V1057 may be associated with the non-stationary development of DAD disks around such stars. During these outbursts, the brightness of the disk increases by $5–6^m$ for about a year, then returns to its initial brightness for several decades [59]. The increase of the disk brightness is due to a temporary increase in the accretion rate of the gas to $\sim 10^{-4}\ M_\odot$/yr [60] due to the accumulation instability in the DAD disks around the young accreting stars. The presence of a distant companion in an elliptical orbit can also serve as a trigger for this instability. Note that the semi-major axes of the binary orbits can reach $\sim 10^6\ R_\odot$ and their orbital periods $\sim 3 \times 10^5$ years [16]. Thus, the above mechanism can probably give rise to periodic perturbations of the gravitational potential at the outer edge of the DAD disk around the young accreting star, leading to recurrent outbursts.

Gaseous disks around quasars—accreting supermassive black holes in galactic nuclei. These gaseous DAD disks are responsible for the observed activity of quasars—the brightest quasi-steady-state sources of radiation—which are associated with accreting supermassive ($10^5–10^{10} M_\odot$) black holes in galactic nuclei. The observed brightness variability of quasars provides evidence for variability in their accretion rates. Gas is supplied to the black hole by an extended DAD disk that accumulates gas lost by old stars in the core of the host galaxy. In addition, these stars can lose gas due to dynamical interactions with the DAD disk. Mergers of low-mass satellites with the host galaxies and close interactions with nearby massive galaxies also play substantial roles in intensifying the accretion. The presence of a bar in the central regions can also enhance the accretion of gas by the central black hole. Some of the gas of the DAD disk is accreted by the black hole, providing the high luminosity of the quasar (to $10^{13}\ L_\odot$). The accretion rate needed to provide this luminosity is $\sim 10 M_\odot$/yr, demonstrating that the active stage is short ($\sim 10^8$ years). The radius of such a DAD disk can reach several tens to several hundreds of parsecs. The formation of stars is possible in the outer, relatively cool part of the disk. Such compact, gaseous circumnuclear disks are rich in young stars and are known in numerous galaxies, including our own [61]. The relative number of active nuclei displaying strong absorption indicates that the relative thickness of the gaseous disk around a quasar can reach ~ 0.25 [62].

A gaseous galactic disk. Galactic gaseous disks are the largest known DAD disks. Their sizes vary from several hundreds of parsecs for irregular galaxies to tens of thousands of parsecs for giant spirals. The circular shape of these disks indicates that their formation and evolution are dissipative. In some cases, slight ellipticity with eccentricities of $\sim 0.1–0.16$ [63] is observed, probably due to recent collisions or mergers in these galaxies. Galactic gaseous disks have two main sources of gas: old stars forming planetary nebulae and the accretion of intergalactic gas. Gas can be lost in two main ways: star formation and via the galactic stellar wind. Only a small fraction of the galactic gas (less than $\sim 10^{-3}$) is accreted by the black hole, judging from the observed ratios of the masses of the central black hole and of the galaxy [64].

Gaseous disks in galaxies become turbularized due to outbursts of groups of supernovae in OB associations, which result in the formation of gaseous envelopes hundreds of parsecs in size with velocities of several tens km/s [65, 66]. The estimated time scale for the diffusive evolution of a disk is $\tau_d = R^2/(UH)$, where R is the radius of the gaseous disk, $U = 3 \times 10^6$ cm/s is the velocity of the supernova envelopes, and $H = 300$ pc the thickness of the disk. This is of the order of the Hubble time. It follows that the outer parts of the gaseous disk of the galaxy are formed under the action of the diffusive expansion of the gaseous (and, therefore, also the stellar) disk in the course of the galaxy's evolution. Indeed, the surface brightnesses of disk galaxies decrease exponentially in their peripheries on characteristic scales of ~ 2 kpc [67]. As we will show below, such a distribution is formed by diffusion in the outer parts of a DAD disk. During close encounters between galaxies, the time scale for the turbulent diffusion decreases due to the increase in the characteristic velocities of the turbulence. This ultimately increases the activity of the DAD disk and the brightness of the central region of the galaxy.

3. ANALYTICAL TREATMENT

If we assume that the evolution of gaseous disks is diffusive, we can estimate analytically the main parameters of the disk and their time variations. The basic relation describing the characteristic diffusion time τ_d is obtained via a global "linearization" of the diffusion equations:

$$\tau_d = \frac{R^2}{D} = \frac{l}{U}\left(\frac{R}{l}\right)^2, \qquad (2)$$

where R is the radius of the diffusion penetration zone and $D = Ul$ is the diffusion coefficient. The factor D includes the velocity of the diffusive (turbulent) elements U and their mean free path l. The Keplerian velocity of the gas serves as a natural unit for the local velocity in the disk, and the distance from the gravitating center as a unit of length. Therefore, our description of diffusive disks will assume that the

velocities and mean free paths of turbulent elements can be expressed in the form

$$U = \alpha V, \tag{3}$$

$$l = \beta r^{\gamma}, \tag{4}$$

where $V = (GM_*/r)^{1/2}$ is the Keplerian velocity, r is the distance from the central body, G is the gravitational constant, M_* is the mass of the central body, and α, β, and γ are free parameters. Relations (3)–(4) represent the basic assumptions of our model. Note the fundamental necessity of introducing the two parameters α and β to describe a diffusive disk (for a specified $\gamma = 1$, both parameters are dimensionless); this is due to the fact that, in the general case, the basic components of the diffusion coefficient (the velocity and mean free path of the turbulent elements) are not related to one another and have different dimensions.

Let us consider the evolution of a disk with a given mass. This evolution can be represented as the diffusion of matter originally concentrated within some ring in the vicinity of the star. This model can describe the evolution of the product of the dynamical decay of a companion, or the result of a rapid increase in the viscosity of the gaseous disk (ring) around the accretor. Equation (2) can be used to obtain the time dependence of the size of the decretion part of the disk:

$$R = (\alpha\beta)^{\frac{2}{5-2\gamma}} (GM_*)^{\frac{1}{5-2\gamma}} t^{\frac{2}{5-2\gamma}}. \tag{5}$$

The conservation of angular momentum ($MVR =$ const) can be used to derive the time dependence of the mass of the disk M and the accretion rate $\dot{M}$. Taking into account the fact that most of the disk mass is concentrated near the boundary of the decretion part and that $M \sim R^{-1/2}$, we obtain

$$M \sim t^{\frac{1}{2\gamma-5}}, \quad \dot{M} \sim t^{\frac{6-2\gamma}{2\gamma-5}}. \tag{6}$$

The time dependence of the surface density of the decretion part of the disk $\Sigma \sim M/R^2$ will be

$$\Sigma \sim t^{\frac{5}{2\gamma-5}}. \tag{7}$$

The radial distribution of Σ in the accretion part of the disk can be derived from the condition that the radial flux of matter in the inner parts of the disk be constant. The total flux of matter at a distance r from the star is given by the formula

$$\dot{m}(r) \sim r\Sigma(r)V_d(r). \tag{8}$$

The diffusion velocity V_d for any R can be found from (5):

$$V_d(R) \approx \frac{R}{t} \sim R^{\frac{2\gamma-3}{2}}. \tag{9}$$

Substituting this expression into (8) and assuming that the flux is quasi-steady-state ($\dot{m}(r) =$ const), we obtain

$$\Sigma(r) \sim r^{\frac{1-2\gamma}{2}}. \tag{10}$$

Here, we have studied numerically the evolution of two types of massive-disk models. In the first model, $\gamma = 0$; i.e., the mean free path of a turbulent element is constant along the disk. In this case, relations (5)–(7) reduce to the dependences

$$R \sim (\alpha\beta)^{\frac{2}{5}} t^{\frac{2}{5}}, \quad M \sim t^{-\frac{1}{5}}, \quad \dot{M} \sim t^{-\frac{6}{5}}, \quad \Sigma \sim t^{-1}. \tag{11}$$

The distribution of the surface density in the inner parts of the disk (10) assumes the form

$$\Sigma(r) \sim r^{\frac{1}{2}}. \tag{12}$$

In the second model, we adopt $\gamma = 1$; i.e., the mean free paths of turbulent elements in the disk are proportional to the distance from the central gravitating object. In this case, (5)–(7) can be written in the form

$$R \sim (\alpha\beta)^{\frac{2}{3}} t^{\frac{2}{3}}, \quad M \sim t^{-\frac{1}{3}}, \quad \dot{M} \sim t^{-\frac{4}{3}}, \quad \Sigma \sim t^{-\frac{5}{3}}. \tag{13}$$

The distribution of $\Sigma(r)$ in the accretion part takes the form

$$\Sigma(r) \sim r^{-\frac{1}{2}}. \tag{14}$$

The following interpretation of the models with different values of γ is useful. If we suppose that the mean free path of the turbulent elements is equal to the thickness of the disk, $l \sim H$, which is, in turn, proportional to the distance from the center ($\gamma = 1$), then β remains dimensionless and the product $\alpha\beta$ can be combined into a single parameter. In general, however, the parameters α, β, and γ are determined by the specific physical model considered. For example, when $\gamma = 0$, the thickness of the disk does not depend on the distance from the center, and β becomes dimensional and equal to this thickness. The analytical treatment considered in this section can be used to analyze the results of our simulations.

4. NUMERICAL SIMULATIONS

To study the models described in Section 2, we carried out simulations of the dynamics of several characteristic types of DAD disks. In general, numerical modeling involves the solution of a system of differential equations. We chose a simpler analogous approach. We were able to simplify the modeling based on a physical interpretation of the diffusion, together with the assumptions that there is local conservation of mass and angular momentum and that the velocity field is Keplerian. The partitioning of the computation

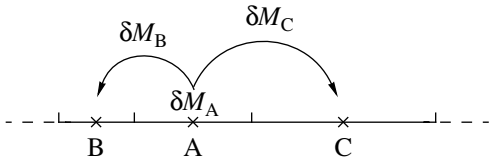

Fig. 1. Schematic illustrating mass transfer between adjacent cells of the computational grid.

domain into cells is an important point in the simulations, and should be based on physical reasoning rather than purely on the accuracy required, as in classical difference schemes.

Let us consider a disk around a star with a mass of M_*. Let the mass of the disk be $M_d \ll M_*$, so that its gravitation can be neglected. The disk is assumed to be geometrically thin, Keplerian, and axially symmetrical. We describe the structure of the disk in terms of the surface density $\Sigma(r)$, where r is the distance from the axis of symmetry. We introduce a numerical grid $\{r_i$, with $i = 0, N\}$ in the interval (r_{in}, r_{out}), which divides the computational domain into annular elements that form the grid cells. The surface density Σ_i is assumed to be constant in each cell, (r_i, r_{i+1}). In this approach, the cell size

$$l_i = r_{i+1} - r_i \tag{15}$$

is equal to the characteristic mean free path of a turbulent element. Let us consider the construction of the corresponding grid for the model with $\gamma = 1$. According to (4), the size of the ith cell can be specified in the form

$$l_i = \beta r_{i+1/2}, \tag{16}$$

where

$$r_{i+1/2} = \frac{1}{2}(r_i + r_{i+1}) \tag{17}$$

is the center of the cell. Combining (15)–(17), we obtain

$$r_i = r_{in}\left(\frac{2+\beta}{2-\beta}\right)^i, \quad i = 0, N. \tag{18}$$

Thus, we obtain for the model with $\gamma = 1$ a nonuniform grid that is denser toward the disk center, while the grid for the model with $\gamma = 0$ is uniform. Along with the surface density Σ_i, the average orbital velocity is also determined in each grid cell

$$V_i = \left(\frac{GM_*}{r_{i+1/2}}\right)^{1/2}, \tag{19}$$

as well as the average turbulent velocity [see (3)]:

$$U_i = \alpha V_i. \tag{20}$$

The computations were organized as follows. We will suppose that we know the $\Sigma_i^{(n)}$ for time $t^{(n)}$. Let us consider a cell A and denote the nearest cells B and C (Fig. 1). We will suppose that a mass δM_A is removed from cell A during the time δt due to turbulent motion. This amount of matter can be determined as follows:

$$\delta M_A = 2\pi r_A \Sigma_A^{(n)} U_A \delta t. \tag{21}$$

The matter leaving cell A is transferred to the two adjacent cells, and this redistribution of the mass must conserve mass and angular momentum. The corresponding equations for the system of three cells can be written

$$\delta M_A = \delta M_B + \delta M_C, \tag{22}$$

$$\delta M_A r_A V_A = \delta M_B r_B V_B + \delta M_C r_C V_C, \tag{23}$$

where δM_B and δM_C are the masses flowing into cells B and C, respectively. Solving these equations for δM_B and δM_C enables us to derive the mass distribution between cells B and C. Having treated all cells $\{i = 1, N\}$ consecutively as cell A and thereby determined all the fluxes $\{\delta M_A(i)$, $\delta M_B(i)$, and $\delta M_C(i)\}$, we can find the surface density distribution $\Sigma_i^{(n+1)}$ for the time $t^{(n+1)} = t^{(n)} + \delta t$:

$$M_i^{(n+1)} = M_i^{(n)} - \delta M_A(i) + \delta M_B(i+1) + \delta M_C(i-1), \tag{24}$$

$$\Sigma_i^{(n+1)} = \frac{M_i^{(n+1)}}{\pi\left(r_{i+1}^2 - r_i^2\right)}, \tag{25}$$

where $M_i^{(n)}$ and $M_i^{(n+1)}$ are the masses of the ith cell at times $t^{(n)}$ and $t^{(n+1)}$, respectively, $\delta M_A(i)$ is the mass outflow from the ith cell, and $\delta M_B(i+1)$ and $\delta M_C(i-1)$ are the masses flowing into the $i+1$th and $i-1$th cells, respectively.

This procedure can be used to derive the surface temperature of the disk T_e from the local conservation of energy. To this end, let us again consider the schematic in Fig. 1. The energy of the state in which an element with mass δM_A is in cell A is equal to

$$\delta E_A = -G\frac{\delta M_A M_*}{r_A} + \frac{\delta M_A V_A^2}{2}. \tag{26}$$

The energy of the state in which the mass δM_A is distributed over the cells B and C is equal to

$$\delta E_{BC} = -G\frac{\delta M_B M_*}{r_B} - G\frac{\delta M_C M_*}{r_C} + \frac{\delta M_B V_B^2}{2} + \frac{\delta M_C V_C^2}{2}. \tag{27}$$

It can be shown that the difference between the final and initial energies of the system is $\delta E_{BC} - \delta E_A < 0$. Since this difference is negative, some energy must be

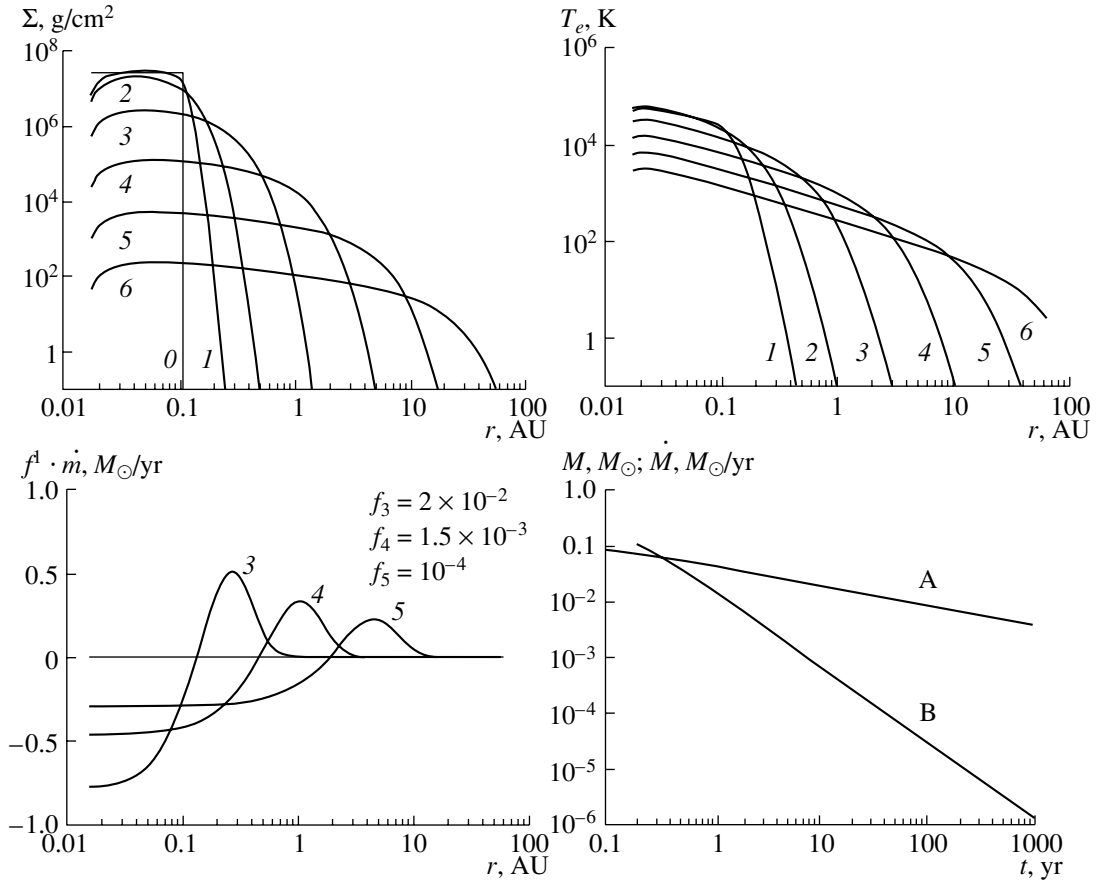

Fig. 2. Evolution of the surface-density distribution (top left), temperature (top right), and local mass flux (bottom left), and the time dependence of the disk mass and the rate of accretion onto the gravitating center (bottom right, curves A and B, respectively) for the model with a massive disk with $M_d = 0.1\ M_\odot$, $\alpha = 0.1$, $\beta = 0.1$, and $\gamma = 1$. The distributions marked by numbers from *0* to *6* correspond to times of 0, 0.01, 0.1, 1, 10, 100, and 1000 years.

released in each such act. The effective temperature can be derived from the condition

$$\frac{\delta E_{\rm A} - \delta E_{\rm BC}}{\delta t \pi \left(r_{i+1}^2 - r_i^2\right)} = 2\sigma T_e^4, \qquad (28)$$

where r_i and r_{i+1} are the inner and outer radii of cell A. Formula (28) specifies the desired effective temperature T_e at a given point of the disk. It is important to understand that the temperature determined in this way may differ substantially from the real local temperature of the DAD disk. This is due to the rapid decrease of this "accretion temperature" with distance in the accretion part of the DAD disk ($T_e \sim r^{-3/4}$) [10] and the even more rapid decrease in the decretion part of the disk (see Figs. 2–5 below). For example, radiation from the accretor or hotter central parts of the disk can substantially alter the temperature distribution in the disk. Indeed, the blackbody temperature of the radiation decreases with distance from the radiating region substantially more slowly: $T \sim r^{-1/2}$. Therefore, modeling real spectra requires a correct solution for the radiation transfer in the disk.

We adopted the condition that the mass outflow $\delta M_{\rm A}$ for each cell over the time δt not exceed one-fifth of the cell's mass as a criteria for determining the computational steps. The test computations indicated that this restriction on the step size was sufficient. Naturally, the time step is determined primarily by the inner cells of the computational domain. The initial and boundary conditions for the computations were specified as part of the formulation of the problem. We consider below the simulation results for four models of astrophysical disks.

A massive disk, $\gamma = 1$. This disk models the evolution of the product of the dynamical disruption of a star, or the development of instability in the accretion disk in a cataclysmic system due to an increase of the viscosity of the disk material. The model parameters for the massive disk were chosen as follows. The mass of the central body (star) is equal to the solar mass, $M_* = 1\ M_\odot$. A disk with uniform surface density in the region $3\ R_\odot < r < 0.1$ AU is specified at the initial time $t = 0$. The condition of free outflow is specified at the inner boundary of the computational

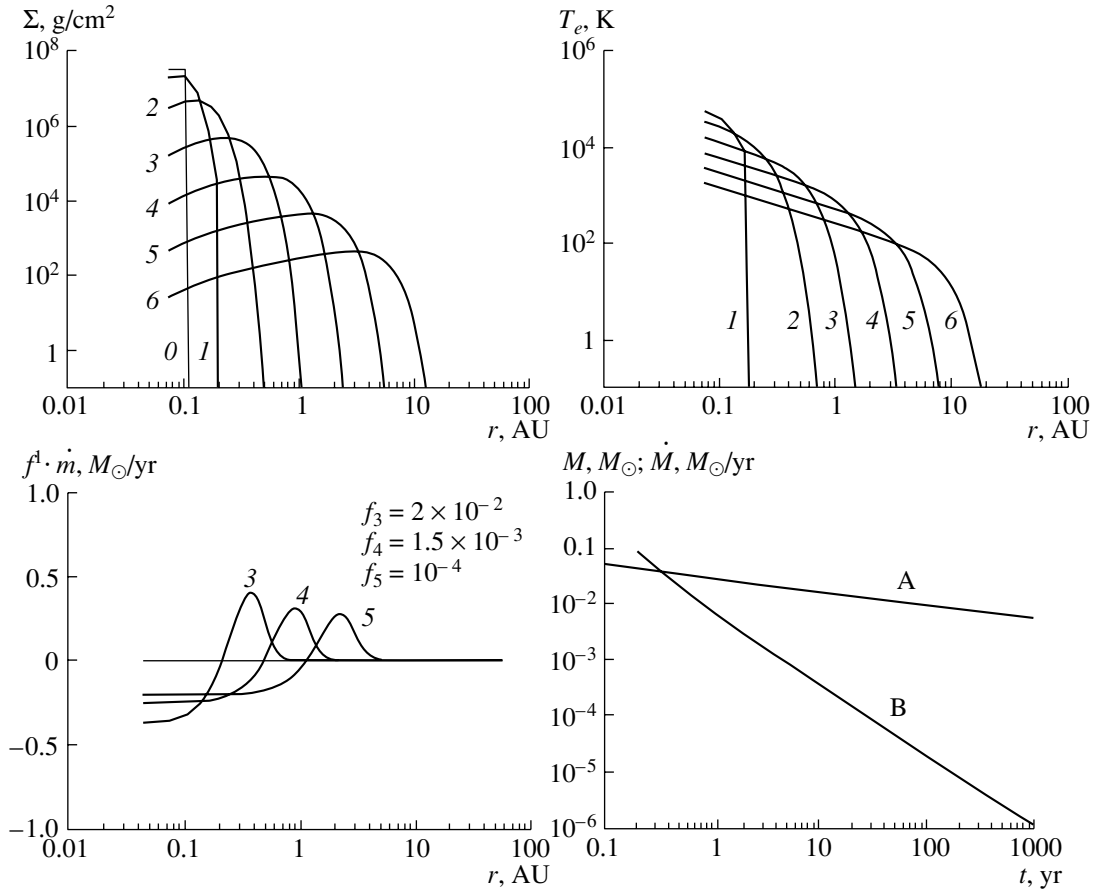

Fig. 3. Same as Fig. 2 for a massive disk with $M_d = 0.1 M_\odot$, $\alpha = 0.1$, $\beta = 0.03$ AU, and $\gamma = 0$.

domain r_{in}, which coincides with the inner boundary of the disk, and at the outer boundary $r_{out} = 60$ AU; i.e., we assume that matter from these boundary layers can freely leave the computational domain and that there is no influx of matter from outside. When $\gamma = 1$, the thickness of the disk increases linearly with distance from the center; the remaining model parameters are $\alpha = 0.1$ and $\beta = 0.1$.

Figure 2 presents the simulation results for the evolution of such a disk. As expected, the characteristic size of the disk R (which can be defined as the region containing most of the disk mass) increases with time, whereas the characteristic density and temperature in the central part of the disk decrease with time. The radial distributions of the total mass flux for various times (bottom left graph in Fig. 2) enable us to distinguish several characteristic zones in the flow structure. In the inner zones, $\dot{m}(r) < 0$; this can be considered the accretion part of the disk. The flux in the inner parts of the accretion zone depends only weakly on r, due to the small characteristic diffusion time in the inner parts of the disk. In the outer zones of the disk, $\dot{m}(r) > 0$; therefore, this part of the disk can logically be considered the decretion part. The density and temperature decrease exponentially in the outer parts of the disk. The mass of the disk and the accretion rate decrease with time.

The above analytical formalism enables us to re-estimate the basic parameters of the disk for other initial disk masses (provided they are still appreciably smaller than the mass of the accreting star) and other values of α and β. It is obvious that the surface density and accretion rate are proportional to the initial mass of the disk, while the volume density of the gas is inversely proportional to its thickness. The effective temperature of the disk is proportional to the mass of the star, $T_e \sim M_*^{1/4}$. In addition, it can be shown [see, for example, (5)] that, for a given value of γ, the solution of the initial system of equations depends on the combination $t/\alpha\beta$. Thus, the distributions obtained for $\alpha = 0.1$ and $\beta = 0.1$ for time t will be equivalent to those for $\alpha^*\beta^*$ for time $t^* = \dfrac{\alpha^*\beta^*}{\alpha\beta} t$, all other factors being the same. Recall that most of the disk mass is contained in the region where $d \ln \Sigma / d \ln r = -2$. It follows from the computations that this region is located in the zone where the mass flux changes its sign.

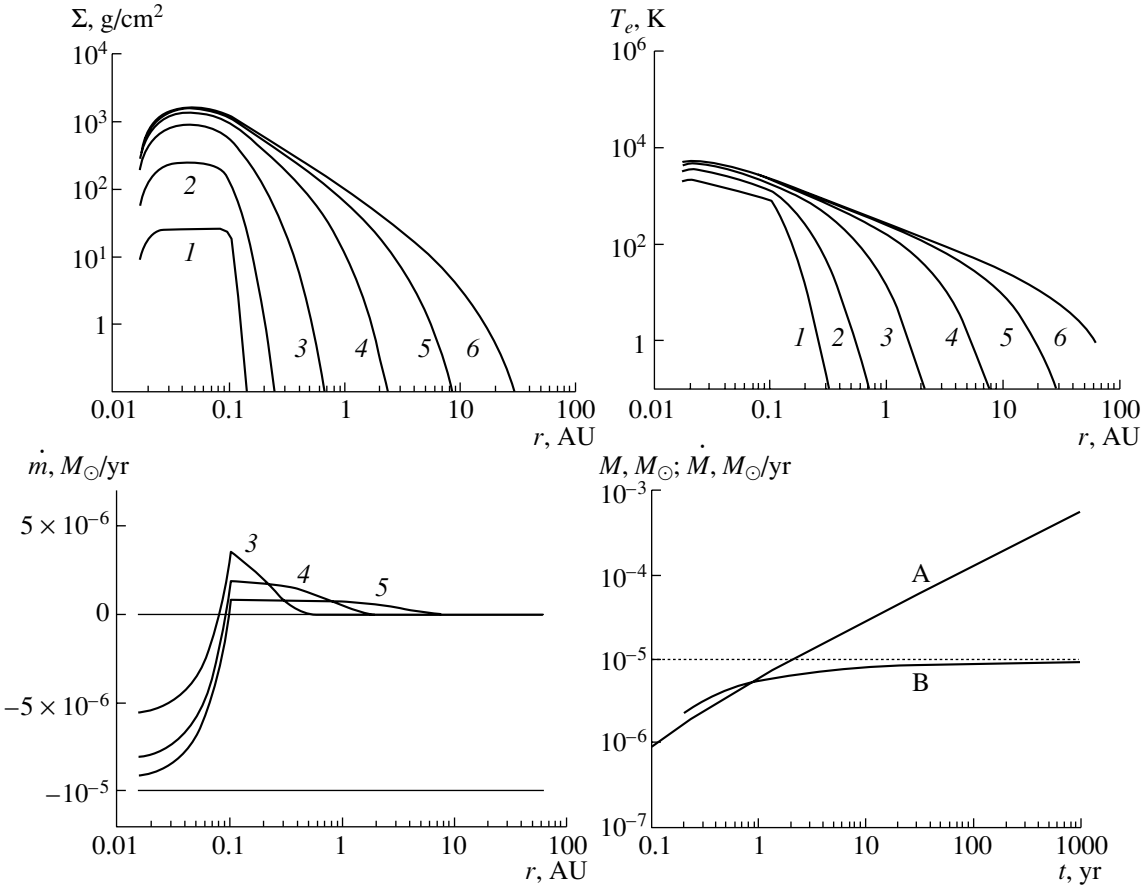

Fig. 4. Same as Fig. 2 for a disk with constant accretion. The model parameters are $\alpha = 0.1$, $\beta = 0.1$, and $\gamma = 1$.

A massive disk, $\gamma = 0$. The boundary and initial conditions in this model are the same as in the previous case, but now $\gamma = 0$; i.e., the mean free path for the turbulent elements (the thickness of the disk) is taken to be constant over the entire disk. The mean free path is specified as $l = \beta = 0.03$ AU. Figure 3 presents the simulation results. A comparison between the distributions $\Sigma(r)$ for this and the previous models reveals a change in the density distribution in the accretion part of the disk. In the model with $\gamma = 0$, the surface density decreases toward the center, reaching a maximum near the boundary of the disk, whereas, in the model with $\gamma = 1$, the density decreases monotonically with distance from the center (with the exception of the most central parts of the disk, which are sensitive to the influence of the boundary conditions).

Note that, for both models ($\gamma = 1$, $\gamma = 0$), the time dependences for the disk mass $M(t)$, accretion rate $\dot{M}(t)$, and disk size $R(t)$, as well as the distributions $\Sigma(r)$ and $T_e(r)$ in the accretion part of the disk, are consistent with the analytical estimates obtained in Section 3. However, the simulations have enabled us to reconstruct the detailed pattern of the disk structure, in particular, we can identify places in the decretion region and transition zone where the direction of the flow changes.

A disk with continuous accretion. Let us consider the evolution of a disk with continuous accretion and a fixed specified angular momentum. We assume that the disk mass at the initial time is $M = 0$ and specify the constant accretion rate $\dot{M}_{out} = 10^{-5}\ M_\odot$/yr in the zone $3\ R_\odot < r < 0.1$ AU. The boundary conditions and other model parameters are the same as for the massive disk with $\gamma = 1$. Figure 4 illustates the evolution of the disk. Note that the disk mass increases as $M \sim t^{2/3}$, while the rate of accretion onto the star gradually approaches the rate of accretion onto the disk. Thus, in the course of the evolution of the system, the decretion rate decreases and the rate of accretion onto the star approaches the specified value. The distribution of matter in the inner accretion part of the disk tends to a steady state. This model may illustrate the origin and evolution of a protoplanetary disk or a disk around the accretor in a symbiotic binary with a relatively small initial size [52].

A decretion disk. We calculated a model for a

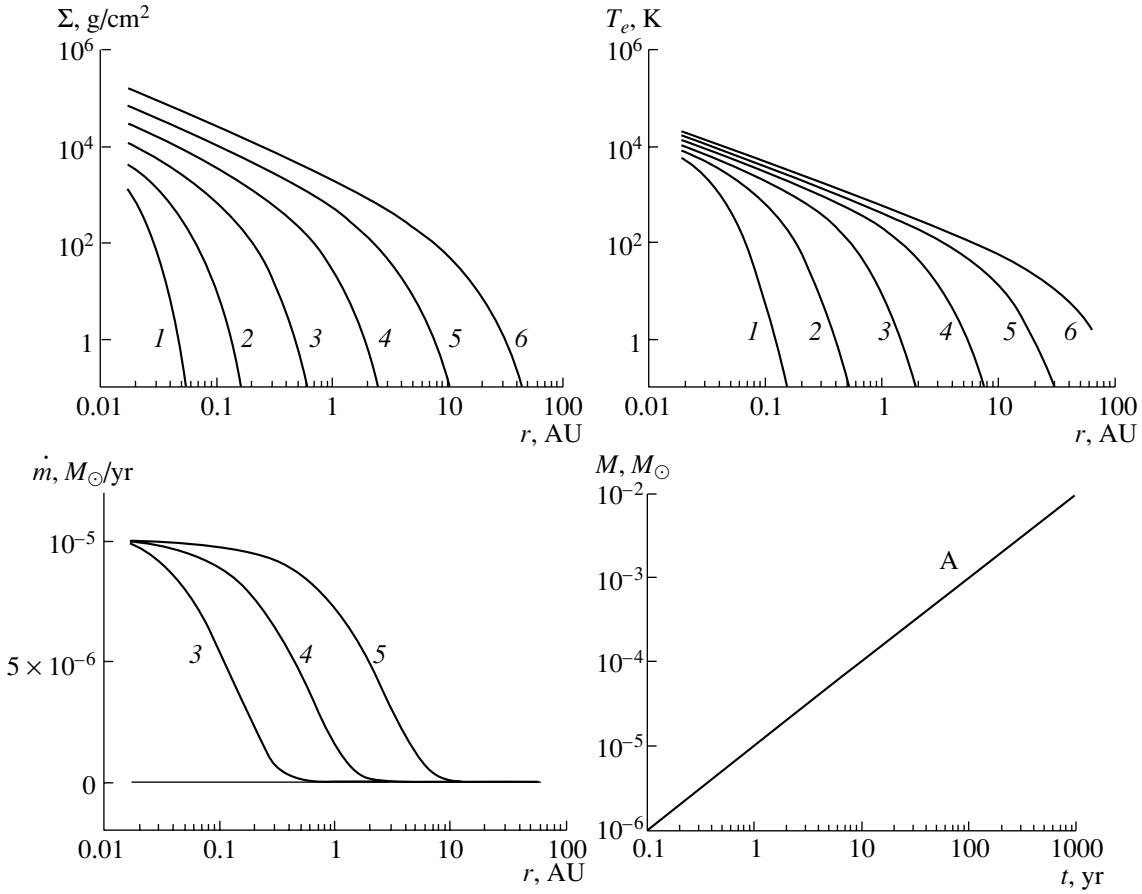

Fig. 5. Same as Fig. 2 for a purely decretion disk. The model parameters are $\alpha = 0.1$, $\beta = 0.1$, and $\gamma = 1$.

purely decretion disk in order to study the origin and development of the decretion disks around Be stars. In this model, we assume that matter and angular momentum are continuously injected from the star into the inner edge of the disk. As a boundary condition, we assume that matter is injected into the first cell of the grid at the rate $\dot{M}_{out} = 10^{-5}\ M_\odot$/yr. The parameters α, β, and γ are the same as for the massive disk with $\gamma = 1$. Figure 5 presents distributions of the basic model parameters for various times and the time dependence of the disk mass. It is obvious that the disk is a pure decretion disk. Note that, as in the case of an accretion disk, the radial dependence of the temperature obeys the law $T_e(r) \sim r^{-3/4}$, and the radiation of the central star can substantially alter the surface temperature of the decretion disk. It is therefore essential to take into account heating of the disk by the radiation of the central star when constructing its continuum spectrum. The basic parameters of the decretion disk can be recalculated following the procedure presented above for the massive disk.

5. CONCLUSION

We have analyzed the basic parameters and evolution of various DAD disks. Such a disk can be divided into an accretion part, where matter is accreted onto the gravitating body and where most of the gravitational energy is released, and a decretion part, where the angular momentum of the accreted gas is accumulated. The turbulent viscosity of the gas is probably the main driving force behind this evolution. In some cases, the magnetic field of the gas disk may also provide an additional source of viscosity in DAD disks. The strong (up to 10^7 G [68]) magnetic field of the accretor—a neutron star or white dwarf—may prevent the formation of a quasi-steady-state accretion disk close to the star's surface. In this case, the matter may be accreted directly onto the magnetic poles of the dwarf or neutron star.

The presence of a magnetic field in the accreted matter is likely. In particular, this field is manifest in the formation of the polar jets observed in various accreting astrophysical objects, such as quasars, microquasars (accreting stellar-mass black holes), accreting neutron stars, and young T Tauri stars. The

formation of jets is probably a result of the electromagnetic acceleration of matter from the inner regions of the accretion part of the DAD disk by the magnetic field, which is amplified by compression and differential rotation. It remains unclear if purely hydrodynamical acceleration of matter as a result of coronal outflows from the accretion disk is possible. A corona should appear due to the dissipation of mechanical energy in the atmosphere of the disk.

The analytical treatment of the evolution of a DAD disk with $\gamma = 1$ yields the relation between the basic dimensionless parameters $\alpha\beta = \tau_K/\tau_{acc}$, where τ_K is the Keplerian time at the disk edge and τ_{acc} is the time for accretion or the duration of an outburst. For cataclysmic binaries with outburst durations of about a month and a Keplerian time for the disk of about an hour, $\alpha\beta \sim 10^{-3}$ in the phase of active accretion during outburst. Since the typical time interval between outbursts is roughly a year [69], $\alpha\beta < 10^{-4}$ during the phase when the critical mass is accumulating in the disk. This example yields an estimate for the amplitude of variations in the viscosity in the disks of cataclysmic binaries. The decretion disks of T Tauri stars increase to sizes of $\sim$100 AU [70] over the stars' lifetimes of several million years. In this case, the above relation imposes the constraint $\alpha\beta \sim 0.0003$.

The binarity of the accreting objects suggests that they may all experience recurrent increases in the activity of their extended gaseous disks. As a rule, the orbits of wide binaries, whether their components are stars or galaxies, have high eccentricities. When objects with disks approach their companions, the gas viscosity increases and the disk evolution accelerates. This enhances accretion in the disks of binaries or star formation in galaxies. Indeed, as a rule, galaxies with a high star-formation rate are binary.

The temperatures in the decretion parts of extended DAD disks are low, which may lead to the condensation of dust. Consequently, the disk becomes optically opaque. The estimated optical depth in the plane of the disk is $\tau \sim 100\Sigma/\beta(\gamma = 1)$, while $\tau \sim 100\Sigma$ in the polar direction. Figures 2–5 show that even extended disks are optically thick in their peripheral parts. Therefore, the emission of some Be stars with their DAD disks viewed edge-on may be substantially weakened at optical wavelengths. Indeed, the presence of dust around Be stars is confirmed by their IR excesses [71]. In particular, the Beklyn-Neugebauer object, displaying an optical absorption of $\sim 17^m$ and a temperature of $\sim$55 K [72], may be a Be star with a mass of $7M_\odot$ and a gas–dust disk with $\Sigma \sim 0.2\beta$ and $M_d \sim \beta R_d^2$ viewed edge-on.

ACKNOWLEDGMENTS

This work was supported by the Russian Foundation for Basic Research (project no. 02-02-17524, 03-02-16254, NNIO-02-02-04008), the Federal Science and Technology Program in Astronomy, and a grant in support of Leading Scientific Schools of the Russian Federation (NSh-162.2003.2).

REFERENCES

1. V. S. Safronov, *Evolution of a Protoplanetary Cloud and the Formation of the Earth and Planets* (Nauka, Moscow, 1969) [in Russian].
2. M. Laplace, *Exposition du système du monde*, 3rd Ed. (Chez Courcier, Paris, 1808; Obshchestvennaya Pol'za, St. Petersburg, 1861), Vols. 1, 2.
3. F. Hoyle, Quart. J. Roy. Astron. Soc. **1**, 28 (1960).
4. O. Struve, Astrophys. J. **73**, 94 (1931).
5. G. P. Kuiper, Astrophys. J. **93**, 133 (1941).
6. J. Crawford, Astrophys. J. **121**, 71 (1955).
7. Ya. B. Zel'dovich, Dokl. Akad. Nauk SSSR **155**, 67 (1964).
8. E. E. Salpeter, Astrophys. J. **140**, 796 (1964).
9. D. Lynden-Bell, Nature **223**, 690 (1968).
10. N. I. Shakura, Astron. Zh. **49**, 921 (1972).
11. G. S. Bisnovatyi-Kogan and S. I. Blinnikov, Astron. Astrophys. **59**, 111 (1977).
12. G. S. Bisnovatyi-Kogan and R. V. Lovelace, New Astron. Rev. **45**, 663 (2001).
13. D. V. Bisikalo, A. A. Boyarchuk, O. A. Kuznetsov, *et al.*, Astron. Zh. **72**, 190 (1995) [Astron. Rep. **39**, 167 (1995)].
14. D. V. Bisikalo, A. A. Boyarchuk, V. M. Chechetkin, *et al.*, Mon. Not. R. Astron. Soc. **300**, 39 (1998).
15. I. Iben and A. V. Tutukov, Astrophys. J., Suppl. Ser. **54**, 335 (1984).
16. A. G. Masevich and A. V. Tutukov, *Stellar Evolution: Theory and Observations* (Nauka, Moscow, 1988) [in Russian].
17. A. Goodman, P. Benson, G. Fuller, *et al.*, Astrophys. J. **406**, 528 (1993).
18. B. Kane and D. Clemens, Astron. J. **113**, 1799 (1997).
19. Ya. N. Pavlyuchenkov and B. M. Shustov, Astron. Zh. **81** (2004, in press).
20. K. H. Predergast and G. R. Burbidge, Astrophys. J. **151**, L83 (1968).
21. D. Lynden-Bell and J. E. Pringle, Mon. Not. R. Astron. Soc. **168**, 603 (1974).
22. A. M. Fridman, A. Khorughii, and E. Polyachenko, Space Sci. Rev. **102**, 51 (2002).
23. D. V. Bisikalo, A. A. Boyarchuk, P. N. Kaĭgorodov, *et al.*, Astron. Zh. (2004, in press).
24. A. V. Tutukov, in *3rd Decimal US-USSR Conference on CETI*, Ed. by G. Shostak (1983), p. 195.
25. A. M. Fridman and N. Gorkavyi, *Physics of Planetary Rings* (Springer, 1999).
26. P. Goldreich and S. Tremaine, Icarus **34**, 227 (1978).
27. A. Wisdom and S. Tremaine, Astron. J. **95**, 925 (1988).

28. J. Hahn and E. Gallo, Bull. Amer. Astron. Soc. **34**, 892 (2002).
29. H. Daisaka, H. Tanaka, and S. Ida, Bull. Amer. Astron. Soc. **32**, 1089 (2000).
30. I. Mosqueira, P. Estrada, and L. Brookshaw, Icarus **139**, 260 (1999).
31. J. Hertzsch, H. Scholl, F. Spanm, *et al.*, Astron. Astrophys. **320**, 319 (1997).
32. L. Molnar and D. Dunn, Bull. Amer. Astron. Soc. **48**, 1126 (1996).
33. J. Colwell, Planet. Space Sci. **42**, 1139 (1994).
34. I. Iben and A. Tutukov, Astrophys. J., Suppl. Ser. **54**, 335 (1984).
35. G. Nelemans, P. Jonker, T. Marsh, *et al.*, Mon. Not. R. Astron. Soc. **348**, L7 (2004).
36. A. V. Fedorova, D. V. Bisikalo, A. A. Boyarchuk, *et al.*, Astron. Rep. **44**, 309 (2000).
37. I. Iben, A. Tutukov, and A. Fedorova, Astrophys. J. **486**, 955 (1997).
38. A. A. Boyarchuk, Vopr. Kosmogonii, No. 7, 231 (1960).
39. A. A. Boyarchuk, *Cosmical Gas Dynamics* (Nauka, Moscow, 1972) [in Russian], p. 329.
40. A. V. Tutukov and L. R. Yungel'son, Astrofizika **8**, 381 (1972).
41. D. V. Bisikalo, A. A. Boyarchuk, E. Yu. Kil'pio, and O. A. Kuznetsov, Astron. Rep. **46**, 1022 (2002).
42. K. Hodapp, Ch. Walker, B. Reipurth, *et al.*, Astrophys. J. **601**, L79 (2004).
43. A. Quillen, P. Varniero, I. Minchev, *et al.*, astro-ph/0312647.
44. O. Struve, Astrophys. J. **93**, 104 (1941).
45. A. V. Tutukov, Nauchn. Inform. Astron. Soveta Akad. Nauk SSSR, No. 11, 62 (1969).
46. A. V. Tutukov and A. V. Fedorova, Astron. Rep. **47**, 826 (2003).
47. A. Okazaki, Publ. Astron. Soc. Jpn. **53**, 119 (2001).
48. A. Okazaki, M. Bate, G. Ogilvie, *et al.*, Mon. Not. R. Astron. Soc. **337**, 967 (2002).
49. P. Harmanec, D. Bisikalo, A. Boyarchuk, *et al.*, Astron. Astrophys. **396**, 937 (2002).
50. C. Miller and J. Marlborough, Astrophys. J. **494**, 715 (1998).
51. C. Miller and J. Marlborough, Astrophys. J. **516**, 276 (1999).
52. A. V. Tutukov, Astron. Vestn. **21**, 299 (1987).
53. S. Beckwith and A. Sargent, in *Protostars and Planets III,* Ed. by E. Levy and J. Lunine (UAP, Tucson, 1993), p. 521.
54. J. Carr, A. Tokunaga, and J. Najita, Astrophys. J. **603**, 213 (2004).
55. D. Lin and J. Papaloizou, Mon. Not. R. Astron. Soc. **191**, 37 (1980).
56. S. Balbus and J. Hawley, Astrophys. J. **376**, 214 (1991).
57. T. Sano, S. Inutsuka, N. Turner, *et al.*, astro-ph/0312480.
58. T. Currie, D. Semenov, T. Henning, *et al.*, ASP Conf. Ser. **294**, 265 (2003).
59. C. Aspin and B. Reipwith, Astron. J. **126**, 2936 (2003).
60. L. Hartmann and S. Kenyon, Astrophys. J. **299**, 462 (1985).
61. R. Genzel, R. Schodel, T. Ott, *et al.*, Astrophys. J. **594**, 812 (2003).
62. A. Caccianiga, P. Severgnini, V. Braito, *et al.*, astro-ph/0312344.
63. B. Ryden, Astrophys. J. **601**, 214 (2004).
64. R. McLure and J. Dunlop, Mon. Not. R. Astron. Soc. **331** (3), 795 (2002); astro-ph/0201081.
65. I. Igumenschev, B. Shustov, and A. Tutukov, Astron. Astrophys. **234**, 396 (1990).
66. M. MacLow, astro-ph/0311032.
67. B. Robertson, N. Yoshida, V. Springel, *et al.*, astro-ph/0401252.
68. C. Brinkworth, M. Burleigh, G. Wynn, *et al.*, Mon. Not. R. Astron. Soc. **348**, L33 (2004).
69. T. Kato, P. Nelson, and C. Stockdale, Mon. Not. R. Astron. Soc. **347**, 861 (2004).
70. K. Hodapp, Ch. Wakker, B. Reiperth, *et al.*, Astrophys. J. **601**, L79 (2004).
71. L. Waters, Astron. Astrophys. **162**, 121 (1986).
72. J. Tan, astro-ph/0401552.

Translated by K. Maslennikov

Astronomy Reports, Vol. 48, No. 10, 2004, pp. 813–825. Translated from Astronomicheskiĭ Zhurnal, Vol. 81, No. 10, 2004, pp. 895–908.

Dissipation of the Hot Dust Envelope of CH Cygni (1996–2003)

O. G. Taranova and V. I. Shenavrin

Sternberg Astronomical Institute, Universitetskiĭ pr. 13, Moscow, 119992 Russia

Received January 20, 2004; in final form, March 15, 2004

Abstract—Our analysis of *JHKLM* photometric data obtained in 1978–2003 for the CH Cyg system shows that the "local" dust envelope that formed in the system in 1986 and reached its highest column density in 1996 had largely dispersed by mid-2001, so that the observed brightness of the system's red giant has returned to its pre-1985 level. The giant's spectral type varied in the range M6.5–M7.5 in 2001–2003. The optical depth of the dust envelope at 1.25 μm was $\tau(J) \approx 0.83$ near JD 2450090. The increase in the dust envelope's optical depth was approximately a factor of 2.3 slower than the decrease. The envelope of CH Cyg can be pictured as a "stationary" dust cloud with an optical depth at $\lambda = 1.25$ μm of $\sim$0.4 and a dust-grain temperature of $\sim$750–800 K. There was probably an injection of matter into this cloud toward the end of 1985, initiating the condensation of dust grains. The optical depth began to increase and, by 1991, the dust envelope was transformed from a cloud into a local, almost spherically-symmetric envelope with a grain temperature of 750–800 K. Its optical depth reached its maximum in 1996, after which the local envelope began to disperse, becoming a cloud again by 2001. The detected 4000-day variability of the *JHK* brightness of CH Cyg is in good agreement with a model with an eclipsing binary consisting of two cool giants with effective temperatures differing by approximately 100 K, a luminosity ratio of $L(\mathrm{M7})/L(\mathrm{M6}) \sim 6.8$, and a radius ratio of $R(\mathrm{M7})/R(\mathrm{M6}) \sim 3.6$. The orbital ephemeris is given by JD (Min I) $= 2444180 + 4000E$. © *2004 MAIK "Nauka/Interperiodica".*

1. INTRODUCTION

It is currently generally believed that the binary CH Cyg is the only triple system among the known symbiotic stars. The triple nature of the system was first noted by Hinkle *et al.* [1]; in their model, the inner pair is a symbiotic system (with a period of $\sim$756 days), and the third component, which is a red or brown dwarf, is in an outer orbit (with a period of $\sim$5300 days). Hinkle *et al.* [1] believed in 1993 that the system was not eclipsing. However, in 1996, Skopal *et al.* [2] noted that eclipses were possible, and suggested that there were two cool giants in the system: one associated with the symbiotic pair, and the other in the outer orbit. In their model, a massive ($\sim 4M_\odot$) cool giant orbits the symbiotic pair, which consists of a red giant with a mass of $\sim 1M_\odot$ and a main-sequence dwarf (the hot component). The hot component undergoes outbursts due to the accretion of matter from the red giant. Numerical modeling of such systems by Mikkola and Tanikawa [3] demonstrates that a system with components of this type should not be stable, and they suggest that models with two cool giants are implausible. Mikkola and Tanikawa [3] consider the model of Hinkle *et al.* [1] to be more acceptable with regard to stability, although details of the model need to be refined. For example, we can consider the following possibility: a symbiotic pair consisting of a cool giant and a faint star of unknown nature ($3M_\odot + 0.5M_\odot$) + a third star (probably a white dwarf, $0.9M_\odot$). The orbits are eccentric, and the hot star is active when the components approach each other.

Analysis of our spectroscopic and photometric observations of CH Cyg in 1978–1989 indicates that the symbiotic system's cool component is a late-type (M5–M7), giant, semiregular variable. We first detected the presence of a hot circumstellar dust envelope in 1985, at the end of an optical outburst. The results of our many-year (1978–1998) infrared and optical observations of CH Cyg [4] show that the character of the brightness and color variations of the system in the IR in 1978–1998 are generally consistent with the observed radiation being emitted by a source surrounded by a dust envelope with variable optical depth.

This paper presents the results of our analysis of further IR photometric observations of CH Cyg carried out in 1999–2003.

2. OBSERVATIONS

We obtained our infrared photometric data for CH Cyg on the 125 cm telescope of the Sternberg Astronomical Institute's Crimean station using an InSb photometer. The uncertainties of these observations were $0.01–0.05^m$ in all filters. A description

1063-7729/04/4810-0813$26.00

Table 1. *JHKLM* photometry of CH Cyg in 1999–2003

JD 2440000+	J	H	K	L	M
11180	0.8	−0.26	−0.73	−1.5	−1.44
11300	0.74	−0.22	−0.76	−1.38	−1.48
11336	0.76	−0.24	−0.75	−1.45	−1.32
11352	0.79	−0.29	−0.76	−1.51	−1.37
11359	0.78	−0.28	−0.79	−1.49	−1.4
11367	0.79	−0.25	−0.74	−1.52	−1.41
11384	0.82	−0.26	−0.72	−1.47	−1.38
11387	0.82	−0.23	−0.67	−1.49	−1.44
11420	0.82	−0.24	−0.73	−1.48	−1.34
11448	0.77	−0.28	−0.77	−1.51	−1.38
11452	0.73	−0.32	−0.79	−1.51	−1.45
11456	0.72	−0.27	−0.76	−1.52	−1.48
11475	0.82	−0.27	−0.73	−1.55	−1.64
11505	0.7	−0.35	−0.83	−1.59	−1.51
11524	0.71	−0.33	−0.8	−1.56	−1.52
11549	0.76	−0.28	−0.77	−1.53	−1.45
11642	0.73	−0.32	−0.74	−1.6	−1.52
11684	0.87	−0.14	−0.67	−1.51	−1.52
11706	0.85	−0.13	−0.58	−1.49	−1.56
11710	0.86	−0.12	−0.6	−1.49	−1.5
11737	0.86	−0.11	−0.62	−1.46	−1.49
11743	0.89	−0.15	−0.6	−1.46	−1.47
11769	0.93	−0.09	−0.58	−1.46	−1.47
11778	0.93	−0.09	−0.56	−1.44	−1.51
11824	0.86	−0.15	−0.62	−1.48	−1.51
11853	0.9	−0.13	−0.6	−1.44	−1.4
11866	0.9	−0.14	−0.6	−1.42	−1.45
11887	0.91	−0.11	−0.57	−1.5	−1.48
11902	0.84	−0.18	−0.64	−1.46	−1.44
11952	0.77	−0.27	−0.73	−1.47	−1.47
11983	0.76	−0.28	−0.73	−1.52	−1.5
12008	0.68	−0.35	−0.79	−1.52	−1.48
12032	0.66	−0.35	−0.78	−1.5	−1.53
12071	0.75	−0.28	−0.72	−1.46	–
12122	0.75	−0.29	−0.7	−1.39	−1.22
12133	0.69	−0.32	−0.73	−1.46	−1.4
12158	0.66	−0.35	−0.81	−1.44	−1.4
12188	0.64	−0.36	−0.78	−1.46	−1.35
12210	0.65	−0.34	−0.76	−1.42	−1.39
12421	0.78	−0.19	−0.62	−1.31	−1.26
12455	0.78	−0.2	−0.61	−1.37	−1.24
12489	0.74	−0.26	−0.66	−1.37	−1.25
12511	0.8	−0.19	−0.64	−1.35	−1.32
12518	0.78	−0.23	−0.6	−1.33	−1.26
12539	0.84	−0.16	−0.6	−1.29	−1.22
12600	0.75	−0.24	−0.72	−1.39	−1.29
12717	0.7	−0.31	−0.73	−1.4	−1.34
12752	0.73	−0.31	−0.71	−1.4	−1.32
12774	0.73	−0.3	−0.72	−1.37	−1.35
12800	0.65	−0.35	−0.77	−1.43	−1.35
12832	0.63	−0.38	−0.80	−1.45	−1.39
12870	0.66	−0.36	−0.78	−1.46	−1.38
12892	0.65	–	−0.78	−1.43	−1.39
12921	0.63	−0.38	−0.78	−1.47	−1.42

of our observing techniques, the instrumental parameters, and the observational data for 1978–1995 can be found in [4–6].

Table 1 presents our 1999–2003 data for CH Cyg. Our data for the entire time interval covered by available observations are shown in Fig. 1 as light and color curves. The horizontal dashed lines show the corresponding color indices for a normal M6 giant [9]. The data analyzed in [4] lie to the left of the vertical dotted line. The $U-B$ color indices after 1998 are taken from Skopal *et al.* [7, 8].

3. DISCUSSION

3.1. The Photometric State of the CH Cyg System in 1998–2003

We can see from Fig. 1 and Table 1 that the system's IR brightness and colors had almost returned to their 1982–1984 levels by 2001, and stayed at these levels until the end of 2003. The *JHK* brightnesses gradually increased (by 0.20^m–0.25^m in J) from mid-1996 to 2001, whereas $J-H$ decreased. These gradual changes were accompanied by brightness variations on a time scale of 600–800 days with an amplitude of several tenths of a magnitude. The brightness at 3.5–5 μm (the L and M filters) and the $L-M$ color index decreased from 1996 to 2001.

In the optical, the hot component has remained in a state of low activity since the fall of 1999 (Fig. 1). However, the $U-B$ values were already approaching those characteristic of cool giants by mid-2000, and there were no reports of new activity of the hot component in the CH Cyg system after 2001. Note that the increase in the column density of the dust component in 1986–1996 was accompanied by repeated outbursts of optical activity (Fig. 1, the variations of $U-B$); the activity of the hot component was low during the dissipation of the dust envelope, and this activity had probably completely ceased by 2001.

The characteristics of the radiation from CH Cyg in 1999–2003 suggest that the "local" dust envelope that formed in the system in 1986 and achieved its highest column density in 1996 [4] had been largely dispersed by mid-2001, with the brightness of the system's cool giant returning to its pre-1985 level. This is clearly visible in Fig. 2, where the solid curve is the J light curve and the open circles and asterisks show variations of the K and M brightnesses, respectively, reduced to the 2002–2003 J brightness level of CH Cyg. Figure 2 indicates that the spectral energy distribution of CH Cyg at 1.25–5 μm is the same from 1975 to late 1985 and after 2001, within the errors. A redistribution of the energy in the near-IR started by the end of 1985 and continued until 2000 (the interval between the dashed lines in Fig. 2). Thus, all the unusual phenomena that had been manifest

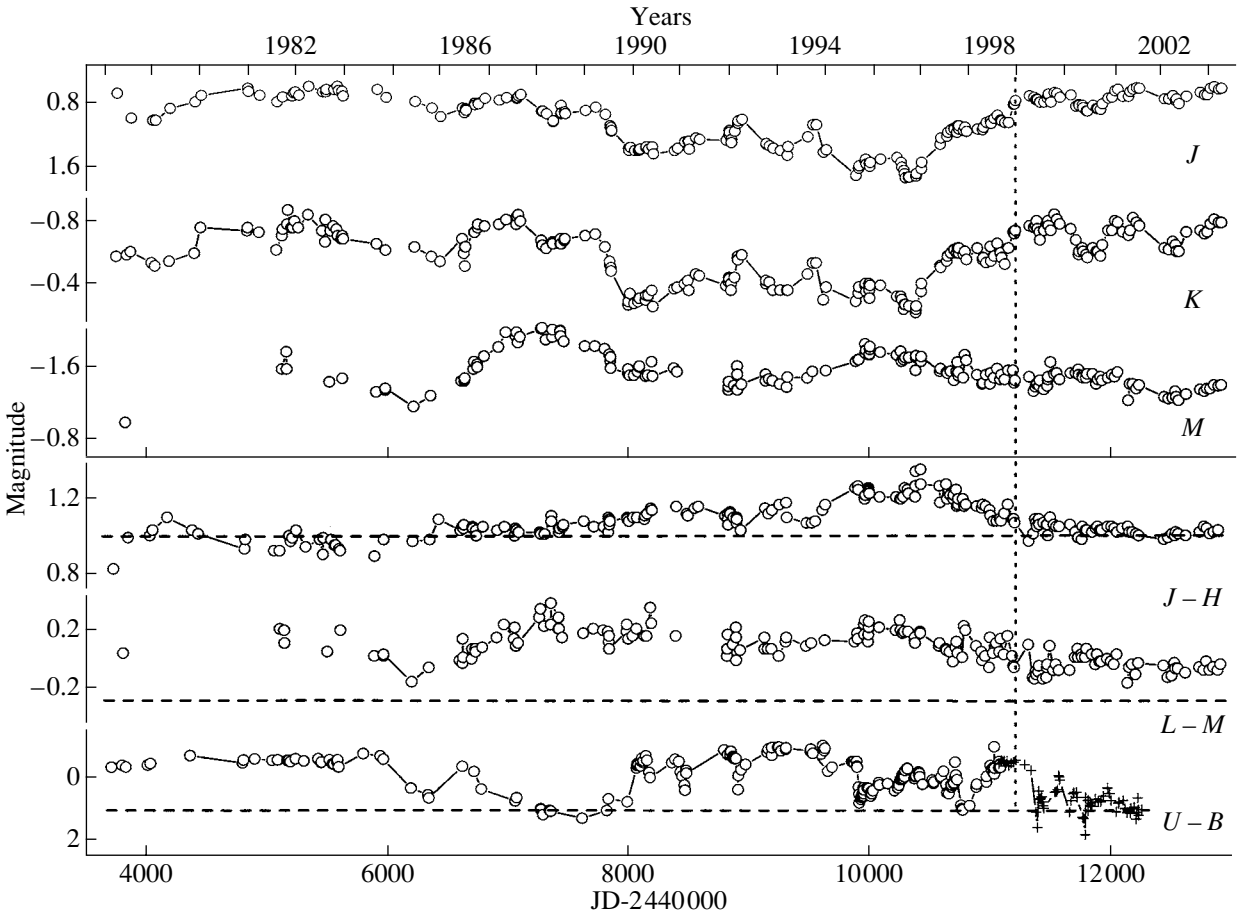

Fig. 1. Variations of the *JKL* brightnesses and the $J-H$, $L-M$, and $U-B$ color indices for CH Cyg in 1978–2003. The open circles show our own data, and the asterisks show the data of Skopal *et al*. [7, 8]. The observations of 1999–2003 lie to the right of the vertical dotted line. The dashed lines show the color indices for an M6 giant.

in the *JHKLM* radiation of the CH Cyg system since 1985 were absent by 2001, and we can now undertake a general analysis of what happened to the system's cool sources over nearly 15 years.

3.2. The System's Cool Component

Figure 3 presents two-color diagrams relating the optical and IR data for CH Cyg. The $B-V$ and $V-J$ color indices prior to 1998 are from our observations; the *UBV* photometry data of Skopal *et al*. [7, 8] were used between 1998 and 2001. The dashed curves show the two-color relations for normal M0–M6 giants [9, 10] and late M7–M8 giants [11]. The data obtained with the *BV* photometry of Skopal *et al*. [7, 8] are plotted as asterisks. The asterisks connected with line segments correspond to the 2001 data. The solid arrow in the graphs shows the color changes that occur when the interstellar reddening changes by $E(B-V)=0.5^m$. Figure 3 shows that the observed variations of $J-H$ and $V-J$ can be described using a model with a variable source (red star) and a dust component with variable optical depth in the line of sight [4–6]. The optical depth of the dust component, which consists of dust grains similar to interstellar grains, could be as high as $E' \sim 1.5^m$. The spectral type of the variable source (red giant) changed from M5 to M7.5 during our observations. Considering only the data for 2001, when the dust envelope had nearly completely dissipated and the hot component's activity was close to its minimum, we find that the giant's spectral type varied in the range M6.5–M7.5. The two short-dashed lines in the upper panel of Fig. 3 are the extremes of the cool star's position on the curve for cool giants, based on the 2001 observations. In other words, if the cool component has a spectral type earlier than M6.5III [the $(J-H)$–$(V-J)$ diagram in Fig. 3], this could be due to additional light in the V filter when the hot component is in outburst. This contribution is clearly visible in the variations of $B-V$ (lower panel of Fig. 3), with $B-V$ systematically deviating toward "hotter" values.

If the system's cool star is a normal giant, then

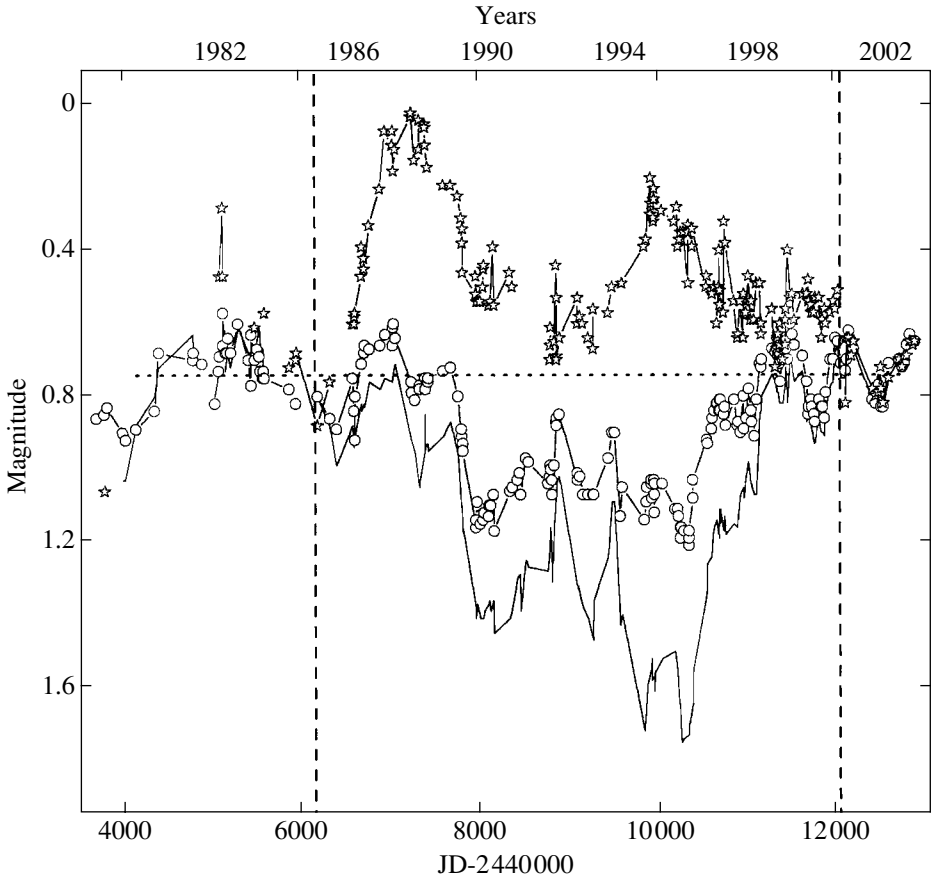

Fig. 2. 1978–2003 variations of the J brightness of CH Cyg (solid curve) and variations of the K and M brightnesses reduced to the J-brightness level for 2002–2003 (open circles and asterisks, respectively).

the color excess of the mean $J-H$ color index in 2001, when the dust envelope had dissipated, can be used to estimate the interstellar reddening of CH Cyg. We estimate based on the mean values of $J-H$, $V-J$, and $B-V$ for four sets of IR observations and six sets of UBV observations in 2001 $E(B-V) = 0.11^m \pm 0.01^m, 0.16^m \pm 0.05^m, 0.11^m \pm 0.03^m$. These estimates nearly coincide with the reddening we adopted from Kenyon [12].

3.3. The Parameters of the Local Dust Envelope

Let us consider the data at 1.25–1.65 μm (the J and H filters). We have noted earlier [4–6] that only the system's cool component (red giant) radiates at these wavelengths, with its light possibly attenuated by the dust envelope. Even in the active state of the hot component, the direct contribution of its light at wavelengths $\lambda > 1$ μm does not exceed 1–2%; it may have been significant in the J filter only at the activity peak of 1982–1984, when the red giant was classified as an M5 based on the $J-H$ color index.

Figure 4 displays the JH and $J-H$ variations for the entire time covered by the observations. These curves clearly show at least two components: a slow one with a time scale of about 6000 days, and a fast one with a time scale of several hundred days. We approximated the slow component with polynomials of various orders. The ninth-order (and higher-order) curves for 1986–2000 virtually coincide with the linear approximations for two intervals: 1986–1996 (the descending branch) and 1996–2000 (the ascending branch). In the corresponding light curves in the figure, the ninth-order curve is plotted as a dotted curve and the regression lines as solid line segments.

The short-dashed line in the bottom panel corresponds to $J-H$ for an M6–M7 red giant [11]. Based on the character of the JH and $J-H$ color variations on the descending and ascending branches of the slow component, we conclude that the most probable origin of the observed variations (the decrease and then increase of the JH brightness, with simultaneous reddening and bluing) is an increase and then decrease of the optical depth of the dust envelope that began to form in the system in 1986. Note that, although this interpretation of the observed JH and $J-H$ variations appears to be the most probable one, it is not the only possible explanation if only the

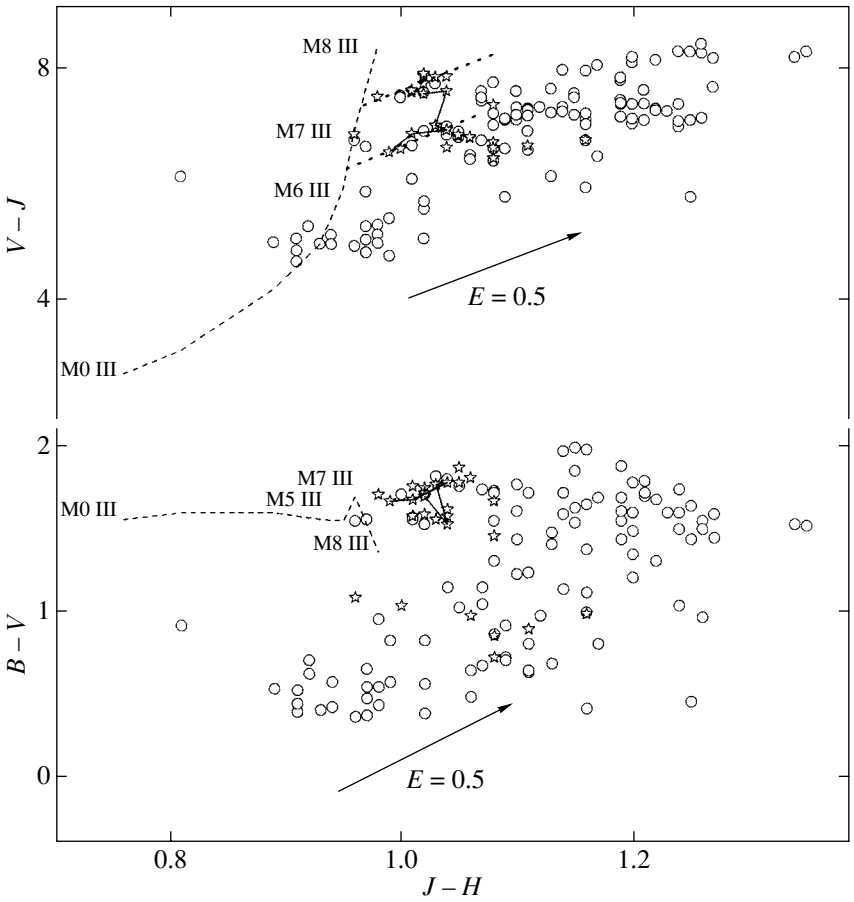

Fig. 3. $(J-H, B-V)$ and $(J-H, V-J)$ two-color diagrams based on observations of CH Cyg in 1978–2003. The dashed curves show the two-color relations for normal M0–M8 giants. The asterisks show the two-color relations obtained using the *BV* photometry of Skopal *et al.* [7, 8]. The asterisks connected with line segments correspond to observations obtained in 2001. The solid arrows show the color changes that result when the interstellar reddening changes by $E(B-V) = 0.5^m$.

JH photometric data are considered. For example, the effects observed at 1.25–1.65 μm can be obtained by changing the temperature of the red giant itself (by approximately 400–500 K within a color-temperature range of 2300–2800 K). However, conclusive evidence in favor of the dust-envelope interpretation is provided by the *LM* and $L-M$ variations, especially in 1996–2000 (the ascending branch: dispersion of the dust envelope). During this period, the dust envelope was dissipating, and a decrease of $J-H$ and an increase of the *JH* brightness were observed. The *LM* and $L-M$ variations support this picture: the dust envelope's optical depth was decreasing, together with its radiation at 3.5 and 5 μm (the *LM* filters). If the cool star's temperature were increasing (the ascending branch), the *LM* brightness should also increase. Thus, the observed gradual decrease of the *JH* brightness in 1986–1996 and its subsequent increase in 1996–2000 are due to the formation of a local dust envelope in 1986, whose density increased until 1996, and the subsequent nearly complete dissipation of the envelope by 2001. The parameters for a linear approximation of the *JH* and $J-H$ variations on the descending and ascending branches of the light and color curves in the form $Y = A + BX$ are presented in Table 2. Let us suppose that the gradual changes of the *JH* brightness are due solely to variations of the dust envelope's optical depth. In this case, these variations should be proportional to the optical depth of the dust envelope, i.e.

$$\Delta J = B(J)X \propto \tau(J) \propto Q(J),$$
$$\Delta H = B(H)X \propto \tau(H) \propto Q(H)$$

and

$$(\Delta J/\Delta H) = B(J)/B(H) = Q(J)/Q(H),$$

where $Q(\lambda)$ is the absorption efficiency of the dust grains, whose wavelength dependence can be represented $Q(\lambda) \propto \lambda^{-\alpha}$. The parameter α depends primarily on the type of dust grain. The $B(J)/B(H)$ values derived from Table 2 are 1.38 ± 0.13 for the

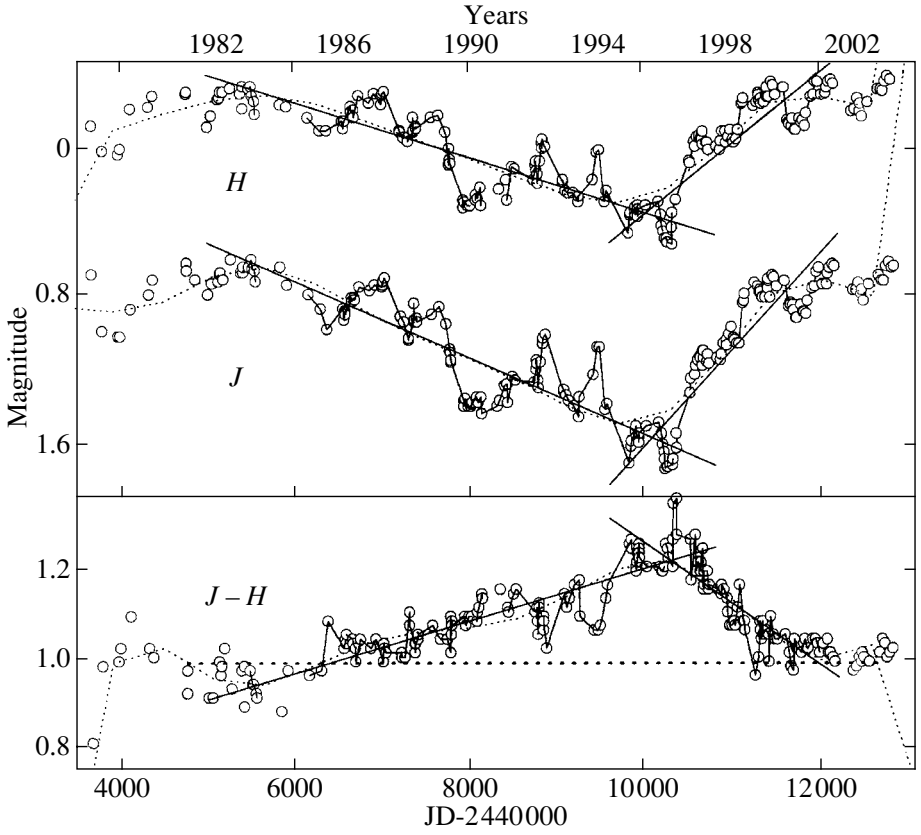

Fig. 4. *JH* brightnesses and $J - H$ color variations (open circles) for CH Cyg in 1978–2003. The dotted curves show the fit of the observations with a ninth-order polynomial. The solid lines show linear approximations to the descending and ascending branches (see text). The short-dashed line in the bottom panel is $J - H$ for an M6–M7 red giant.

descending branch and 1.37 ± 0.28 for the ascending branch, corresponding to $\alpha \sim 1.15$. According to Mathis [13], this value of α for $\lambda > 0.9$ μm is consistent with the dust grains being similar to interstellar grains.

Since the J brightness faded by $\sim 0.9^m$ from 1985 to 1996 (Fig. 4, the descending branch), the envelope's 1.25 μm optical depth near JD 2450090 was $\tau(J) \approx 0.83$. Comparing the time intervals occupied by the descending and ascending branches, we see that the increase in the dust envelope's optical depth occurred approximately a factor of 2.3 more slowly than the decrease.

Let us now consider the data at 2.2–5 μm. The situation here is more complicated than at 1.25–1.65 μm. If there is a relatively hot circumstellar dust envelope, its contribution to the combined light at these wavelengths will increase with the wavelength. For example, the contribution of the red giant's radiation to the total light of CH Cyg at 5 μm in 1982–1983 did not exceed 50%; the remaining light came from the dust envelope (cloud) [4]. The observed radiation from the dust envelope (the M and $L - M$ variations) show no clear relation to its absorption in the line of sight, though both components appeared in the fall of 1985 (Figs. 1, 2). The first maximum of the LM brightness was observed in the summers of 1986–1990, followed by a broad minimum centered on the summer of 1992. The next maximum was seen in 1995–1996; i.e., this second maximum of the LM brightness coincided with the highest column density of the envelope. Both variable dust components (the dust density in the line of sight and the radiation of the dust) had virtually completely disappeared by the spring of 2001, and the brightness of CH Cyg at 2.2–5 μm returned to its 1983–1984 level. The second maximum of the observed LM brightness can naturally be associated with the maximum radiation from the dust envelope, which began to condense in 1986, reached its highest density in 1996, and had dispersed by 2001–2002 (see above).

Thus, in our opinion, the most characteristic time intervals in the evolution of the system's IR radiation in 1978–2003 were the following.

(1) 1978–1983: The beginning of our IR observations coincided with the onset of the optical activity. Our IR observations during that period were obtained

Table 2. Linear approximation ($Y = A + B * X$) of the JH and $J - H$ variations on the descending and ascending branches of the light and color curves (Fig. 4)

Descending branch				
Parameter	J		H	
	value	error	value	error
A	-0.53	0.08	-1.15	0.07
B	2.09×10^{-4}	9.9×10^{-6}	1.51×10^{-4}	8.5×10^{-6}
R	0.90	0.14	0.87	0.12
Ascending branch				
Parameter	J		H	
	value	error	value	error
A	6.88	0.27	4.21	0.25
B	-5.23×10^{-4}	2.49×10^{-5}	-3.82×10^{-4}	2.28×10^{-5}
R	-0.91	0.16	-0.87	0.14
	Descending branch		Ascending branch	
Parameter	$J - H$		$J - H$	
	value	error	value	error
A	0.61	0.02	2.60	0.08
B	5.77×10^{-5}	2.9×10^{-6}	-1.34×10^{-4}	7.36×10^{-6}
R	0.89	0.04	-0.89	0.04

Note: R is the correlation coefficient.

Table 3. Mean magnitudes and parameters of the excess radiation from CH Cyg for three time intervals

Parameter	Mean	s.e.	N	Mean	s.e.	N	Mean	s.e.	N	Mag.
JD	2447030 (1988)	19	5	2450080 (1996)	45	8	2452850 (2003)	20	4	M6III
J	0.74	0.01	5	1.564	0.014	8	0.647	0.006	4	0.65
H	-0.28	0.01	5	0.353	0.014	8	-0.363	0.009	3	-0.32
K	-0.8	0.01	5	-0.347	0.014	8	-0.782	0.006	4	-0.69
L	-1.77	0.01	5	-1.533	0.016	8	-1.442	0.008	4	-0.95
M	-1.93	0.02	5	-1.74	0.017	8	-1.377	0.009	4	-0.71
$J - H$	1.02	0.01	5	1.211	0.007	8	1.01	0.006	3	0.97
$K - L$	0.97	0.02	5	1.185	0.015	8	0.66	0.007	4	0.26
$L - M$	0.16	0.03	5	0.207	0.017	8	-0.065	0.01	4	-0.24

using a PbS photoresistor, and a systematic bias relative to the main body of our observations (obtained after 1984, when we began IR photometry with an InSb light detector) is possible for all these data.

(2) 1986–1990: The "activation" of the cool sources.

(3) 1995–1997: The minimum of the JH brightness (the highest density of the dust envelope in the line of sight).

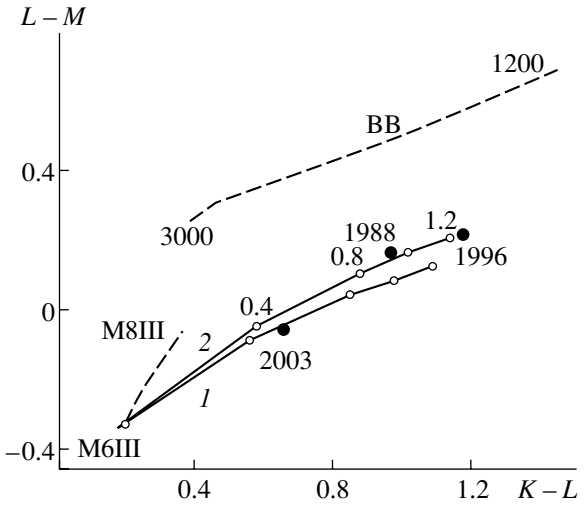

Fig. 5. Two-color $K-L$ and $L-M$ diagram for the three intervals from Table 3. The filled circles are the observed mean values. The dashed "BB" curve shows the change in the blackbody color indices for a change of the color temperature within 1200–3000 K. The dashed M6III–M8III curve is the change in the color indices for M6–M8 red giants. The solid curves *1* and *2* correspond to changes in the color indices for various models (see text).

(4) 2003: The system's IR radiation returned to its pre-1985 level.

The results of our photometric observations of CH Cyg averaged near intervals 2–4 are presented in Table 3, which presents the mean observational epochs, photometric bands, and color indices; the mean values, standard errors (s.e.), and number of averaged data points (N) for each of the intervals; and the magnitudes and color indices for a normal M6 giant (corrected for interstellar absorption with $E(B-V)=0.08^m$).

Table 3 indicates that excess radiation (relative to that of a normal M6 giant) was observed at $\lambda \geq 2.2$ μm during all three intervals. In 2003, when the local dust envelope had dispersed in our scenario, the lowest IR color excesses and the lowest LM brightness were observed. The highest reddening was observed in the IR in 1996, and the highest brightnesses at 3.5 and 5 μm in 1988.

For use in interpreting the data from Table 3, we calculated the changes in the color indices for a system consisting of a spherically symmetric dust envelope and a source of heating at its center, with the envelope and central source in radiative equilibrium [5]. The envelope was assumed to be physically thin. The source of heating is a cool M6 giant whose spectral energy distribution corresponds to that of a blackbody with a temperature of 2800 K; we varied the temperature of the dust grains in the envelope from 600 to 1000 K. The wavelength dependence of the dust envelope's optical depth was taken to be $\tau(\lambda)=\tau(1.25\ \mu\text{m})\ (1.25/\lambda)^{\alpha}$, where $\alpha=1.15$ (see above). The input parameters for the computations were the red giant's temperature, the temperature of the dust grains, the range of variations of the dust envelope's optical depth at $\lambda=1.25$ μm, and α. Figure 5 presents $(K-L, L-M)$ two-color diagrams; the filled circles are the mean $K-L$ and $L-M$ color indices for the three intervals from Table 3. The dashed curve "BB" shows variations of the color indices for a blackbody when the color temperature varies in the range 1200–3000 K. The dashed curve (M6III–M8III) shows the changes in the color indices for M6–M8 red giants. The solid curves *1* and *2* (the model curves) show the changes in $K-L$ and $L-M$ corresponding to a change in the dust envelope's optical depth at $\lambda=1.25$ μm from 0 to 1.2, with the dust grain temperature being 800 K (curve *1*) or 750 K (curve *2*). The numbers 0.4–1.2 near curve *2* correspond to the optical depth of the dust envelope at $\lambda=1.25$ μm, derived from the radiation at 2.2–5 μm. Thus, the dust envelope's optical depth in 1996, derived from the radiation of the dust envelope, exceeds 1.2 when the dust-grain temperature is $\sim$750 K. The attenuation of the brightness at 1.25–1.65 μm implies an optical depth for the dust envelope of $\sim$0.8 (see above). The difference between these values, $\sim$0.4, is equal to the optical depth of the dust envelope in 2003 (and before 1985). There was no absorption in the line of sight during these periods (only the light of the unreddened red giant was observed at 1.25–1.65 μm). In other words, before 1985 and after 2001, the dust envelope was manifest only in emission, and its dust-grain temperature was approximately the same as in the local dust envelope.

Thus, we can imagine the dust envelope of CH Cyg as follows. There is a stationary dust envelope in the form of an extended cloud (clouds) whose optical depth at $\lambda=1.25$ μm is $\sim$0.4 and whose dust-grain temperature is $\sim$750–800 K. For some reason, matter was injected into these clouds at the end of 1985, leading to the condensation of dust grains. The optical depth began to increase and, approximately by 1991, the dust envelope had been transformed from a cloud (clouds) to a nearly spherically symmetric local envelope with a dust-grain temperature of 750–800 K. The optical depth of this local envelope was highest in 1996, after which it began to disperse, again becoming a cloud (clouds) by 2000–2001.

Comparing the state of the system's hot source (the variations of $U-B$ in Fig. 1) to the emission of the dust component, we note the following. The formation of the spherically symmetric local dust envelope began during the decline of the strong optical outburst of 1978–1985. The first maximum in the

Table 4. Dust-envelope parameters for CH Cyg

Time interval		1988	1996	2003
$F_{ex}(\lambda)$, W cm$^{-2}\mu$m^{-1}	L	2.2×10^{-14}	1.8×10^{-14}	1.1×10^{-14}
	M	8.6×10^{-15}	7.3×10^{-15}	3.5×10^{-15}
T(M6III), K		2800	2800	2800
R(M6III), 10^{13} cm		2.2	2.2	2.2
T_d, K		750	750	750
R_d, 10^{14} cm		3.3	3.3	3.3
$\tau_{em}(1.25)$		$\sim$1	$\sim$1.2	0.4
$\tau_{ex}(1.25)$		$\sim$0.3	$\sim$0.8	$\sim$0
M_d, $10^{-6}M_\odot$		2.7	3.3	1.1
Time interval		1985–1988	1985–1996	1996–2001
$\dot{M}_d$, $10^{-7}M_\odot$ yr^{-1}		3.8	1.7	−5.4

emission of the dust component (the "activation" of the cool sources—injection of matter into the dust cloud) was observed during a deep minimum of the optical activity (1988). During the formation of the spherically symmetric dust envelope, the activity of the hot component was comparable to that of 1980–1984. After 1996, the hot component's activity declined, on average, and the spherically symmetric dust envelope dispersed, until only the stationary dust cloud remained by 2001, when the optical activity had also ceased.

Table 4 presents our estimates of the excess *LM* fluxes for the three intervals from Table 3. The fluxes were derived relative to the radiation of a normal M6 giant, taking into account the absorption in the local dust envelope. We also present the mean optical depths of the dust envelope estimated from the *LM* brightness ($\tau_{em}(1.25)$) and the attenuation of the *JH* radiation ($\tau_{ex}(1.25)$).

The temperature of the dust grains in the envelope estimated from the mean *KLM* brightnesses of CH Cyg in 1988, 1996, and 2003 was $\sim$750 K, and the envelope's optical depth at $\lambda = 1.25$ μm was 0.4 in 2003 and higher than 0.8 in 1988 and 1996.

Let us refine the estimated parameters of the dust envelope. Its radius is

$$R_d \approx 0.5 R_x (T_x T_d^{-1})^{2.07},$$

where $R_x = 2.2 \times 10^{13}$ cm [4] and T_x are the giant's radius and temperature and R_d and T_d are the same parameters for the dust envelope. The mass of the emitting dust envelope is

$$M_d \approx 4\pi R_d^2 (\rho V)(n\Delta R),$$

where $\rho \sim 3$ g cm^{-3} is the density of matter in the dust envelope, $V = 4\pi a^3/3$ is the volume of a dust grain, $(n\Delta R)_{em} \approx \tau_{em}(L)/Q(L)\pi a^2$ is the number of emitting grains in a column with a cross sectional area of 1 cm^2, $a \sim 0.1$ μm is the grain radius, and $Q(L) \sim 0.03$ is the absorption efficiency of the dust grains.

The estimated values of these parameters are collected in Table 4. The bottom row of this table gives the mean rates of matter injection and dispersion for the dust envelope for the three intervals in Table 3.

3.4. The Periodic Component in the JHK Variations

We have repeatedly searched for various periods in the observed IR-brightness variations of CH Cyg [4]. Two of the system's periods, $\sim$5300 days (the longer orbital period) and 756 days (the orbital period of the symbiotic pair), are not clearly manifest in the IR. Our observations have always indicated a period of $\sim$2000 days, even for short series of observations [14]. Having in mind the above results, we can take into account the influence of the local dust envelope on the IR observations and search for periods associated with the *JHK* brightness of the unreddened cool giant. For this purpose, we transformed the observed magnitudes into fluxes [10] and then subtracted the slowly varying component approximated with a ninth-order

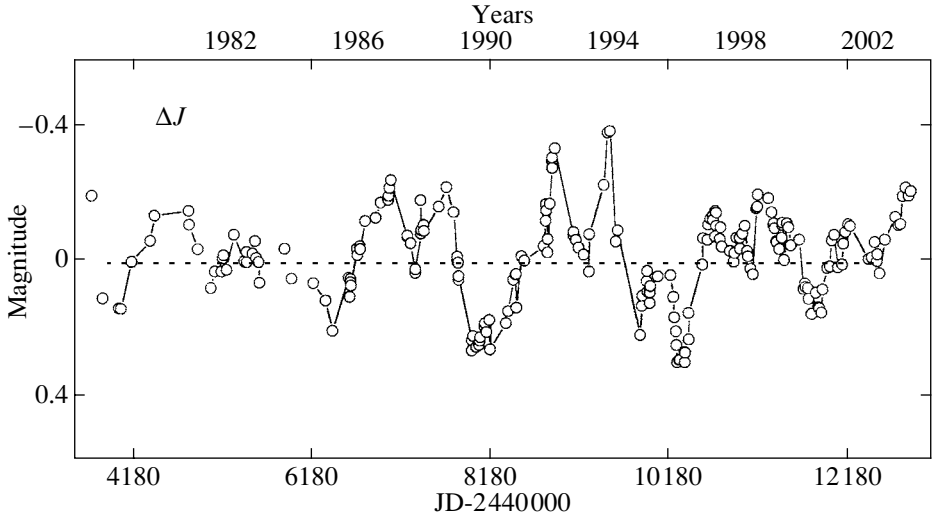

Fig. 6. J variations of CH Cyg after removal of the slow component approximated with a ninth-order polynomial. The separation between the vertical solid lines is 4000 days.

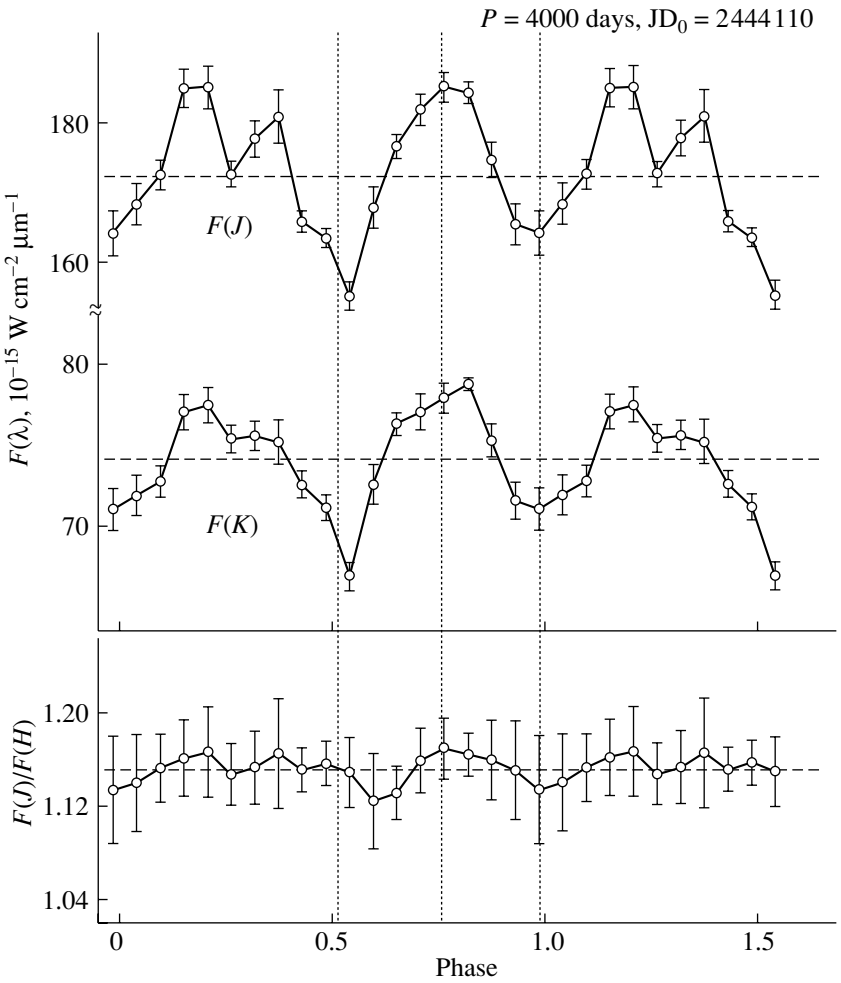

Fig. 7. Phase curves of the JK fluxes and the $F(J)/F(H)$ ratio folded with the 4000-day period, based on the entire set of observations of CH Cyg. The vertical short-dashed lines show the positions of minima in the phase curves. The horizontal dashed lines show the mean values.

Table 5. Possible parameters of the two red giants in the CH Cyg system

Parameter	First giant (M7)	Second giant (M6)
$F(K)$, 10^{-15} W cm^{-2}	68	10
$F_{\rm int}$, 10^{-15} W cm^{-2}	283	42
L, $L_\odot$	$\sim$7900	$\sim$1175
R, $R_\odot$	$\sim$366	$\sim$141

polynomial. A period of 4000 days (the solid vertical lines) is clearly visible in Fig. 6, which shows the residual variations of the J fluxes (1.25 μm). In approximately the middle of this period (the dotted vertical lines), an additional, shallower minimum is observed. A similar pattern is observed at 1.65 and 2.2 μm (the H and K filters). This led us to suppose that the 2000-day period could be the second harmonic of the 4000-day period.

Figure 7 shows the residual variations of the *JK* fluxes folded with the 4000-day period. Mean *JK* fluxes derived from the observations of CH Cyg in 2003 (the dashed horizontal lines) were added to the residual fluxes. The bottom panel of Fig. 7 presents the flux ratio $F(J)/F(H)$. The solid vertical bars in Fig. 7 are the standard errors. The amplitude of the J variations with the 4000-day period is $\sim 0.16^m$.

The shape of the phase curves with the 4000-day period immediately suggests binarity of the *JHK* light source. In addition, the 4000-day period is probably the orbital period for a binary system consisting of two cool stars. Eclipses are possible in the course of the orbital motion in the system: the minima are separated by phase intervals close to 0.5 (the two extreme vertical dotted lines), and a primary and secondary minima are present. Figure 3 [the ($J-H$, $V-J$) diagram] also provides indirect confirmation of the binary nature of the cool component of CH Cyg: it clearly shows variations of the cool component's spectral type in the range M5III–M7III. In addition, binarity of the cool component was noted in 1996 by Skopal *et al.* [2]. The variations of the $F(J)/F(H)$ flux ratio with phase are within the errors, and the value of this ratio is 1.15 ± 0.01, corresponding to $J-H = 0.98^m \pm 0.01^m$. In other words, the spectral types of the cool stars are in the range M5–M7.5, and their color temperatures can differ by about 100 K within the range of color temperatures 2800–2900 K. We can see in Fig. 7 ($F(J)$ and $F(K)$) that the primary minimum can be deeper than the secondary minimum. In this case, the component seen during the primary minimum should be somewhat cooler. The system's cool components may be two giants, with spectral types M(7–7.5) and M(5–6).

Some parameters of such a system can be estimated. Suppose that the second cool component is totally eclipsed in the primary minimum, and that the cool stars have the same spectral type. In this case, the flux from the first component, $F_1(\lambda)$, is equal to the flux at phase 0, and the flux from the second component is equal to the difference of the fluxes at phases 0.25 and 0; i.e., $F_2(\lambda) = F(\lambda, 0.25) - F_1(\lambda)$. The ratio of the components' radii is $R_2/R_1 \approx [F_2(\lambda)/F_1(\lambda)]^{0.5}$, and we find from the J, H, and K fluxes that $(R_2/R_1) \approx 0.4$. The minima in the phase curves (Fig. 7) have no plateaus, and, for the derived ratio of the radii, the orbital inclination cannot exceed 60°–70°. Knowing the K fluxes from the cool stars, we can estimate their integrated fluxes (luminosities). The $\lambda = 2.2$ μm flux for an M(5–7) giant is 0.24 ± 0.02 of the integrated flux [15]. Our parameter estimates for the cool stars are presented in Table 5. We estimated the radii and luminosities of the cool giants assuming they have the same temperature (2850 K), and adopting a distance to CH Cyg of 300 pc. These estimates are very rough, since our observations of CH Cyg cover about 9000 days, and so span the 4000-day period only slightly more than twice.

Thus, the 4000-day variability of the JHK brightnesses of CH Cyg agrees well with the presence of an eclipsing pair consisting of two cool giants whose effective temperatures differ by approximately 100 K, whose luminosity ratio is $L(\mathrm{M7})/L(\mathrm{M6}) \sim 6.8$, and whose radius ratio is $R(\mathrm{M7})/R(\mathrm{M6}) \sim 3.6$.

The orbital ephemeris can be written JD (Min I) = $2444180 + 4000E$.

Thus, we consider the main sources of the variability of CH Cyg observed in 1978–2003 in the range 1.25–2.2 μm to be the local dust envelope and the presence of two cool giants in the system, which constitute an eclipsing pair with the 4000-day orbital period.

Note that the JK (and H) light curves (Fig. 1) reveal variations on a time scale of 600–800 days, but our frequency analysis of the observations gives no period in this range. Figure 8 is similar to Fig. 7, but corresponds to the 756-day period. The variations

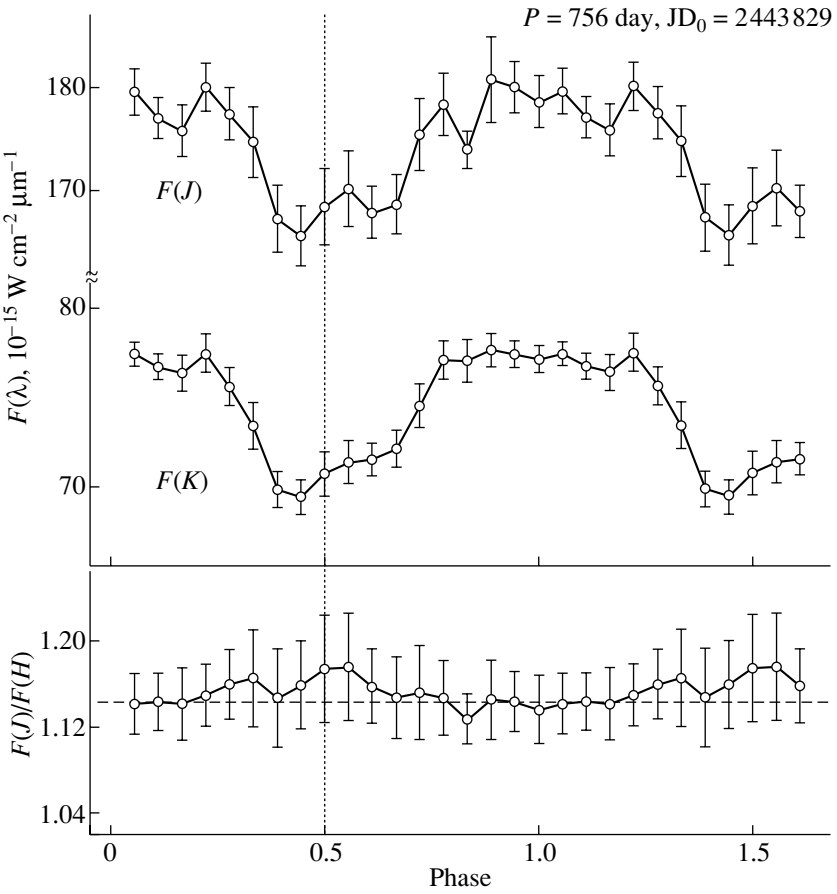

Fig. 8. Same as Fig. 7 for the 756-day period.

of the $J(H)K$ fluxes with this period are considerably larger than the standard errors, and may be real. The amplitude of the J variations with the 756-day period is $\sim 0.07^m$.

4. CONCLUSIONS

The above discussion leads us to the following conclusions.

(1) The local dust envelope that formed in the system in 1986 and reached its highest density in the line of sight in 1996 had largely dispersed by mid-2000, and the radiation from the system's cool giant had returned to its pre-1985 level. The observed variations of $J-H$ and $V-J$ can be successfully described using a model with a variable source (red star) and a dust component with variable optical depth in the line of sight. The optical density of the dust component could be as high as $E' \sim 1.5^m$. In 2001–2003, the giant's spectral type varied in the range M6.5–M7.5.

(2) We estimate $E(B-V) = 0.11^m \pm 0.01^m$, $0.16^m \pm 0.05^m$, and $0.11^m \pm 0.03^m$ based on the mean $J-H$, $V-J$, and $B-V$ color indices for four epochs of IR observations and six epochs of UBV observations in 2001.

(3) At least two components are present in the observed variations of JH and $J-H$: a slowly varying component with a time scale of about 6000 days and a faster component with a time scale of several hundred days. We conclude from the character of the JH and $J-H$ variations on the slow component's descending and ascending branches that the most probable origin of the observed variations is an increase and then decrease of the optical depth of the dust envelope that began to form in the system in 1986. The LM brightness and $L-M$ color variations support this picture. The parameter α in the relation $Q(\lambda) \propto \lambda^{-\alpha}$ was ~ 1.15 for the descending and ascending branches; this value of α at $\lambda > 0.9$ μm is consistent with the presence of dust grains similar to interstellar grains.

(4) The optical depth of the dust envelope at 1.25 μm near JD 2450090 was $\tau(J) \approx 0.83$. The increase of the dust envelope's optical depth was approximately a factor of 2.3 slower than its decrease.

(5) The dust envelope's optical depth in 1996, derived from the emission of the dust envelope at 3.5

and 5 μm, exceeded 1.2 if the temperature of its dust grains was $\sim$750 K. The attenuation of the brightness at 1.25–1.65 μm indicates that the optical depth of the dust envelope was $\sim$0.8. The difference between these values, $\sim$0.4, is just the optical depth of the dust envelope in 2003 (and prior to 1985). There was no absorption in the line of sight at these times (only the radiation of the unreddened red giant contributes at 1.25–1.65 μm).

(6) The dust envelope of CH Cyg can be pictured as a stationary dust cloud (or clouds) with an optical depth at $\lambda = 1.25$ μm of $\sim$0.4 and a grain temperature of $\sim$750–800 K. Matter was injected into this cloud in late 1985, giving rise to the condensation of dust grains. The optical depth began to increase and, by 1991, the dust envelope was transformed from a cloud to a nearly spherically symmetric local envelope with a grain temperature of 750–800 K. Its optical depth was highest in 1996, after which it began to disperse, becoming a cloud again by 2000–2002.

(7) After subtracting the slow component in the observed *JHK* variations for CH Cyg, we clearly detected a period of 4000 days in the residual variations of the *JHK* fluxes. The 2000-day period found from our earlier *JHK* photometric data may be the second harmonic of this 4000-day period. Analysis of the phase curves of the variations of the residual *JHK* fluxes with the 4000-day period suggests that this period corresponds to the orbital motion of two cool (M6–M7) giants. The binary system may exhibit eclipses. The ratio of the components' radii is $R(\mathrm{M7})/R(\mathrm{M6}) \sim 3.6$, the ratio of their luminosities is $L(\mathrm{M7})/L(\mathrm{M6}) \sim 6.8$, and the radius and luminosity of the cooler component are $R(M7) \sim 360R_\odot$ and $L(M7) \sim 7900L_\odot$. The orbital inclination cannot exceed 60°–70°. The orbital ephemeris can be written JD (Min I) = 2444180 + 4000E.

ACKNOWLEDGMENTS

This work was partially supported by the Federal Science and Technology Program in Astronomy.

REFERENCES

1. K. H. Hinkle, F. C. Fekel, D. S. Johnson, and W. W. G. Schrlach, Astron. J. **105**, 1074 (1993).
2. A. Skopal, M. F. Bode, H. M. Lloyd, and S. Tamura, Astron. Astrophys. **308**, L9 (1996).
3. S. Mikkola and R. Tanikawa, Astron. J. **116**, 444 (1998).
4. O. G. Taranova and V. I. Shenavrin, Astron. Zh. **77**, 780 (2000) [Astron. Rep. **44**, 460 (2000)].
5. O. G. Taranova, Pis'ma Astron. Zh. **17**, 253 (1991) [Sov. Astron. Lett. **17**, 107 (1991)].
6. O. G. Taranova and B. F. Yudin, Astron. Astrophys. **257**, 615 (1992).
7. A. Skopal, T. Pribulla, M. Wolf, *et al.*, Contrib. Astron. Observ. Skalnate Pleso. **30**, 29S (2000).
8. A. Skopal, M. Vanko, T. Pribulla, *et al.*, Contrib. Astron. Observ. Skalnate Pleso. **32**, 62 (2002).
9. J. Koorneef, Astron. Astrophys., Suppl. Ser. **51**, 489 (1983).
10. H. L. Johnson, Annu. Rev. Astron. Astrophys. **4**, 193 (1966).
11. G. Perrin, V. Coude du Foresto, *et al.*, Astron. Astrophys. **331**, 619 (1998).
12. S. J. Kenyon, Astron. J. **95**, 1817 (1988).
13. J. S. Mathis, Annu. Rev. Astron. Astrophys. **28**, 37 (1990).
14. O. G. Taranova, Astron. Tsirk., No. 1473, 7 (1986).
15. H. M. Dyck, G. W. Lockwood, and R. W. Capps, Astrophys. J. **189**, 89 (1974).

Translated by N. Samus'

Astronomy Reports, Vol. 48, No. 10, 2004, pp. 826–833. Translated from Astronomicheskiĭ Zhurnal, Vol. 81, No. 10, 2004, pp. 909–917.

Two-Stage Algorithm for Reconstructing the Images of the Gravitational Lens QSO 2237+0305

E. A. Koptelova[1], E. V. Shimanovskaya[2], B. P. Artamonov[1], M. V. Sazhin[1], and A. G. Yagola[2]

[1]*Sternberg Astronomical Institute, Moscow State University, Universitetskiĭ pr. 13, Moscow, 119899 Russia*

[2]*Moscow State University, Vorob'evy gory, Moscow, 119899 Russia*

Received February 17, 2004; in final form, March 15, 2004

Abstract—A two-stage algorithm for reconstructing images made up of point sources is proposed and applied to images of the gravitational lens QSO 2237+0305 obtained with the 1.5-m telescope of the Maĭdanak Observatory. In the first stage, a modified Tikhonov regularization algorithm is used to split an image with a high signal-to-noise ratio into two parts, corresponding to numerical galaxy and quasar components. In the second stage, the astrometric and photometric characteristics of the individual images of the gravitational-lens system are determined using information about the brightness distribution in the galaxy and a least-squares fit. The two-stage algorithm substantially reduces the time required for the image analysis. A comparison of our method with CLEAN is presented. © *2004 MAIK "Nauka/Interperiodica".*

1. INTRODUCTION

The best method to use for the reconstruction of images of astronomical objects depends substantially on the nature of these objects and the required accuracy of their photometric and astrometric characteristics. The available algorithms can be separated into two groups: CLEAN and its modifications [1] and methods based on searching for the extremal of a specified functional. Such methods can be separated into statistical (informational) methods [2] (e.g., the maximum-entropy [3–5] and maximum-likelihood [6] methods) and regularization algorithms, based on the theory of ill-posed inverse problems developed by Tikhonov and his coauthors [7–9]. The maximum-entropy method works well in the reconstruction of extended smooth images with sharp boundaries, but leads to considerable errors in the case of point sources with large intensity variations, especially when they are embedded in a smooth background. The method of Richardson and Lucy [10], which is based on the Bayes theorem, is commonly used for images with large signal-to-noise ratios. When it is necessary to reconstruct images with complex structures (e.g., overlapping sources), more sensitive methods must be applied. One efficient reconstruction method is the MCS method, which was proposed by the Belgian scientists Magain, Courbin, and Sohy [11] in 1997. This method is based on Tikhonov regularization theory [12], and makes it possible to considerably improve the resolution and obtain reliable photometric and astrometric results. The accuracy of this and other methods depends substantially on the appropriate choice of the point spread function, as well as on the model used to describe the galaxy (either numerical or analytical). Therefore, the results of the calculations are model-dependent.

A large volume of data on the Einstein Cross (the gravitational lens QSO 2237+0305) is now available, obtained by a number of international groups. The first international project involved observations using two telescopes over three years, with the intervals between observations being slightly less than a year [13]. More valuable results were obtained by the Ostensen *et al.* [14], whose observations were carried out over five years with the Nordic Optical Telescope. In the framework of the GLITP project [15], the Einstein Cross was observed by this same telescope daily in 1999–2000 in the V and R filters. Monitoring of the gravitational lens QSO 2237+0305 has been carried out since 1996 at the Maĭdanak Observatory. A large volume of $BVRI$ data has been obtained.

We propose a two-stage algorithm for reconstructing the images of quadrupole gravitational lenses as a means of deriving information about the astrometric and photometric characteristics of these objects. This algorithm is based on a regularization of the corresponding ill-posed inverse problem. Its applicability is tested using images of the gravitational lens QSO 2237+0305 (the Einstein Cross) obtained at the Maĭdanak Observatory in 2002. The results are compared with the results of processing the same data using the CLEAN algorithm, which does not use *a priori* information about the smoothness of

1063-7729/04/4810-0826$26.00

the solution and represents the image as a set of point sources, based on a fully parameterized model of the galaxy. Criteria for selecting an approximate solution of an inverse problem have been developed and verified for regularization algorithms [7]. The effectiveness of the CLEAN reconstruction is directly observed by the user: the image of the object is "cleaned" from the initial field until the correlation between the synthesized point-spread function and the component image obtained by the algorithm is maximum. As was shown by Ostensen *et al.* [14], correlation coefficients below 0.98 for any of the components indicate considerable errors in the magnitudes (brightnesses) of the components. An important feature of this method and its modifications is that each component is considered independently, so that the results are not affected by neighboring components, in contrast to regularization methods.

Note that the errors of the methods used to process the images should be taken into account when light curves for the components of the Einstein Cross obtained by various groups in the course of long-term observations are combined.

2. OBSERVATIONS AND PRELIMINARY DATA REDUCTION

Images of the quasar QSO 2237+0305 were obtained using the 1.5-m telescope of the Maĭdanak Observatory during the fall of 2002 (about 20 nights). On average, observations of the object were obtained five times per night.

A 2000×800 CCD array cooled with liquid nitrogen designed by the Copenhagen University Observatory was used for the observations. The array has pixel size $\Delta = 15$ μm, gain factor $g = 1.2e^{-}\mathrm{ADU}^{-1}$, and readout noise $\mathrm{RON} = 5\mathrm{ADU}$. All the images were obtained in the R filter with an exposure time of 180 s at the 1/16 focus, which corresponds to a scale $0.12''$ per pixel. The mean seeing corresponds to a point source having a full width at half maximum of about $0.8''$.

The preliminary data reduction included bias subtraction, division by the mean value of a flat field, sky subtraction, and removal of bad pixels and cosmic-ray traces. An image with size 64×64 pixels ($7.68'' \times 7.68''$) cut from the initial image and centered on the nucleus of the galaxy 2237+0305 galaxy was reconstructed. The signal-to-noise ratio varied from 100 to 150.

3. ALGORITHM FOR THE IMAGE RECONSTRUCTION

3.1. Mathematical Formulation of the Problem

The model image obtained by a ground-based telescope and distorted by the limited resolution of the equipment used and by atmospheric turbulence is often described by the convolution equation

$$A[z] \equiv t * z \tag{1}$$
$$= \int\int t(x-\zeta, y-\eta) z(\zeta,\eta) d\zeta d\eta = u(x,y),$$

where A is the convolution operator, $z(x,y)$ is the desired brightness distribution over the object, $t(x,y)$ is the point spread function (PSF), and $u(x,y)$ is the observed brightness distribution. Let us assume that the operator A acts from a normalized space Z to the space of square-integrable functions, and that a solution exists.

When processing real frames, it is always necessary to deal with data that were recorded on the pixel grid with some error that was naturally introduced in the plane of the CCD array, and the numerical realization of an image-reconstruction method usually involves some approximation and digitization of the data. Photon noise and the resulting errors in the input data substantially complicate the solution of (1), which otherwise could be solved simply via a transformation of the space of the Fourier images and application of the convolution theorem. Therefore, the reconstruction of an image is reduced to searching for an approximate solution of (1) using an approximate operator A_h with a known estimated error h ($||A_h - A||_{Z \to L_2} \le h$) and a specified approximate right-hand side u_δ with an estimated noise level δ ($||u_\delta - u||_{L_2} \le \delta$).

If the error in the brightness in pixel (i,j) is σ_{ij}, then the error in the right-hand side should be

$$\delta = \sqrt{\sum_{i,j} \sigma_{ij}^2}. \tag{2}$$

Assuming that the error in the intensity in each pixel is composed of a noise component represented by a Poisson law and a readout error, we can write

$$\sigma_{ij} = \sqrt{\frac{u_{ij}}{g} + N\mathrm{RON}^2}. \tag{3}$$

This expression corresponds to the frame obtained by summing N frames to increase the signal-to-noise ratio. Here, u_{ij} is the count rate in pixel (i,j), g is the gain of the CCD array, and RON is the readout noise.

The error in the operator will depend on the method used to model the PSF. If the error in the PSF model

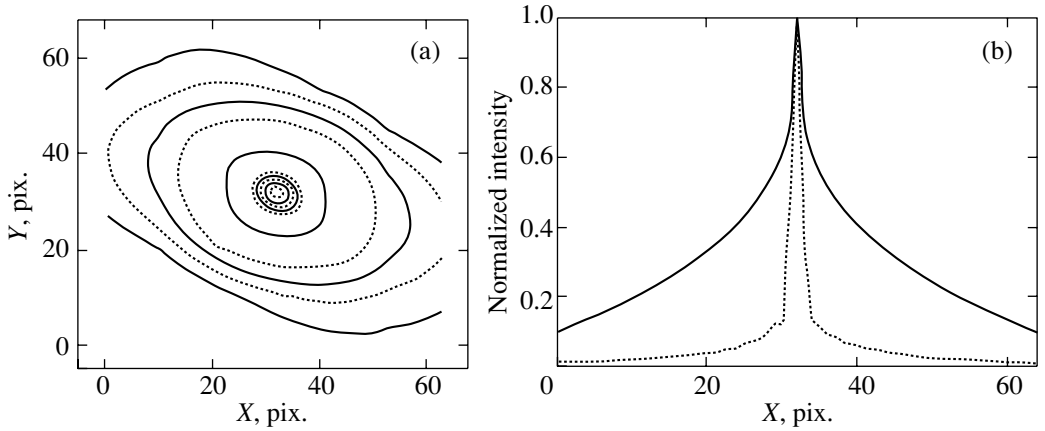

Fig. 1. Central part of the galaxy 2237+0305: (a) brightness contours, (b) profile of the galaxy along the major axis (the solid curve corresponds to the Sersic model, and dotted curve represents the brightness distribution obtained numerically).

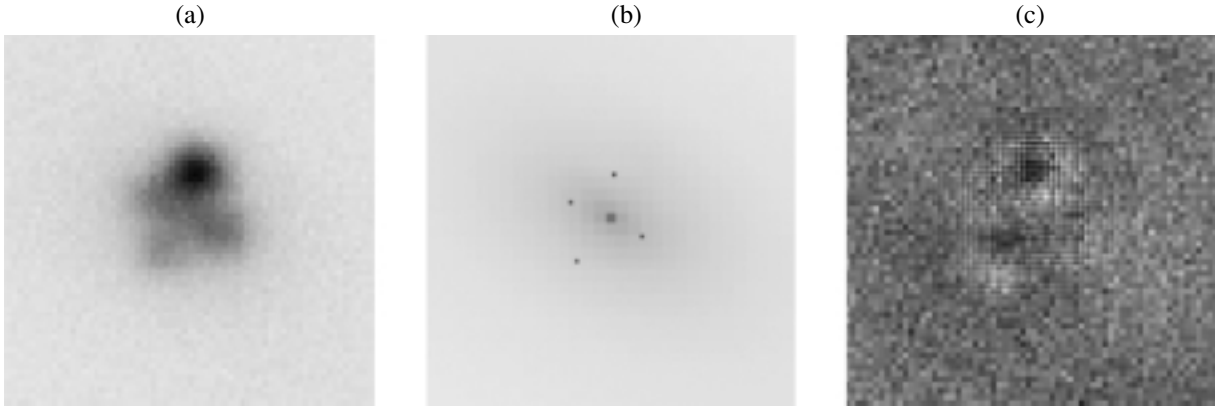

Fig. 2. Results of the reconstruction: (a) initial image, (b) reconstructed image, and (c) error distribution (model − observational data)/$\sqrt{\text{model}}$.

in each pixel (the kernel of the convolution equation) is $d\%$, then the error in the operator will be

$$h = \sqrt{\sum_{i,j}(dt_{ij})^2}. \qquad (4)$$

3.2. Modeling the PSF

The kernel $t(x, y)$, which is determined by the joint influence of the equipment used and the atmosphere on a signal with the form of a δ function, is constructed from observations of one or several nearby stars in the same frame. These stars should be located sufficiently close to the region under investigation that variations of the PSF over the frame can be ignored, but sufficiently far from the reconstructed object that the images of the star and object do not overlap. In our case, the PSF was determined from observations of the α star from the same frame. We used two methods to reconstruct the PSF: (1) smoothing the star's brightness distribution using median filtration and then normalizing the peak to a flux of unity, or (2) approximating the star with an analytic profile based on a two-dimensional elliptical Gaussian.

We estimate the total loss in intensity to be $\varepsilon = (1 - k) \times 100\%$, where k is the ratio of the integrated intensities of the model and the star. The loss was slightly lower in the case of median filtration with a window equal to the half-width of the PSF than for the two-dimensional Gaussian approximation, which was $\sim$3–4%.

3.3. The Regularization Method

The convolution equation (1) with an approximate, specified right-hand side represents an ill-posed problem. Its solution may be nonunique, and small

perturbations in the input information can lead to very large changes in the solution. Tikhonov [7] proposed his regularization method to deal with such problems. The approximate solution obtained using this method takes into account *a priori* information about the image to be reconstructed, and identifies among the set of all possible solutions a unique solution that possesses a specified degree of smoothness, has physical meaning, and whose norm in the chosen functional space tends to the norm of the exact solution when the errors in the input data tend to zero.

The basic idea of this method is to reformulate the problem (1) by constructing a smoothing functional composed of two parts: the square of the residual, and the "stabilizer" $\Omega[z]$ multiplied by the regularization parameter α:

$$M^{\alpha}[z] \equiv ||A_h z - u_\delta||^2_{L^2} + \alpha\Omega[z]. \qquad (5)$$

The choice of the stabilizer depends on the smoothness of the required solution. In most cases, this function is taken to be the square of the norm of the solution in the functional space under consideration, but this is not the only possibility. The initial problem (1) is replaced by the problem of minimizing the smoothing functional for a specified chosen regularization parameter, and the resulting extremal z^{α} can be treated as an approximate solution [7–9].

One key problem in the correct reconstruction of images is choosing a regularization parameter α that will result in a uniform error distribution and the required smoothness for the solution. In other words, α is responsible for the balance between the degree of correspondence of the required solution to the right-hand side of (1) (within the errors in the input data) and the smoothness of the solution. Thus, the method used to specify the regularization parameter α is crucial in the solution of ill-posed problems. In general, the regularization parameter will depend on the input information, the errors, and the method used to approximate the initial problem. The most common method is to find a residual or a generalized residual (when the error in the specified operator A can be estimated). In this case, the parameter α is taken to be the solution of the equation

$$\rho(\alpha) = 0, \qquad (6)$$

where $\rho(\alpha)$ is the generalized residual, defined to be

$$\rho(\alpha) \equiv ||A_h[z^{\alpha}] - u_\delta||^2_{L^2} - (\delta + h||z^{\alpha}||_Z)^2\,. \qquad (7)$$

This is an *a posteriori* method for choosing the regularization parameter, since the smoothing functional must be minimized in each iteration for α to find the root of (6). To solve (6), we can first take some initial value for α that satisfies the inequality $\rho(\alpha) > 0$, then carry out the following steps.

(1) Calculate the next value $\alpha = \alpha/2$.

Table 1. Parameters of the galaxy 2237+0305

Images	r_e	$(a-b)/a$	PA
H (CASTLES)	$4.7'' \pm 0.9''$	0.33 ± 0.01	$66^\circ \pm 1^\circ$
R (GLITP)	4.94 ± 0.25	0.38 ± 0.02	62 ± 1
R (Maĭdanak)	4.6 ± 0.3	0.35 ± 0.02	64 ± 1

(2) Minimize the smoothing functional using the new α.

(3) If equality (6) is satisfied, the appropriate approximate solution has been obtained. It $\rho(\alpha) > 0$, the process must be repeated. If $\rho(\alpha) < 0$, then we must search for the root of (6), for example, using the segment-halving method.

3.4. A priori Information

To obtain stable and physically relevant results, the image-processing algorithm should incorporate as much *a priori* information about the reconstructed object as possible. This is, in fact, a general rule for solving ill-posed problems. The more a priori information about the required solution is formalized and incorporated into the algorithm, the more adequate the physical results that are ultimately obtained. Accordingly, the model image of the gravitational-lens system was represented by a sum of the images of the quasar components (a sum of δ functions)

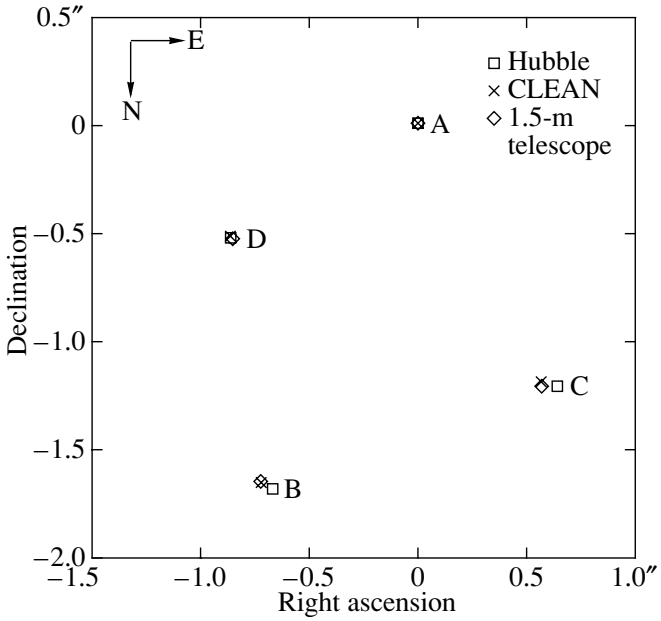

Fig. 3. Astrometry of QSO 2237+0305.

Table 2. Astrometry of QSO 2237+0305 according to the data of Rix *et al.* [25]

Component	$\Delta\alpha$	$\Delta\delta$
B	$-0.673'' \pm 0.003''$	$-1.697'' \pm 0.003''$
C	0.635 ± 0.003	-1.210 ± 0.003
D	-0.866 ± 0.003	-0.528 ± 0.003

Table 3. Astrometry of QSO 2237+0305 according to the observations with the Maĭdanak Observatory 1.5-m telescope

Component	$\Delta\alpha$	$\Delta\delta$
B	$-0.723'' \pm 0.052''$	$-1.646'' \pm 0.058''$
C	0.567 ± 0.069	-1.211 ± 0.016
D	-0.858 ± 0.016	-0.534 ± 0.016

and the brightness distribution of the lensing galaxy (a smooth function):

$$z(x,y) = g(x,y) + \sum_{q=1}^{Q} a_q \delta(x - b_q, y - c_q), \quad (8)$$

where Q is the number of point sources, which have coordinates (b_q, c_q) and intensities a_q, $g(x,y)$ is the component of the solution corresponding to the galaxy, and δ is a Dirac delta function. The assumption that the required solution (in our case, the function describing the brightness distribution in the galaxy) is smooth is incorporated into the algorithm via an appropriate choice of the stabilizer [16]. As was noted above, the stabilizer is often defined to be the square of the norm in the chosen functional class Z, which is responsible for the degree of convergence of the approximate solution to the exact solution. For $Z = L_2$ (the set of square-integrable functions) and $Z = W_{21}$ (the set of functions possessing square-integrable first-order generalized derivatives), a mean-convergence theorem has been proven in the general theory of ill-posed problems. For $Z = W_{22}$ (functions possessing square-integrable generalized derivatives up to second order), there is higher-order convergence as well, which is uniform in each compact, bounded subset of the plane. For the space of functions with bounded total variations (these functions may be discontinuous at grid lines), Leonov proved the piecewise uniform convergence theorem [17–20]. The dependence of the properties of the solution on the choice of stabilizer for the functional classes L_2, W_{21}, W_{22}, and for functions with bounded total variations were analyzed in [16].

The galaxy 2237+0305 has a bright nucleus. This sharp variation in brightness can be described in various ways, for example, by including an additional δ function describing the central part of the galaxy in the model (as was done in the MCS method), or by using a functional space that admits jumplike behavior of the solution, such as the space of functions with finite total derivatives. Numerical simulations have shown that the most stable results are obtained when we introduced the assumption that the brightness distribution in the galaxy was close to one of the model profiles into the algorithm; in other words, when the stabilizer was taken in the form

$$\Omega[z] = ||g - g^{mdl}||_G^2 + \beta \sum_{q=1}^{Q} a_q^2. \quad (9)$$

The second term in this expression suppresses the quasar components, which are extremely bright compared to the galaxy. The parameter β was chosen so that the difference between the intensity of the components and the much weaker background was taken into account. This approach enables us to exclude probable artefacts in the brightness distribution of the galaxy ("holes" at the positions of the quasar components). A generalized de Vaucouleurs exponential law [21–23] describes the central region of galaxy very well:

$$g^{mdl}(r) = I_e \exp^{-b_n(\frac{r}{r_e})^{\frac{1}{n}}}, \quad (10)$$

where r_e is the effective radius, I_e is the intensity of the galaxy inside the effective radius, and b_n is some function of n [21]. The coordinate r is expressed in Cartesian coordinates introduced in the plane of the frame:

$$r = \sqrt{\frac{x'^2}{a_x^2} + \frac{y'^2}{a_y^2}}, \quad (11)$$
$$x' = (x - x_c)\cos T - (y - y_c)\sin T,$$
$$y' = (x - x_c)\sin T + (y - y_c)\cos T.$$

The model parameters are determined at the preliminary stage using the least-squares method.

4. DESCRIPTION OF THE ALGORITHM

In the case of the gravitational lens QSO 2237+0305, the galaxy has an extremely bright nucleus and is almost indistinguishable from the background in the wings, making the processing of each individual frame difficult. To optimize the reduction of the frames, the process was separated into two stages: (1) obtaining a numerical model for the galaxy using the summed frame and the regularization algorithm and (2) utilizing this model

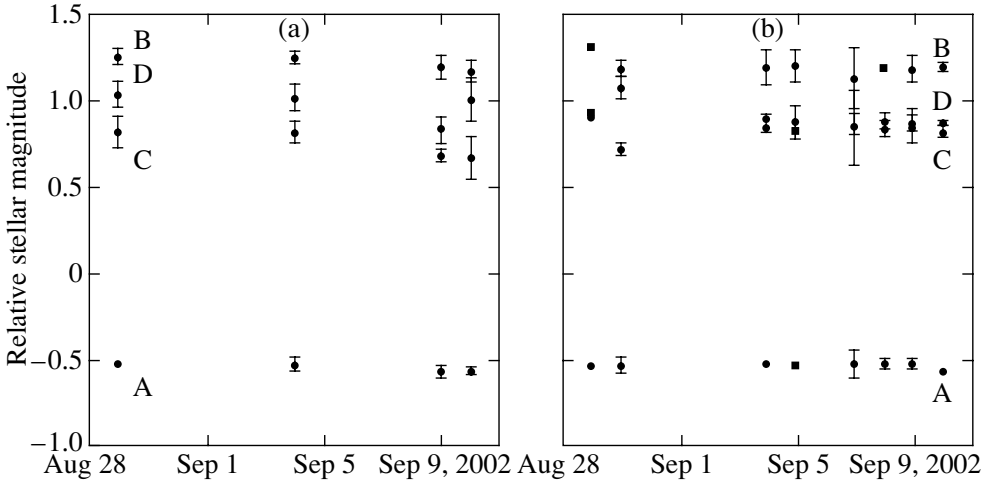

Fig. 4. Photometry of QSO 2237+0305: (a) CLEAN method and (b) the two-stage reconstruction algorithm.

to reduce a large volume of observational material to obtain the astrometric and photometric parameters of the gravitational lens.

The first stage. The frames with the best quality were summed. The finite-parameter inverse reconstruction problem was solved for the summed frame, assuming that the image could be separated in accordance with (8) and that the lensing galaxy is described by the model (10). We obtained the model parameters by minimizing the functional χ^2 on the grid

$$F_1(a_q, b_q, c_q, I_e, n, r_e, x_c, y_c, a_x, a_y, T) \qquad (12)$$
$$= \sum_{i=0}^{N_1-1}\sum_{j=0}^{N_2-1}\frac{1}{\sigma_{ij}^2}\left(\sum_{m=0}^{N_1-1}\sum_{n=0}^{N_2-1}\left\{t_{i-m,j-n}\right.\right.$$
$$\left.\left.\times\left(\sum_{q=1}^{4}a_q\delta_{m-b_q,n-c_q}+g_{mn}^{mdl}\right)\right\}-u_{ij}\right)^2.$$

Here and below, we use the notation for the grid functions $f_{ij} = f(x_i, y_j)$; the grid width is equal to one pixel, and the trapezoid method was used to calculate the integrals. The minimization sequence was constructed using the method of Powell [24].

Next, the image of the Einstein Cross was reconstructed from the summed frame using the regularization algorithm, assuming that the required solution was described by the model (8). We applied the assumption that the brightness distribution of the galaxy was close to the model distribution (10) through the stabilizer, which had the form (9). The coordinates of the quasar components (b_q, c_q) obtained in the previous step were fixed. The resulting model brightness distribution for the galaxy was used to calculate the stabilizer and as an initial approximation in the minimization of the smoothing functional:

$$M^\alpha(a_q, g) \qquad (13)$$
$$= \sum_{i=0}^{N_1-1}\sum_{j=0}^{N_2-1}\frac{1}{\sigma_{ij}^2}\left(\sum_{m=0}^{N_1-1}\sum_{n=0}^{N_2-1}\left\{t_{i-m,j-n}\right.\right.$$
$$\left.\left.\times\left(\sum_{q=1}^{4}a_q\delta_{m-b_q,n-c_q}+g_{mn}\right)\right\}-u_{ij}\right)^2+\alpha\Omega[g].$$

The conjugate-gradient method was used to construct the minimizing sequence [24].

The main result of this stage in the reduction, along with the relative astrometric and photometric parameters of the components of the Einstein Cross, is a numerical brightness distribution for the galaxy, which can be further used when processing the individual frames. Brightness contours for the central region of the lensing galaxy are presented in Fig. 1a. Profiles of a generalized de Vaucouleurs model (Sersic model) and the brightness distribution obtained using the regularization algorithm are presented in Fig. 1b. The intensities are normalized to unity at the maximum.

The mean values of the galaxy parameters obtained by the CASTLES group in the H filter, by the GLITP group, and in the first step of our two-stage reconstruction algorithm for data in the R filter are presented in Table 1.

The second stage. The numerical model for the galaxy obtained by reconstructing the summed frame was used to process the entire series of observations of the object. The brightness distribution of the galaxy was described using the relation

$$G(x, y) = \lambda_1 g^{num}(x, y) + \lambda_2, \qquad (14)$$

Table 4. Photometry of QSO 2237+0305 using the two-stage reconstruction algorithm

Date	Seeing	A	B	C	D
09.28.2002	0.8″	-0.524 ± 0.010	1.309 ± 0.020	0.913 ± 0.010	0.930 ± 0.018
09.29.2002	0.9	-0.527 ± 0.042	1.181 ± 0.044	0.721 ± 0.037	1.075 ± 0.063
10.04.2002	0.8	-0.521 ± 0.005	1.193 ± 0.101	0.835 ± 0.027	0.887 ± 0.031
10.05.2002	0.7	-0.526 ± 0.018	1.199 ± 0.092	0.828 ± 0.015	0.878 ± 0.098
10.07.2002	0.8	-0.521 ± 0.076	1.130 ± 0.177	0.843 ± 0.217	0.868 ± 0.055
10.08.2002	0.9	-0.519 ± 0.025	1.190 ± 0.021	0.836 ± 0.049	0.883 ± 0.051
10.09.2002	0.8	-0.522 ± 0.035	1.184 ± 0.076	0.857 ± 0.096	0.877 ± 0.038
10.10.2002	0.8	-0.567 ± 0.007	1.194 ± 0.020	0.821 ± 0.034	0.873 ± 0.020

Table 5. Photometry of QSO 2237+0305 using the CLEAN method

Date	Seeing	A	B	C	D
09.28.2002	0.8″	-0.516 ± 0.006	1.255 ± 0.047	0.817 ± 0.094	1.038 ± 0.074
10.04.2002	0.8	-0.520 ± 0.040	1.245 ± 0.037	0.822 ± 0.064	1.012 ± 0.078
10.09.2002	0.8	-0.561 ± 0.035	1.192 ± 0.076	0.682 ± 0.038	0.832 ± 0.075
10.10.2002	0.8	-0.562 ± 0.023	1.168 ± 0.057	0.672 ± 0.122	1.003 ± 0.121

where λ_1 specifies the intensity of the galaxy in each frame, and λ_2 is a constant background intensity. Since the galaxy is described here using only two independent parameters, the number of variables is reduced considerably. At this stage, we again solved the finite-parameter inverse problem using the least-squares method. The model parameters were obtained by minimizing the χ^2 functional

$$F_2(a_q, b_q, c_q, \lambda_1, \lambda_2) \tag{15}$$
$$= \sum_{i=0}^{N_1-1}\sum_{j=0}^{N_2-1}\frac{1}{\sigma_{ij}^2}\left(\sum_{m=0}^{N_1-1}\sum_{n=0}^{N_2-1}\left\{t_{i-m,j-n}\right.\right.$$
$$\left.\left.\times\left(\sum_{q=1}^{4}a_q\delta_{m-b_q,n-c_q}+\lambda_1 g_{mn}^{num}+\lambda_2\right)\right\}-u_{ij}\right)^2.$$

5. DISCUSSION OF THE RESULTS

The results of reconstructing the Maĭdanak Observatory Einstein-Cross images are presented in Fig. 2. The size of the cutoff part of the frame is 32×32 pixels. The scale of the image was doubled by subdividing the pixel grid and interpolating the brightness distribution to intermediate points. The functional space used to search for the brightness distribution of the galaxy was $G = L_2$.

QSO 2237+0305 has a complex spatial structure, with the angular distance between components being about 1″, which is comparable to the half-width of the point spread function. Therefore, the wings of the brightness distributions of the quasar components overlap, even in very good observing conditions. In addition, large problems with the photometry were caused by the lensing galaxy, which possesses a very bright nucleus.

The proposed algorithm demonstrated its stability in the determination of the astrometric characteristics of the Einstein-Cross components. The results of astrometry of the object relative to component A according to the Maĭdanak observations are presented in Fig. 3. The positions of the quasar components obtained using the two-stage reconstruction algorithm are marked by diamonds, while the crosses denote the results obtained using the CLEAN algorithm, and the squares represent data obtained by the Hubble Space Telescope [25] (the coordinates of [25] are presented in Table 2). The coordinates of the components obtained for the 2002 Maĭdanak Observatory data using CLEAN and the two-stage reconstruction algorithm are presented in Table 3.

The small angular separation between the components, comparable to the half-width of the PSF, and

their proximity to the nucleus of the lensing galaxy complicate determination of the photometric characteristics of QSO 2237+0305. Photometry of the Einstein Cross carried out using the CLEAN method and our two-stage reconstruction algorithm is presented in Fig. 4, and the corresponding numerical values are given in Table 4. We defined the photometric error to be the rms deviation of the results for individual frames taken during a single night. The photometric calibration was carried out using the α star in the field, which was present in all frames. The flux of this star was used to estimate the fluxes from the compact sources. The photometric data for frames with the best quality obtained using the CLEAN method and our algorithm are presented in Table 5. The difference in the resulting magnitudes may be associated with the models used for the galaxy profile, since this affects the reference point for the fluxes but not the general behavior of the curves.

The results of the reconstruction using the widespread CLEAN method and our two-stage algorithm show that CLEAN is not effective when the seeing is worse than $0.8''$, while the two-stage reconstruction algorithm can process even the low quality frames.

6. CONCLUSIONS

The results of reconstructing the images of the Einstein Cross gravitational-lens system presented in Fig. 2 demonstrate clearly that our two-stage algorithm (which is a combination of a modified regularization algorithm and the least-squares method) can be successfully applied to the reduction of complex images, such as close quadrupole gravitational lenses. The method makes it possible to separate the image into two components: a set of point sources (quasar components) and an extended object (the galaxy). The successful reconstruction of complex images containing both smooth and singular (point-source) parts requires using all available *a priori* information about the object. The more *a priori* information that is formalized and incorporated into the algorithm, the more reliable and adequate are the results of reconstructing the images. Parametrizing the brightness distribution of the galaxy based on a numerical model constructed in the first stage enables us to substantially reduce the time required to process each individual frame, and therefore to simplify the treatment of large volumes of observational material.

ACKNOWLEDGMENTS

This work was supported by the Russian Foundation for Basic Research (project nos. 01-02-16800 and 02-01-00044).

REFERENCES

1. J. A. Hogbom, Astron. Astrophys., Suppl. Ser. **15**, 417 (1974).
2. V. Yu. Terebizh, Usp. Fiz. Nauk **165** (2), 143 (1995).
3. R. Narayan and R. Nityananda, Annu. Rev. Astron. Astrophys. **24**, 127 (1986).
4. J. Skilling and R. K. Bryan, Mon. Not. R. Astron. Soc. **211**, 111 (1984).
5. A. S. Leonov and A. G. Yagola, Vestn. Mos. Univ., Ser. 3: Fiz. Astron. **2**, 14 (2000).
6. V. Yu. Terebizh, Astrofizika **33** (1) (1990).
7. A. N. Tikhonov, A. V. Goncharskii, V. V. Stepanov, and A. G. Yagola, *Numerical Methods for Solving Ill-posed Problems* (Nauka, Moscow, 1990) [in Russian].
8. A. V. Goncharskii, A. M. Cherepashchuk, and A. G. Yagola, *Ill-posed Problems in Astrophysics* (Nauka, Moscow, 1985) [in Russian].
9. A. V. Goncharskii, A. M. Cherepashchuk, and A. G. Yagola, *Numerical Methods for Solving Inverse Problems in Astrophysics* (Nauka, Moscow, 1978) [in Russian].
10. M. Houde and R. Racine, Astron. J. **107**, 466 (1994).
11. P. Magain, F. Courbin, and S. Sohy, astro-ph/9704059 (1997).
12. V. A. Belokurov, E. V. Shimanovskaya, M. V. Sazhin, *et al.*, Astron. Zh. **78**, 876 (2001) [Astron. Rep. **45**, 759 (2001)].
13. R. T. Corrigan, M. J. Irwin, J. Arnaud, *et al.*, Astron. J. **102** (1), 34 (1991).
14. R. Ostensen, S. Refsdal, R. Stabell, *et al.*, Astron. Astrophys. **309** (1), 59 (1996).
15. D. Alcalde, E. Mediavilla, O. Moreau, *et al.*, astro-ph/0204426 (2002).
16. E. Koptelova, E. Shimanovskaya, and V. Belokurov, astro-ph/0311508 (2003).
17. A. S. Leonov, Zh. Vych. Mat. Mat. Fiz. **36** (9), 35 (1996).
18. A. S. Leonov, Sib. Mat. Zh. **39** (1), 74 (1998).
19. A. S. Leonov, Sib. Zh. Vych. Mat. **2** (3), 257 (1999).
20. A. S. Leonov, Zh. Vych. Mat. Mat. Fiz. **39** (12), 1939 (1999).
21. I. Trujillo, W. Graham Alister, and N. Caon, astro-ph/0102393 (2001).
22. G. de Vaucouleurs, Ann. Astrophys. **11**, 247 (1948).
23. G. de Vaucouleurs, Hand. Phys. **53**, 311 (1959).
24. W. Press, S. Teukolsky, W. Vetterling, and B. Flannery, *Numerical Recipes in C: The Art of Scientific Computing* (Cambridge Univ. Press, Cambridge, 1998).
25. H.-W. Rix, D. P. Schneider, and J. N. Bachall, Astron. J. **104**, 959 (1992).

Translated by Yu. Dumin

Astronomy Reports, Vol. 48, No. 10, 2004, pp. 834–839. Translated from Astronomicheskiĭ Zhurnal, Vol. 81, No. 10, 2004, pp. 918–924.

A Statistical Analysis of Methanol Maser Groups

I. E. Val'tts and S. Yu. Lyubchenko

Astro Space Center, Lebedev Physical Institute, Russian Academy of Sciences, Profsoyuznaya ul. 84/32, Moscow, 117997 Russia

Received January 15, 2004; in final form, March 15, 2004

Abstract—An analysis of the flux densities of the 5_1–6_0A^+ (6.7 GHz) and 2_0–$3_{-1}E$ (12.2 GHz) class II methanol maser lines in a large and homogeneous sample of maser sources has been carried out. For convenience, the maser lines were divided into three groups: group I contains spectral features for the lines most prominent in the 5_1–6_0A^+ (6.7 GHz) transition, group II contains spectral features for the lines strongest in the 2_0–$3_{-1}E$ (12.2 GHz) transition, group III contains spectral features for which the velocities of the emission maxima of the two lines coincide. The same dependence was found for group II and group III: $\log S_{6.7} = (0.79 \pm 0.05) \times \log S_{12.2} + (0.79 \pm 0.05)$. The spectral features in group I do not obey this relation, and deviations from a linear dependence are considerably greater. It is suggested that methanol class II masers be divided into a subclass IIa, which has special conditions favoring 6.7 GHz masers, and a subclass IIb, which is comprised of the 12.2 GHz masers and those 6.7 GHz masers that necessarily accompany them under the same conditions. © *2004 MAIK "Nauka/Interperiodica"*.

1. INTRODUCTION

We have analyzed the parameters of the 5_1–6_0A^+ (6.7 GHz) and 2_0–$3_{-1}E$ (12.2 GHz) spectral lines (class II methanol maser lines) given by Caswell *et al.* [1], who present data for 131 sources. The LSR velocities of the emission maxima in the 2_0–$3_{-1}E$ (12.2 GHz) and 5_1–6_0A^+ (6.7 GHz) lines do not coincide in the spectra of 67 sources, and Caswell *et al.* [1] give parameters for two distinct spectral features in these lines. The LSR velocities of the maxima in the $2_0 - 3_{-1}E$ (12.2 GHz) and 5_1–6_0A^+ (6.7 GHz) lines coincide in the spectra of the other 64 sources, and parameters are given for a single spectral feature at each of the two frequencies. In other words, Caswell *et al.* [1] noted a lack of coincidence between the emission maxima in the 2_0–$3_{-1}E$ (12.2 GHz) and 5_1–6_0A^+ (6.7 GHz) lines in approximately half the investigated sources. This fact was also noted by Caswell *et al.* [2].

Our first attempts to analyze these lines were made in [3, 4]. In the current paper, we present a new approach—the identification of methanol maser groups—to understand why the maxima of these lines are sometimes not coincident.

2. ANALYSIS

We classified the spectral features observed by Caswell *et al.* [1] into three groups. Groups I and II contain lines for sources for which the maximum intensities of the 2_0–$3_{-1}E$ (12.2 GHz) and 5_1–6_0A^+ (6.7 GHz) lines do not occur at the same LSR velocity. The distinction between groups I and II is that group I contains lines for sources with stronger emission in the 5_1–6_0A^+ (6.7 GHz) transition, while group II contains lines for sources with stronger emission in the 2_0–$3_{-1}E$ (12.2 GHz) transition. There are 67 sources in these two groups. The third group contains the lines for the 64 sources for which the velocities of the emission maxima of the two lines coincide. We studied the distributions and dependences for 129 sources (two sources were excluded from the third group for reasons discussed below). Our analysis shows the following.

We first look at the average flux densities in the 5_1–6_0A^+ (6.7 GHz) line. The average flux density for group I features is considerably higher than for groups II and III, while the average flux densities in groups II and III are similar. When we consider the flux density ratios for the 5_1–6_0A^+ (6.7 GHz) and 2_0–$3_{-1}E$ (12.2 GHz) lines, it is clear that the group I features show significantly higher ratios (see Table 1).

Figures 1a–1c show the distributions of the line flux densities. These histograms illustrate the differences between the distributions of the 5_1–6_0A^+ (6.7 GHz) and 2_0–$3_{-1}E$ (12.2 GHz) maser flux densities in groups I, II and III, which are most substantial for group I. Figure 1a contains essentially no spectral features with flux densities below 10 Jy, while most of the spectral features in Fig. 1b have flux densities below 10 Jy.

Figures 2a–2c present the distributions of the line flux density ratios for the three groups. In the

1063-7729/04/4810-0834$26.00

Table 1. Average flux density in the $5_1{-}6_0A^+$ (6.7 GHz) and $2_0{-}3_{-1}E$ (12.2 GHz) lines

Group	Average 6.7 GHz flux density $\bar{S}_{6.7}$ (Jy)	Average 12.2 GHz flux density $\bar{S}_{12.2}$ (Jy)	$\bar{S}_{6.7}/\bar{S}_{12.2}$
Group I—maximum in the the $5_1{-}6_0A^+$ (6.7 GHz) line	207	25	8.3
Group II—maximum in the $2_0{-}3_{-1}E$ (12.2 GHz) line	118	45	2.6
Group III—maxima in either line	128	36	3.6

first group, the ratios cover a wide range: the flux densities of the $5_1{-}6_0A^+$ (6.7 GHz) and $2_0{-}3_{-1}E$ (12.2 GHz) lines can be nearly equal or can differ by as much as four orders of magnitude. In the second and, especially, the third groups, the flux densities are roughly equal (the difference is no more than an order of magnitude).

Figures 3a and 3b (logarithmic scale) show the relationship between the flux densities of the $5_1{-}6_0A^+$ (6.7 GHz) and $2_0{-}3_{-1}E$ (12.2 GHz) lines for the first and second groups. The first group is located above the approximation of the second group, and the second group is accordingly located below the approximation for nearly all sources in the first group.

Figure 4a shows the same dependence for the third group. We did not include two sources in these distributions: 24.33+0.14, for which $S_{12.2} > S_{6.7}$, and 9.62+0.20. The former object is a rare exception among the group III sources, and the latter is likewise obviously atypical for this group, since the flux density in the $5_1{-}6_0A^+$ (6.7 GHz) line exceeds that in the $2_0{-}3_{-1}E$ (12.2 GHz) line by a factor of 28, and the $5_1{-}6_0A^+$ (6.7 GHz) line itself is very bright, $S_{6.7} =$ 5090 Jy (this is the brightest known 6.7 GHz maser, see [1]). Including this line increases the average 6.7 GHz flux density by 62%, while including the corresponding $2_0{-}3_{-1}E$ (12.2 GHz) line ($S_{12.2} =$ 128 Jy) increases the average 12.2 GHz flux density by only 6%.

The parameters of the fit (on a log–log scale), are given in Table 2. The values of the parameter A for Fig. 3b and Fig. 4a are very similar, and we can approximate the data from groups II and III using the same dependence, $\log S_{6.7} = (0.79 \pm 0.05) \times \log S_{12.2} + (0.79 \pm 0.05)$. The spectral features of group I do not obey this relation.

This suggests that the physical conditions leading to the excitation of the masers are the same in groups II and III. Figure 4b presents a combination of the sources in the second and third groups. The parameters of the fit for these combined data are also given in Table 2, and it is clear that this is consistent with the individual fits for groups II and III. It is possible that the third group represents a mix of sources from groups I and II.

There are some grounds to suspect that 13 sources from group III (including 9.62+0.20) actually belong to group I (the 12 triangles in Fig. 4a above the approximation for group I), since the flux density $S_{6.7}$ for each of these sources is even larger than would be obtained using the approximation for group I from Table 2. Similarly, it is possible that 23 sources from group III actually belong to group II (the 23 open triangles below the approximation for group II in Fig. 4a). The flux density $S_{6.7}$ for each of these sources is even smaller than would be obtained using the approximation for group II from Table 2. We cannot identify the groups for the remaining 27 sources of the 64 in group III because they are consistent with both fits.

Caswell *et al.* [5] also present 6.7 GHz data for 107 sources, but with upper limits for the flux density of the 12.2 GHz line, which we can add to our sample. These 107 sources include some weak 6.7 GHz masers. If a 6.7 GHz maser is weak, the source could be either intrinsically weak or very distant. If the maser is very distant, but the upper limit for the 12.2 GHz flux density is physically real, the source could belong to group I, however we cannot be certain about this.

We used our fit for group I from Table 2 to find the minimum value for the 6.7 GHz flux density that corresponds to the limit of 0.4 Jy at 12.2 GHz from [5], which turns out to be 30 Jy. This indicates that 17 sources of the 107 may belong to group I.

We added 13 sources from group III and 17 sources from [5] to the distribution in Fig. 1a and 23 sources from group III to the distribution in Fig. 1b. The overall distributions are preserved but become better defined (Fig. 5).

The distributions in Figs. 1 and 5 indicate that the groups of maser features differ in both the coincidence or noncoincidence of the flux density maxima and

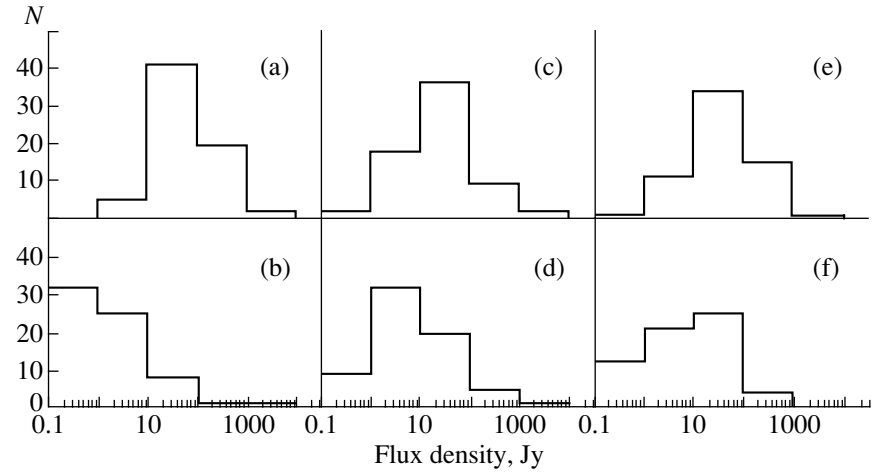

Fig. 1. Distribution of the 6.7 GHz (a, c, e) and 12.2 GHz (b, d, f) maser flux densities for the various samples identified (the upper panel shows the 6.7 GHz and lower panel the 12.2 GHz data). (a, b) Group I, with the maximum flux density in the $5_1-6_0A^+$ (6.7 GHz) line; (c, d) group II, with the maximum flux density in the $2_0-3_{-1}E$ (12.2 GHz) line; (e, f) group III, with maximum flux density in either line and coincident LSR velocities for both lines.

their line flux density ratios. We suggest that the difference in the ratios of the flux densities of the $5_1-6_0A^+$ (6.7 GHz) and $2_0-3_{-1}E$ (12.2 GHz) lines is more important than the coincidence or noncoincidence of the flux density maxima.

We believe that the differences in these line flux density ratios are associated with the physical properties in the sources, and suggest that class II methanol maser condensations be divided into two subclasses: subclass IIa, with brighter $5_1-6_0A^+$ (6.7 GHz) lines, and subclass IIb, with weaker $5_1-6_0A^+$ (6.7 GHz) lines. In other words, subclass IIa has special conditions favoring 6.7 GHz masers. Subclass IIb accounts for the 12.2 GHz masers and those 6.7 GHz masers that necessarily accompany them under the same conditions.

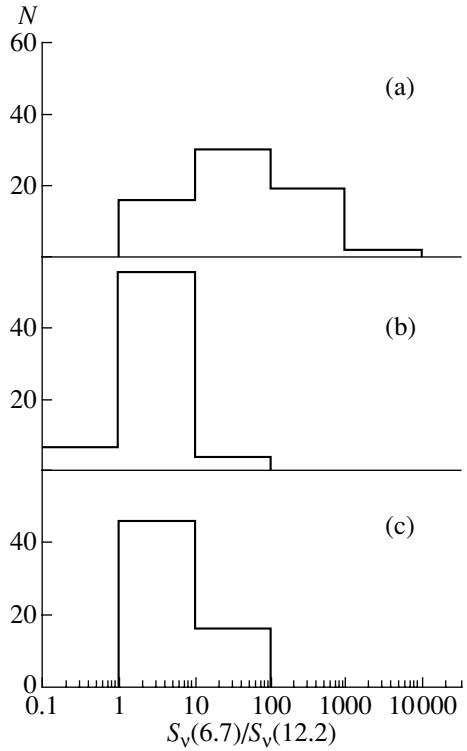

Fig. 2. Distribution of the ratio of the $5_1-6_0A^+$ (6.7 GHz) and $2_0-3_{-1}E$ (12.2 GHz) line flux densities (a) in the first, (b) second, and (c) third groups.

3. DISCUSSION

The existence of two subclasses of class II methanol masers can be explained as follows. We note first the following.

(1) Interferometric observations show that the maser condensations in which the $5_1-6_0A^+$ (6.7 GHz) and $2_0-3_{-1}E$ (12.2 GHz) lines are formed coincide spatially (see, for example, [6–8]).

(2) Theoretical models for the excitation of methanol masers [9–11] require different pumping mechanism for class I and class II methanol masers. We assume that the pumping source is external and is the same for all class II maser condensations within an astrophysical object.

(3) The $5_1-6_0A^+$ (6.7 GHz) line is usually brighter than the $2_0-3_{-1}E$ (12.2 GHz) line, due to its lower frequency and oscillator strength (see [11]).

Let us consider a maser condensation in a molecular cloud in which the $5_1-6_0A^+$ (6.7 GHz) and $2_0-3_{-1}E$ (12.2 GHz) lines are formed and the combinations of these lines could be observed in the source spectrum.

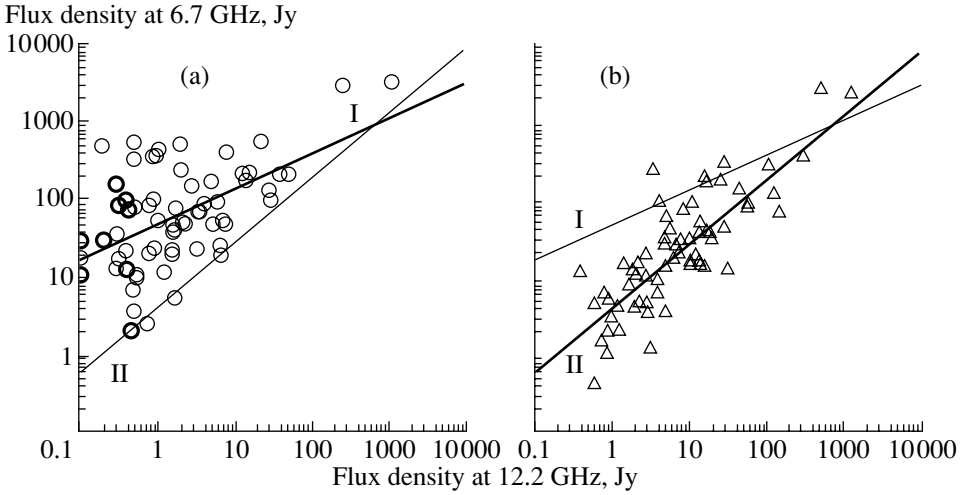

Fig. 3. Dependence between the flux densities of the $5_1{-}6_0A^+$ (6.7 GHz) and $2_0{-}3_{-1}E$ (12.2 GHz) lines in the (a) first and (b) second groups. The solid line is the approximation $\log y = A \log x + B$. The thin line in Fig. 3a is from Fig. 3b and vice verse. The bold circles in Fig. 3a denote sources for which there is an upper limit for the 12.2 GHz flux density from [5].

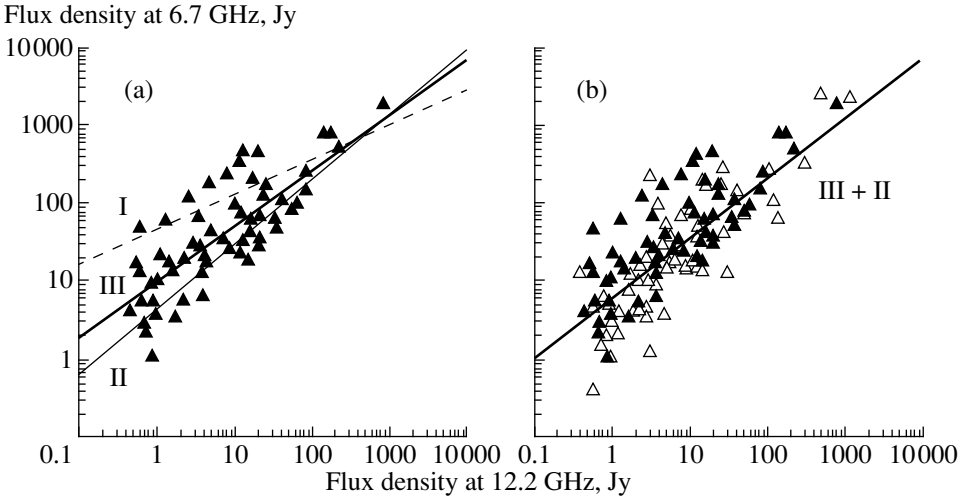

Fig. 4. Dependence between the flux densities of the $5_1{-}6_0A^+$ (6.7 GHz) and $2_0{-}3_{-1}E$ (12.2 GHz) lines in the (a) third group and (b) a mix of the second and third group. The dashed line (I) and thin line (II) are taken from Figs. 3a and 3b, respectively.

We will call the case when the maximum flux density is in the $5_1{-}6_0A^+$ (6.7 GHz) line m6, the case when the maximum flux density is in the $2_0{-}3_{-1}E$ (12.2 GHz) line m12, the usual case for the $5_1{-}6_0A^+$ (6.7 GHz) line (this line is not the maximum in the spectrum) u6, and the usual case for the $2_0{-}3_{-1}E$ (12.2 GHz) line u12. We can consider the following statistical combinations in the source spectrum: m6,u12 (group I); u6,m12 (group II); m6,m12 (group III); and u6,u12 (group IV).

Lines from all four groups could, in principle, be observed in the spectrum. Caswell *et al.* [1] present data for the first three combinations of lines, but not for the combination u6,u12 (group IV).

Statistically, the maxima of the $5_1{-}6_0A^+$ (6.7 GHz) and $2_0{-}3_{-1}E$ (12.2 GHz) lines should coincide or not coincide with equal probability, and we should therefore observe 50% of spectra to belong to group I and 50% to group II. Just this situation is reflected in Table 1 of [1]: the maxima coincide (64 sources) and do not coincide (67 sources) in roughly 50% of the sources.

If the $5_1{-}6_0A^+$ (6.7 GHz) and $2_0{-}3_{-1}E$ (12.2 GHz) lines are formed in different maser condensations, we should not detect any dependence between the flux densities of these spectral features. However, we have detected such a dependence. In this case, it is not a trivial fact that the line flux density ratio for the first group (m6, u12) differs from that

Table 2. Approximation parameters $\log y = A \log x + B$ for the dependences between the flux densities of the 5_1–6_0A^+ (6.7 GHz) and 2_0–$3_{-1}E$ (12.2 GHz) lines

Group	A	B	Correlation coefficient, r
Group I—maximum in the 5_1–6_0A^+ (6.7 GHz) line (Fig. 3a)	0.44 ± 0.09	1.69 ± 0.02	0.53
Group II—maximum in the 2_0–$3_{-1}E$ (12.2 GHz) line (Fig. 3b)	0.84 ± 0.07	0.60 ± 0.06	0.82
Group III—maxima in either line (Fig. 4a)	0.72 ± 0.07	0.97 ± 0.06	0.79
Mix of groups II and III (Fig. 4b)	0.79 ± 0.05	0.79 ± 0.05	0.79

for the second group (u6, m12). It seems that the flux densities of the 5_1–6_0A^+ (6.7 GHz) lines for the first group are too large, suggesting that some factor operates to provide additional amplification of the 5_1–6_0A^+ (6.7 GHz) line.

4. SUMMARY

(1) Masers with their maximum flux densities in the 5_1–6_0A^+ (6.7 GHz; m6, u12—group I) and in the 2_0–$3_{-1}E$ (12.2 GHz; u6, m12—group II) lines display different ratios of the flux densities in the 6.7 GHz and 12.2 GHz maser lines.

(2) Group III (m6, m12) contains spectral features for which the velocities of the emission maxima of these two lines coincide. In this group, the ratios of the flux densities in the 5_1–6_0A^+ (6.7 GHz) and 2_0–$3_{-1}E$ (12.2 GHz) lines are approximately the same as for group II.

(3) For the mixture of group II and group III represented by most of the investigated sources, we have found a single relation between the flux densities of the 5_1–6_0A^+ (6.7 GHz) and 2_0–$3_{-1}E$ (12.2 GHz) lines: ($\log S_{6.7} = (0.79 \pm 0.05) \times \log S_{12.2} + (0.79 \pm 0.05)$). This relation is very similar for group II and group III, and significantly different for group I. The studied interval of flux densities is higher than the detection limit, typically 0.3 Jy at 6.7 GHz [1] and 0.5 Jy at 12.2 GHz [5].

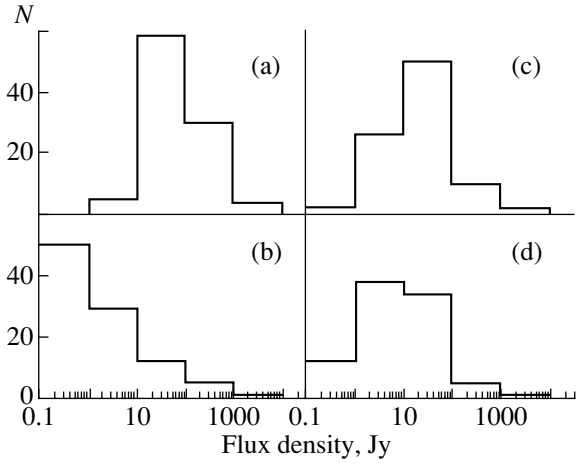

Fig. 5. Same distribution as in Fig. 1, but with 13 sources from group III and 17 sources from [5] added to the distributions in Figs. 1a, 1b, and with 23 sources from group III added to the distributions in Figs. 1c, 1d. See explanation in the text.

(4) We can divide some of the class II methanol masers into a subclass IIa, which has special conditions favoring 6.7 GHz masers, and a subclass IIb, which is comprised of the 12.2 GHz masers and those 6.7 GHz masers that necessarily accompany them under the same conditions.

The existence of two such subclasses can be tested by

—making an additional analysis of the data of Caswell *et al.* [1] to search for the fourth group of features;

—carrying out additional calculations of the methanol level populations and modeling the pumping conditions in view of observable effects;

—carrying out additional observations of class II methanol masers in the Northern hemisphere with high spectral resolution to increase the statistical reliability of the results;

—extending the analysis to weaker spectral features;

—making further interferometric observations to obtain more accurate flux densities for the individual maser spots;

—studying and taking into account the variability of the sources.

Spectral blending and variability could change the observed flux densities. Higher spatial resolution would make it possible to better separate the contributions of various maser spots. Variability is rarely high for 6.7 GHz masers [5], no more than 10% on a time scale of three months. It is slightly higher for 12.2 GHz masers [1, 5, 12, 13]. Because this variability is superposed with calibration uncertainties in the observations, we can only determine the scatter of the data points, but cannot derive corrections for the

variability. It is very important for our study that there be no velocity changes. Caswell *et al.* [5] have seen only changes of line profiles, as would be expected when two blended features vary by different amounts.

ACKNOWLEDGMENTS

We are grateful to J.L. Caswell for very useful comments. This work was supported by the Russian Foundation for Basic Research (project no. 01-02-16902), INTAS (grant N97-11451) and the CRDF (grant no. RP1-2392-MO-02).

REFERENCES

1. J. L. Caswell, R. A. Vaile, S. P. Ellingsen, *et al.*, Mon. Not. R. Astron. Soc. **274**, 1126 (1995).
2. J. L. Caswell, Yi. Jiyune, R. S. Booth, *et al.*, Mon. Not. R. Astron. Soc. **313**, 599 (2000).
3. I. E. Val'tts and S. Yu. Lyubchenko, *IAU Symp. No. 206: Cosmic Masers: from Protostars to Blackholes*, Ed. by V. Migenes and M. J. Reid., ASP Conf. Ser. **206**, 167 (2002).
4. I. E. Val'tts and S. Yu. Lyubchenko, Astron. Zh. **79**, 328 (2002) [Astron. Rep. **46**, 293 (2002)].
5. J. L. Caswell, R. A. Vaile, S. P. Ellingsen, *et al.*, Mon. Not. R. Astron. Soc. **272**, 96 (1995).
6. K. M. Menten, M. J. Reid, P. Pratap, *et al.*, Astrophys. J. **401**, L39 (1992).
7. R. P. Norris, J. B. Whiteoak, J. L. Caswell, *et al.*, Astrophys. J. **412**, 222 (1993).
8. V. Minier, R. S. Booth, and R. S. Conway, Astron. Astrophys. **362**, 1093 (2000).
9. K. M. Menten, in *Proceedings of the Third Haystack Observatory Conference "Atoms, Ions and Molecules*," Ed. by A. D. Hashick and P. T. P. Ho, ASP Conf. Ser. **16**, 119 (1991).
10. D. M. Cragg, K. P. Johns, P. D. Godfrey, and R. D. Brown, Mon. Not. R. Astron. Soc. **259**, 203 (1992).
11. A. M. Sobolev, D. M. Cragg, and P. D. Godfrey, Mon. Not. R. Astron. Soc. **288**, L39 (1997).
12. J. L. Caswell, R. A. Vaile, S. P. Ellingsen, *et al.*, Publ. Astron. Soc. Austral. **12**, 37 (1995).
13. G. C. MacLeod, M. J. Gaylard, and A. J. Kemball, Mon. Not. R. Astron. Soc. **262**, 343 (1993).

Translated by I. Val'tts

Astronomy Reports, Vol. 48, No. 10, 2004, pp. 840–852. Translated from Astronomicheskiĭ Zhurnal, Vol. 81, No. 10, 2004, pp. 925–937.

The Rapid Variability of Blazars at Optical Wavelengths

V. S. Bychkova[1], N. S. Kardashev[1], V. V. Vlasyuk[2], and O. I. Spiridonova[2]

[1] *Astrospace Center, Lebedev Physical Institute, Russian Academy of Sciences, Profsoyuznaya ul. 84/32, Moscow, 117810 Russia*

[2] *Special Astrophysical Observatory, Russian Academy of Sciences, Nizhniĭ Arkhyz, Karachaĭ-Cherkessian Republic, 357147 Russia*

Received December 24, 2003; in final form, March 15, 2004

Abstract—We monitored five active galactic nuclei in the R optical band with a CCD mounted on the 1-m Zeiss-1000 telescope of the Special Astrophysical Observatory from April 2001 to August 2003. Three sources displayed intraday variability on several nights. Stronger variability was detected on time scales from two days to a week. The two-year light curves are presented for four of the observed objects.

1. INTRODUCTION

Since the discovery of rapid variability of active galactic nuclei (primarily blazars) on time scales of a day, or even shorter [1, 2], the number of such objects has been steadily increasing with the amount of observational data. Such variability has been observed both from satellites and the ground, often synchronously at different wavelengths. In particular, numerous observations were made in 1990–1996 [2–4]; however, due to technical problems, insufficient weather conditions, and the faintness of the objects, no unified pattern for their behavior has emerged. Few observations have been made at optical wavelengths, although the comparison between optical and radio observations can indicate whether the variability is inherent to the objects or has an external origin, such as scintillation in the interstellar plasma.

To fill this gap, we carried out photometric observations of blazars previously noted for their rapid radio variability over two and a half years on the 1-m Zeiss telescope of the Special Astrophysical Observatory (SAO) of the Russian Academy of Sciences. We present here our results for five objects. Table 1 presents their coordinates and redshifts and Table 2 presents our main results.

2. OBSERVATIONS AND DATA PROCESSING

Our observations were carried out with an automated $UBVRI$ photometer at the Cassegrain focus of the Zeiss-1000 telescope of the SAO [5], using liquid-nitrogen-cooled CCD systems that were designed and constructed at the SAO, based on a low-noise 520×580 CCD array (in 2000 and 2001) and a 2048×2048 EEV 42-40 array (beginning in February 2002). The image scale for the 520×580 detector was $0.28 \times 0.37''$/pixel, and the field of view was $2.5' \times 3.5'$. The introduction of the thin, large EEV 42-40 detector with inverse illumination reduced the readout noise of the system from 12 to 3.5 electrons, enhanced its sensitivity by a factor of two to three (the quantum efficiencies of the CCD and EEV detectors at peak sensitivity at wavelengths near 550 nm were 45% and 90%, respectively), and increased the field of view to $7' \times 7'$. The upgraded parameters of the detector, together with its high quantum sensitivity and low readout noise, enabled us to obtain reliable photometric measurements of $19–20^m$ objects with 5–10 min exposures. The readout time for a total frame was 90 s; summing pixel-by-pixel, which yields an image scale of $0.43''$/pixel, reduced this time to less than 20 s. We reduced the photometric data using software developed at the SAO by Vlasyuk [6]. The observations were carried out in the R filter. The exposure time varied from 30 to 300 s, depending on the object's brightness, the weather conditions, and the required time resolution. The FWHM seeing varied from $0.9''$ to $3.5''$ from night to night, and was $2''$ on average.

The same standard procedure for processing the frames was used for both CCD systems. We subtracted an average corresponding dark frame from each frame, regardless of the level of the detected radiation. For the CCD detectors cooled to 120–130 K, the dark current did not exceed two to three electrons

1063-7729/04/4810-0840$26.00

Table 1. List of observed objects

Source Name	Coordinates (J2000)						z
	α			β			
[HB89] 0235+164	02^h	38^m	38.9^s	$+16°$	$36'$	$59''$	0.940
TXS 0917+624	09	21	36.2	+62	15	52	1.446
[HB89] 0954+658	09	58	47.2	+65	33	55	0.368
[HB89] 1308+326	13	10	28.6	+32	20	44	0.99
J 1819+3845	18	19	26.6	+38	45	02	0.54

for an individual exposure with a sky-background level of 50–100 electrons. We corrected for small-scale inhomogeneities in the detector's sensitivity and field vignetting using reference images of the evening and morning twilight sky.

The procedure used to estimate the brightnesses of the target and reference sources, which is described in detail in [6], is essentially a modified method for integrating the signals in annular apertures, rejecting readings that exceed a specified statistical level. We carried out photometric calibration for each target object using field objects. Further, the field-object brightnesses were used to determine the brightnesses of the targets during numerous measurements under varying weather conditions.

3. RESULTS

Table 2 presents the results of our observations. The columns contain (1) the name of the object, (2)–(3) the date and Julian date of the observations, (4) the number of observations per night, (5)–(6) the maximum and minimum R magnitude on each night, and (7) the rms error of the measurements. Figures 1–8 present R light curves for individual nights. The dashed lines indicate the rms errors (+/−) relative to the average amplitude.

3.1. The Blazar 0235+164

[HB89] 0235+164 is one of the brightest BL Lac objects displaying pronounced and sometimes rapid variability at various wavelengths [7]. It is a compact superluminal source [8]. Both intraday radio variability [4, 9, 10] and substantial high-energy variability [11] have been observed. The source has been observed fairly frequently in the optical. The object's light curve from 1974 to 2000 displays chaotic variations, with the brightness ranging from 15^m to 21^m over about 200 days [12]. Several rapid radio flares were detected during this period (lasting from half an hour to several hours). Three especially dramatic sets of brightness variations were observed.

(1) On January 17, 1999 (JD 2451196), brightness variations by 0.6^m (from 8.0^m to 18.6^m in several hours) were detected [12] during a decline of the overall light curve in a weak phase [13].

(2) For six nights (JD 2451485–2451490), 0.4^m–0.6^m flares were observed during a decline of the overall light curve between a brightness maximum and minimum [8].

(3) On December 5, 1994 (JD 2449692), a flare with an amplitude of 0.4^m occurring within a single night was detected during a decline of the overall light curve in a weak phase [13].

Our observations were carried out from September 2001 to March 2003. Figures 1a–1e present light curves covering several hours over five nights. We can see that the behavior of the blazar varies from night to night; variability over two to three hours is observed. The most pronounced variability was detected on October 11–12, 2001 (a change by 0.4^m within three hours; Fig. 1a), October 13–14, 2001 (a change by 0.4^m in one hour; Fig. 1b), October 14–15, 2001 (variations by up to 0.4^m over three hours; Fig. 1c), December 12–13, 2001, and November 27–28, 2002 (variations by up to 0.3^m–0.4^m over three hours (Figs. 1d, 1e).

Larger variations were observed on longer time scales from a day to a week. We detected seven intervals of such variability (Table 2, Figs. 2a–2f), with decreasing-brightness trends clearly seen within these intervals. The amplitude of the variations reaches 0.6^m (Figs. 2b, 2d, 2e). Figure 3 presents

Table 2. Results of the optical monitoring (N is the number of observations per night); with all dates in the form day interval. mm. yy.

Object	Date	JD	N	$R_{\max}$	$R_{\min}$	σ
[HB89] 0235+16	15/16.09.01	52169	8	18.52	18.60	0.05
	16/17.09.01	52170	17	18.56	18.82	0.04
	17/18.09.01	52171	11	18.69	18.83	0.04
	11/12.10.01	52195	15	17.80	18.18	0.04
	13/14.10.01	52197	9	17.81	18.13	0.04
	14/15.10.01	52198	18	18.18	18.45	0.05
	12/13.11.01	52227	17	17.33	17.46	0.02
	12/13.12.01	52257	23	17.38	17.72	0.03
	12/13.01.02	52288	7	17.12	17.20	0.03
	15/16.01.02	52291	23	17.17	17.32	0.04
	17/18.01.02	52293	20	17.23	17.55	0.05
	08/09.02.02	52314	7	16.22	16.39	0.03
	10/11.02.02	52316	8	16.65	16.75	0.02
	18/19.03.02	52352	4	16.69	16.76	0.05
	31.08/01.09.02	52518	9	17.69	18.01	0.07
	11/12.09.0	52529	9	17.94	18.41	0.01
	25/26.11.02	52604	10	16.81	16.90	0.02
	26/27.11.02	52605	3	16.87	17.08	0.04
	27/28.11.02	52606	24	16.09	16.35	0.02
	30.11/1.12.02	52609	13	16.60	16.67	0.02
	1/2.12.02	52610	30	16.35	16.75	0.02
	3/4.12.02	52612	4	16.57	16.65	0.02
	4/5.12.02	52613	4	16.43	16.48	0.02
	5/6.12.02	52614	3	16.64	16.67	0.02
	6/7.12.02	52615	6	17.07	17.14	0.01
	5/6.01.03	52645	4	17.94	18.20	0.02
	28.02/1.03.03	52699	3	16.94	16.96	0.01
	4/5.03.03	52703	3	17.15	17.49	0.03
	6/7.03.03	52705	3	17.25	17.27	0.02
[HB89] 0954+658	27/28.04.01	52028	19	16.46	16.70	0.02
	19/20.05.01	52050	8	16.54	16.67	0.02
	25/26.05.01	52056	23	16.80	16.96	0.02
	15/16.01.02	52291	15	16.22	16.35	0.02
	17/18.01.02	52293	36	15.81	16.06	0.02
	07/08.02.02	52313	32	15.86	16.02	0.02
	08/09.02.02	52314	25	15.91	16.01	0.01
	10/11.02.02	52316	5	15.84	15.94	0.01

Table 2. (Contd.)

Object	Date	JD	N	$R_{\max}$	$R_{\min}$	σ
	17/18.03.02	52351	53	15.16	15.48	0.01
	18/19.03.02	52352	100	15.41	15.65	0.02
	12/13.04.02	52377	3	16.63	16.81	0.06
	09/10.05.02	52404	5	16.97	17.08	0.01
	10/11.05.02	52405	3	16.92	16.94	0.01
	13/14.05.02	52408	3	16.86	16.95	0.01
	04/05.06.02	52430	3	16.14	16.20	0.06
	09/10.06.02	52435	3	16.04	16.06	0.01
	10/11.06.02	52436	3	16.01	16.06	0.02
	11/12/06.02	52437	2	16.20	16.20	0.03
	01/02.07.02	52457	3	16.21	16.25	0.02
	02/03.07.02	52458	3	16.32	16.36	0.02
	03/04.07.02	52459	3	16.43	16.53	0.03
	05/06.07.02	52461	3	16.47	16.55	0.02
	07/08.07.02	52463	3	16.57	16.58	0.02
	09/10.07.02	52465	3	16.64	16.70	0.02
	10/11.07.02	52466	3	16.42	16.52	0.02
	11/12.07.02	52467	3	16.34	16.41	0.01
	12/13.07.02	52468	2	16.29	16.50	0.01
	13/14.07.02	52469	3	16.41	16.44	0.02
	29/30.07.02	52485	3	15.94	16.03	0.02
	30/31.07.02	52486	3	16.03	16.04	0.01
	08/09.08.02	52495	3	16.35	16.41	0.02
	30/31.08.02	52517	3	16.18	16.22	0.02
	10/11.09.02	52528	3	16.48	16.57	0.01
	27/28.11.02	52606	6	16.46	16.49	0.01
	02/03.12.02	52611	5	16.14	16.17	0.01
	07/08.02.03	52678	2	15.93	16.11	0.03
	08/09.02.03	52679	3	15.81	15.91	0.05
	28.02/01.03.03	52699	2	16.08	16.10	0.01
	02/03.03.03	52701	4	15.70	15.80	0.03
	03/04.03.03	52702	50	15.88	16.24	0.04
	04/05.03.03	52703	3	15.95	16.03	0.01
	06/07.03.03	52705	49	15.43	15.67	0.02
TXS 0917+624	28/29.04.01	52028	11	21.50	21.79	0.09
	07/08.02.02	52313	3	21.13	21.38	0.09
	08/09.02.02	52314	5	21.41	21.69	0.10

Table 2. (Contd.)

Object	Date	JD	N	$R_{\max}$	$R_{\min}$	σ
	10/11.02.02	52316	6	21.06	21.49	0.09
	17/18.03.02	52351	3	21.25	21.47	0.10
	09/10.05.02	52404	3	21.22	21.33	0.08
	10/11.05.02	52405	3	21.13	21.14	0.10
	13/14.05.02	52408	3	21.08	21.17	0.10
	09/10.06.02	52435	3	21.09	21.40	0.10
	01/02.07.02	52457	3	20.98	21.32	0.10
	09/10.07.02	52465	3	21.04	21.16	0.11
	11/12.07.02	52467	3	20.86	21.08	0.10
	31.07/01.08.02	52487	4	20.87	21.67	0.09
	02/03.12.02	52611	4	20.79	21.01	0.07
	08/09.02.03	52679	3	21.08	21.17	0.09
	28.02/01.03.03	52699	2	20.99	21.13	0.03
	06/07.03.03	52705	3	21.04	21.13	0.04
	01/02.04.03	52731	3	21.25	21.49	0.05
	23/24.04.03	52753	3	20.97	21.03	0.03
	04/05.05.03	52764	3	20.90	21.01	0.03
	22/23.05.03	52782	2	20.89	20.98	0.03
[HB89] 1308+326	21/22.06.01	52082	13	17.13	17.33	0.03
	23/24.06.01	52084	10	17.09	17.30	0.02
	29/30.06.01	52090	10	17.09	17.34	0.02
	30.06/1.07.01	52091	13	16.91	17.35	0.03
	12/13/01/02	52288	5	15.63	15.74	0.06
	08/09.02.02	52314	5	16.09	16.23	0.03
	10/11.02.02	52316	5	16.10	16.17	0.02
	17/18.03.02	52351	3	16.06	16.08	0.02
	12/13.04.02	52377	3	16.48	16.49	0.01
	10/11.05.02	52405	19	15.97	16.09	0.02
	13/14.05.02	52408	3	15.81	15.86	0.02
	09/10.06.02	52435	3	15.67	15.88	0.03
	10/11.06.02	52436	71	15.72	15.97	0.05
	05/06/07.02	52461	3	15.68	15.79	0.05
	07/08.07.02	52463	3	15.66	15.70	0.03
	09/10.07.02	52465	3	15.80	15.81	0.03
	10/11.07.02	52466	4	15.79	15.89	0.02
	31.07/01.08.02	52487	4	15.86	15.93	0.02
	08/09.12.02	52700	3	15.11	15.12	0.01

Table 2. (Contd.)

Object	Date	JD	N	$R_{\max}$	$R_{\min}$	σ
	28/29.03.03	52727	3	15.21	15.27	0.02
	28/29.04.03	52758	2	16.20	16.20	0.01
	29/30.04.03	52759	3	16.11	16.16	0.01
	02/03.05.03	52762	3	15.92	16.03	0.01
	23/24.05.03	52783	2	16.46	16.51	0.01
	24/25.05.03	52784	4	16.47	16.53	0.01
	25/26.05.03	52785	15	16.36	16.43	0.01
	24/25.06.03	52815	3	16.01	16.07	0.01
	01/02.08.03	52853	3	16.25	16.30	0.02
MG3 J181925+3844	08/09.08.00	51764	1	20.37	20.37	0.30
	22/23.08.00	51778	2	19.52	19.86	0.16
	25/26.05.01	52055	2	19.79	19.84	0.10
	20/21.06.01	52081	3	19.71	19.73	0.10
	23/24.06.01	52084	2	20.03	20.10	0.10
	11/12.08.01	52133	1		20.26	0.15
	17/18.08.01	52139	1		19.98	0.10
	16/17.09.01	52169	1		20.19	0.15
	17/18.09.01	52170	2	20.14	20.22	0.15
	11/12.10.01	52194	3	19.85	20.13	0.13
	10/11.02.02	52316	3	19.98	20.01	0.12
	17/18.03.02	52351	3	19.86	20.39	0.13
	12/13.04.02	52377	2	20.18	20.22	0.10
	10/11.05.02	52405	1		20.18	0.13
	13/14.05.02	52408	3	19.96	20.28	0.12
	03/04.06.02	52429	2	19.77	19.90	0.09
	10/11.06.02	52436	1		19.57	0.13
	02/03.07.02	52458	2	19.83	19.93	0.10
	05/06.07.02	52461	2	20.08	20.20	0.12
	07/08.07.02	52463	2	19.91	20.01	0.09
	09/10.07.02	52465	2	19.96	19.98	0.10
	10/11.07.02	52466	2	19.86	19.94	0.10
	30/31.07.02	52486	2	19.72	19.93	0.12
	30/31.08.02	52517	2	19.85	19.92	0.12
	31.08/01.09.02	52518	6	19.77	19.93	0.10
	10/11.09.02	52528	3	20.03	20.11	0.06
	27/28.11.02	52606	1		20.10	0.17
	02/03.12.02	52611	2	19.97	19.99	0.11
	03/04.12.02	52612	3	19.79	19.83	0.20
	04/05.12.02	52613	1		19.04	0.30
	05/06.12.02	52614	1		19.88	0.12

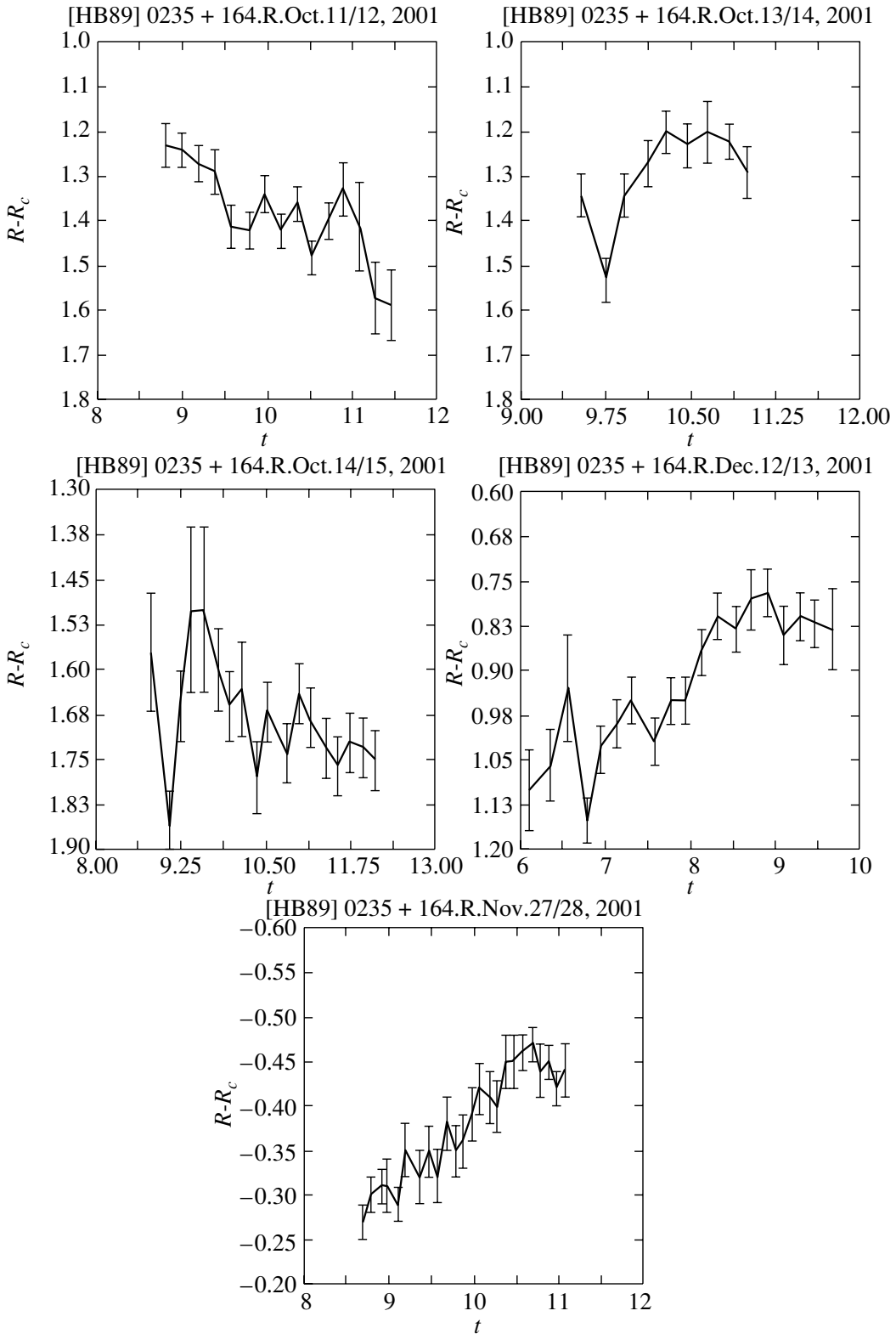

Fig. 1. *R* light curves of the blazar [HB89] 0235+164 for characteristic time intervals of two to six hours. The horizontal axis plots the time in hours, and the vertical axis plots the difference between the magnitudes of the target and a reference star. The headers above the panels give the name of the object, the filter used, and the date of the observations.

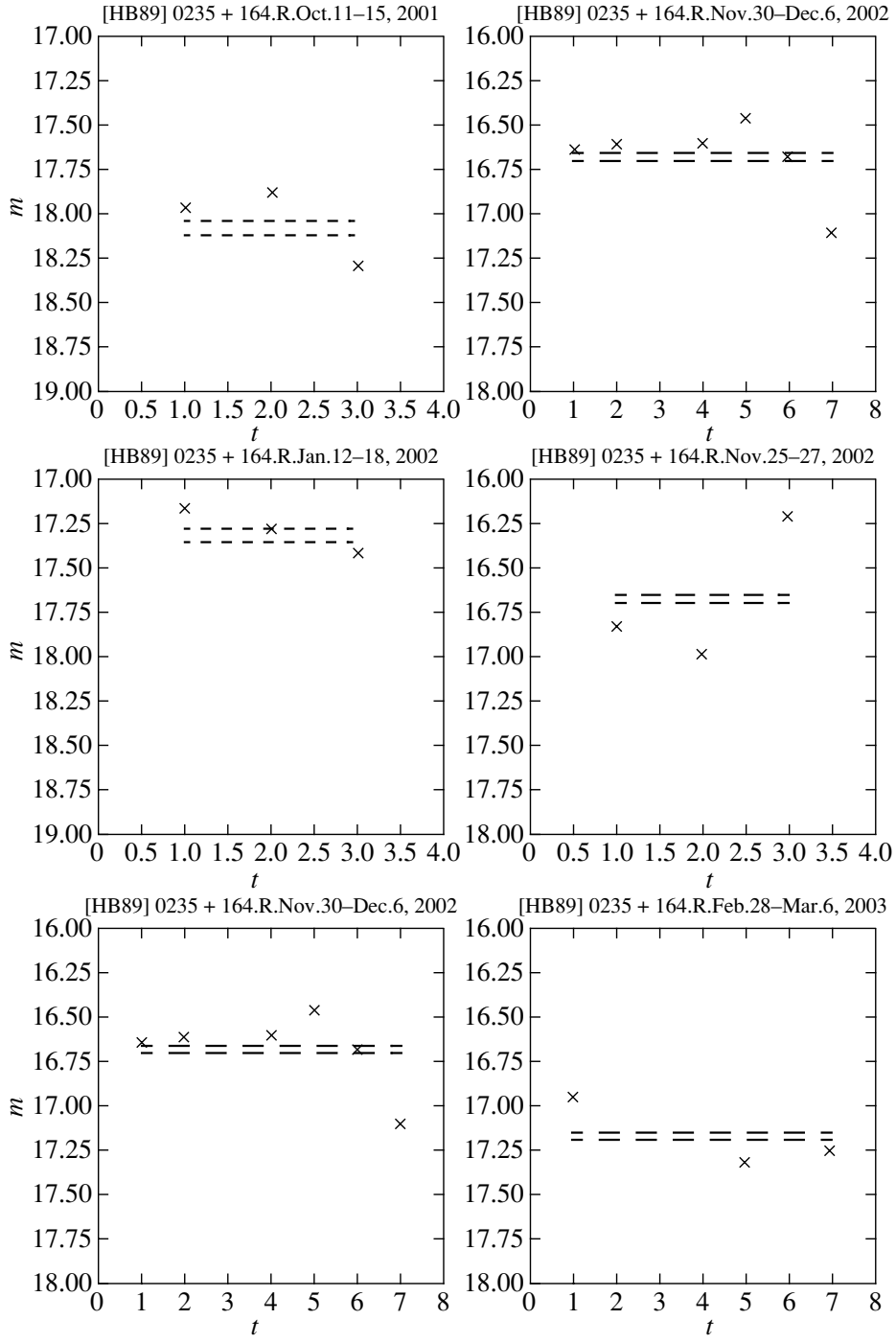

Fig. 2. R light curves of [HB89] 0235+164 over three to seven day intervals. The horizontal axis plots the time in days. The crosses denote the mean magnitudes for each night, and the dashed lines show the rms errors relative to the mean magnitude for the entire interval. The header notation is the same as in Fig. 1.

the overall light curve from September 2001 to March 2003. During the first 200 days, the object increased in brightness from 18.5^m to 16^m; during the last 300 days, sharp brightness variations by more than 1.5^m over 10–40 days are visible. We attempted to find a correlation between the amplitudes of short-time-scale flares and the long-time-scale brightness variations (over about a year). However, it is clear that the available data, both those published earlier and our new data, do not indicate any kind of correlation:

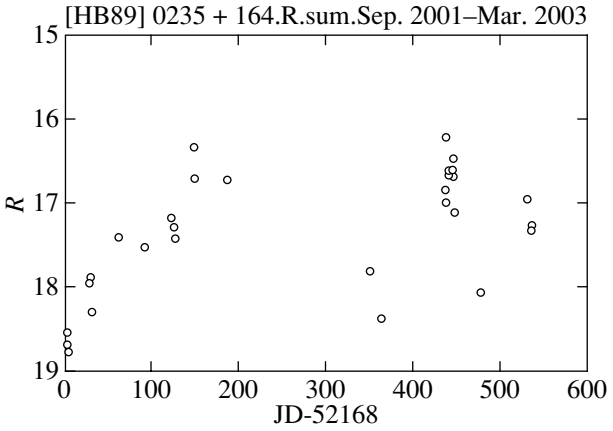

Fig. 3. Overall R light curve for [HB89] 0235+164 over two years. The horizontal axis plots the time (JD-52168). The header notation is the same as in Fig. 1.

flare activity is manifest in phases of both declining and increasing brightness.

The Blazar 0954+658

The BL Lac object [HB89] 0954+658 has a radio core and a superluminal jet. Strong gamma radiation has been detected [14]. It is one of the brightest blazars at optical wavelengths, and has been observed in numerous studies aimed primarily at detecting intraday variability in the R band [3, 15, 16]. Rapid radio variability was detected in 1987 [17]. The synchronous optical and radio observations of Wagner *et al.* [3, 16] revealed rapid, correlated variability in both wavelength bands. Satellite observations of the object have been carried out in the IR, X-ray, and gamma-ray bands, but no apparent variability has been detected [13]. The longest light curve is presented by Raiteri *et al.* [14], and includes optical ($BVRI$) and radio (4.8, 14.5, 22, and 37 GHz) data from November 1994 to May 1998, JD 2449600–2451000. The optical brightness varies by as much as 2^m within 50–100 days.

Optical intraday variations have been observed by several different groups [10, 14, 16]; the amplitude of these variations can reach 0.1^m–0.2^m within several hours. Our R observations were carried out from April 2001 to March 2003, when the object was in a phase of increasing brightness. Intraday variations by 0.2^m–0.3^m within two to three hours were detected on several occasions. Figures 4a–4c present the behavior displayed by the variations over time intervals of between half an hour and four hours. The largest variations occurred on April 27–28, 2001 and March 6–7, 2003. Substantial variability on longer time scales from a day to a week (Figs. 5a–5f) was observed on May 19–26, 2001, when the brightness decreased by 0.25^m for a day (Fig. 5a), January 15–18, 2002, when the object became brighter by more than 0.3^m (Fig. 5b) for a day, and February 28–March 6, 2003, when the amplitude of the brightness variations reached 0.6^m (Fig. 5f). Figure 6 presents the overall light curve from April 2001 to April 2003. The brightness variations in this interval reached 2^m. Unfortunately, we did not have enough data to establish whether there is any relation between the amplitude of the flares and their position in the overall light curve.

TXS 0917+624

TXS 0917+624 is a quasar with a redshift of 1.446. In 1987, Heeschen *et al.* [2] detected variations by up to 4% at 11 cm over two to four days. The synchronous polarization observations at five wavelengths from 2 to 20 cm of Qian *et al.* [18] revealed rapid variations on time scales of 0.3–1.3 days. The analysis of Rickett [19] suggested that these rapid variations could be explained by interstellar scintillation. VLBI images at 2.3 to 22 GHz show a compact core and a jet extending toward the northwest [20]. Synchronous optical and radio observations did not show any variability within a few percent. The quasar has been detected in X-rays [20]. It is likely that the rapid radio variations of TXS 0917+624 are due to its extremely small angular size, which gives rise to scintillations of the radio flux due to the interstellar medium [21, 22]. No systematic optical observations of the object have been published.

We observed 0917+624 in the R filter on individual nights from April 2001 to May 2003, with three to ten exposures per night separated by 10-min intervals. The brightness variations reached 0.3^m; however, due to the object's faintness, the errors were fairly large and no intraday variability on short timescales was detected. The variations were also small on longer timescales from days to a week (Table 2). Figure 7 presents the overall R light curve over the two years from April 2001 to May 2003. The brightness variations did not exceed 0.5^m during this time interval.

[HB89] 1308+326

[HB89] 1308+326 is classified as a BL Lac object due to its nearly featureless optical spectrum, appreciable optical variability, and strong polarization [23, 24]; it also displays variable emission lines [25]. No variability was detected in simultaneous X-ray,

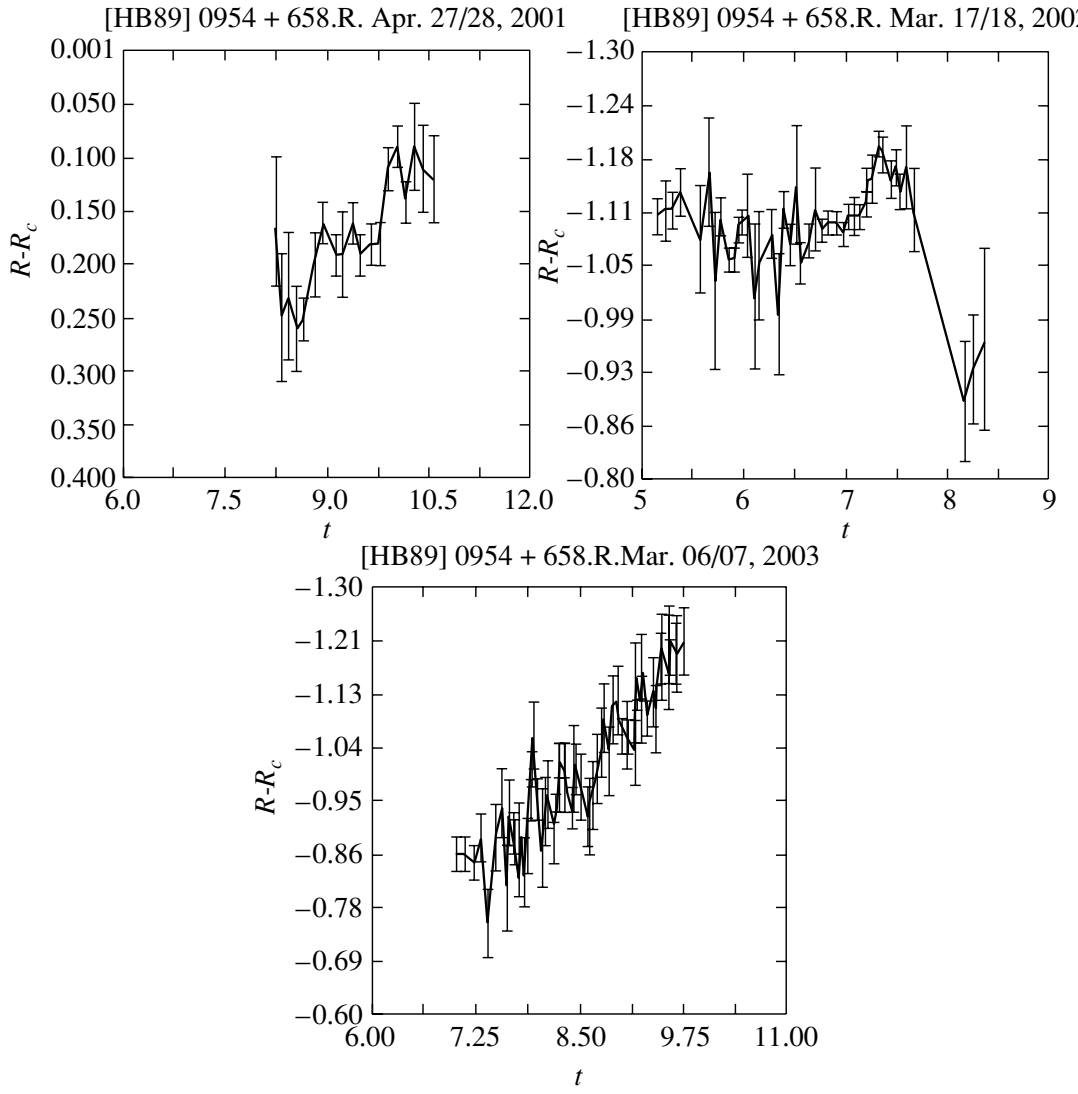

Fig. 4. *R* light curves of the blazar [HB89] 0954+658 for individual nights. The horizontal axis plots the time in hours, and the vertical axis plots the difference between the magnitudes of the target and a reference star. The header notation is the same as in Fig. 1.

optical (V), and radio observations in June 1996. Long-time-scale radio variability has been observed in a number of studies: for example, Tornikoski *et al.* [26] present light curves at 90 and 37 GHz from 1980 to 1994. Long-time-scale variability by up to 2^m–4^m has been observed over time intervals of from 200 days to several years [27, 28]. The object is suspected of being a rapid variable [17]; however, thus far, no appreciable short-time-scale variability has been observed at either radio or optical wavelengths.

Our monitoring was carried out from June 2001 to August 2003. The most appreciable rapid variability (by 0.4^m) was detected on June 24–25, 2001 (Table 2). On the other nights, any intraday variability did not exceed 0.2^m. The brightness increased by more than 1.5^m over the entire period of the observations (Fig. 8).

MG3 J181925+3844

MG3 J181925+3844 is a recently discovered object classified as a quasar with a redshift of 0.54. It is distinguished by its unusually high-amplitude (up to 300%) rapid (over less than an hour) radio variability at various frequencies. This variability has been shown to be due to interstellar scintillations [29]. The quasar is faint (20^m–21^m), and had not been

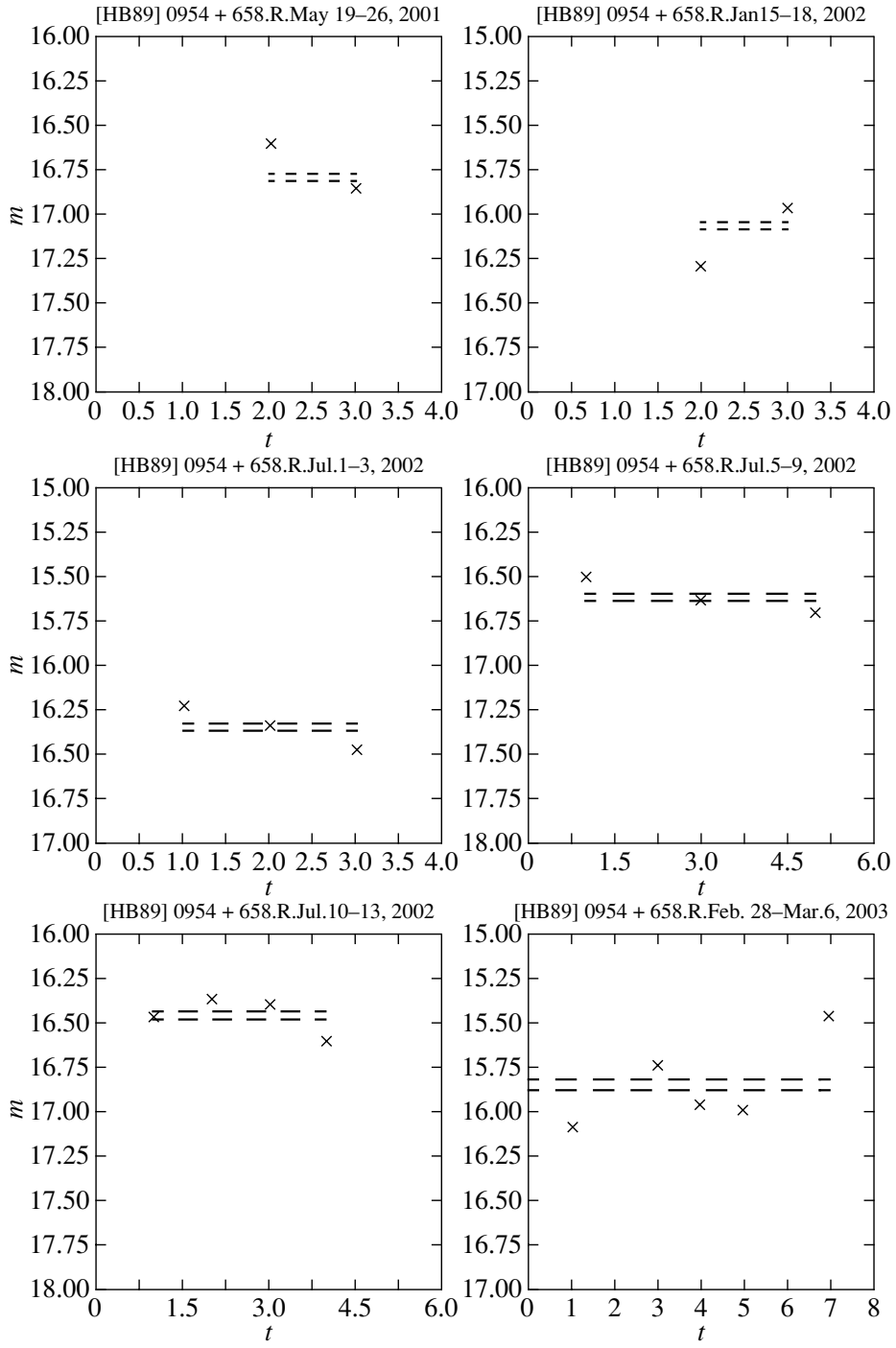

Fig. 5. *R* light curves of [HB89] 0954+658 over two to seven days. The horizontal axis plots the time in days. The notation is the same as in Fig. 2, and the header notation is the same as in Fig. 1.

systematically observed at optical wavelengths prior to our monitoring.

Our observations were carried out from August 22, 2000 to December 6, 2002. The variability observed was within the observational errors (Table 2).

Thus, three of five of our selected targets displayed rapid variability on time scales of hours or days. The source brightnesses can vary by several magnitudes within time intervals of about a year. The data clearly show that the rapid variability can correspond to

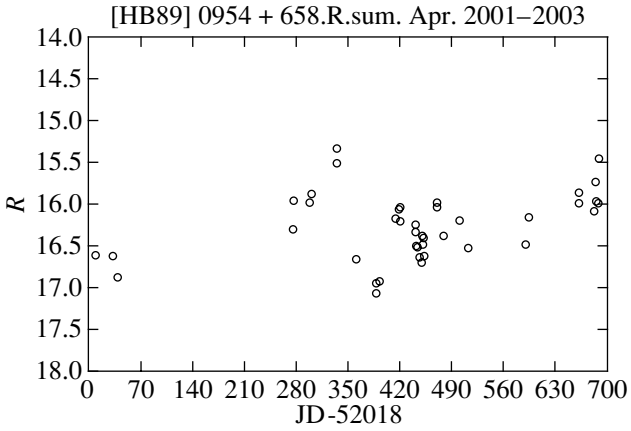

Fig. 6. Overall R light curve of the blazar [HB89] 0954+658 over two years. The horizontal axis plots the time (JD-52018). The header notation is the same as in Fig. 1.

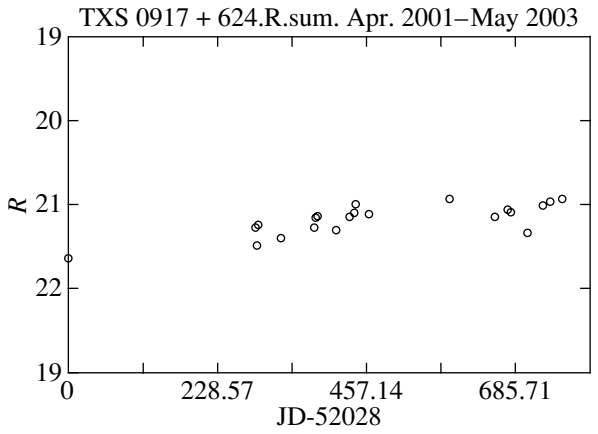

Fig. 7. Overall light curve of TXS 0917+624 over two years. The horizontal axis plots the time (JD-52028). The header notation is the same as in Fig. 1.

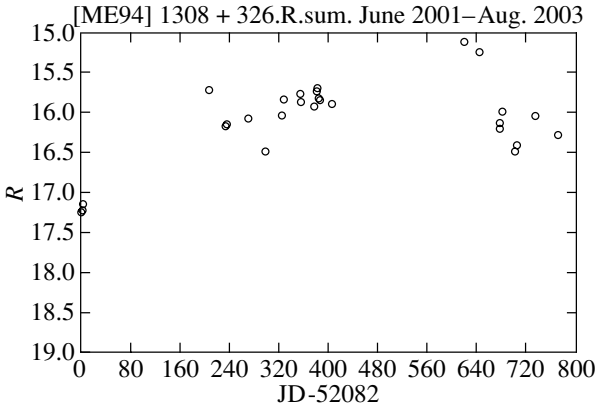

Fig. 8. Overall light curve of [ME94] 1308+326 over two years. The horizontal axis plots the time (JD-52082). The header notation is the same as in Fig. 1.

either an overall increase or decrease of the source brightness.

ACKNOWLEDGMENTS

The authors thank their colleagues É.A. Vitrichenko and M.V. Popov for useful discussions. This work was supported by the Russian Foundation for Basic Research (project no. 02-02-16305) and the Project in Support of Leading Scientific Schools of the Russian Federation (grant NSH-1653.2003.2).

REFERENCES

1. S. J. Wagner and A. Witzel, Ann. Rev. Astron. Astrophys. **33**, 163 (1995).
2. D. S. Heeschen, T. Krichbaum, C. J. Schalinski, *et al.*, Astron. J. **94**, 1493 (1987).
3. S. Wagner, F. Sanchez-Pons, A. Quirrenbach, *et al.*, Astron. Astrophys. **235**, L1 (1990).
4. A. Quirrenbach, A. Witzel, T. P. Krichbaum, *et al.*, Astron. Astrophys. **258**, 279 (1992).
5. V. I. Zin'kovskii, S. S. Kaisin, A. I. Kopylov, *et al.*, Tekh. Otchet SAO RAN, No. 321 (1994).
6. V. V. Vlasyuk, Astrofiz. Issled., Byull. SAO RAN **36**, 107 (1993).
7. M. Roy, I. E. Paradakis, E. Ramos-Coldon, *et al.*, Astrophys. J. **545**, 758 (2000).
8. G. E. Romero, S. A. Cellone, and J. A. Combi, Astron. Astrophys. **360**, L47 (2000).
9. G. E. Romero, J. A. Combi, P. Benaglia, *et al.*, Astron. Astrophys. **326**, 77 (1997).
10. R. Sagar, Gopal Krishna, *et al.*, Astrophys. J. **586**, L25 (2003).
11. R. C. Hartman, D. L. Bertsch, S. D. Bloom, *et al.*, Astrophys. J., Suppl. Ser. **123**, 79 (1999).
12. J. R. Webb, E. Howard, E. Benitez, *et al.*, Astron. J. **120**, 41 (2000).
13. G. S. Xie, K. H. Li, J. M. Bai, *et al.*, Astrophys. J. **548**, 200 (2001).
14. C. M. Raiteri, M. Villata, G. Tosti, *et al.*, Astron. Astrophys. **352**, 19 (1999).
15. J. Height and S. J. Wagner, Astron. Astrophys. **305**, 42 (1996).
16. S. J. Wagner, A. Witzel, T. P. Krichbaum, *et al.*, Astron. Astrophys. **271**, 344 (1993).
17. R. Fiedler, B. Dennison, K. Johnston, *et al.*, Nature **326**, 675 (1987).
18. S. J. Qian, A. Quirrenbach, A. Witzel, *et al.*, Astron. Astrophys. **241**, 15 (1991).
19. J. Rickett, A. Quirrenbach, and R. Wegner, Astron. Astrophys. **293**, 479 (1995).
20. K. J. Standke, A. Quirrenbach, T. P. Krichbaum, *et al.*, Astron. Astrophys. **306**, 27 (1996).
21. B. J. Rickett, A. Witzell, A. Kraus, *et al.*, Astrophys. J. **550**, L11 (2001).
22. S. J. Qian, A. Witzel, A. Kraus, *et al.*, Astron. Astrophys. **367**, 770 (2001).

23. D. Watson, N. Smith, L. Hanlon, *et al.*, Astron. Astrophys. **364**, 43 (2000).
24. M. Stickel, J. W. Fried, H. Kuhr, *et al.*, Astrophys. J. **374**, 431 (1991).
25. R. Scarpa and R. Falomo, Astron. Astrophys. **325**, 109 (1997).
26. M. Tornikoski, E. Valtaoja, H. Terasranta, *et al.*, Astron. Astrophys. **289**, 673 (1994).
27. J. H. Fan and R. J. Lin, Astrophys. J. **537**, 101 (2000).
28. J. H. Fan and R. J. Lin, Astrophys. J., Suppl. Ser. **121**, 131 (1999).
29. J. Dennett-Thorne and A. G. de Bruyn, Astrophys. J. **529**, L65 (2000).

Translated by K. Maslennikov

Astronomy Reports, Vol. 48, No. 10, 2004, pp. 853–870. Translated from Astronomicheskiĭ Zhurnal, Vol. 81, No. 10, 2004, pp. 938–955.

A Comparative Analysis of Zebra-Pattern Structures at Frequencies from 20 to 7000 MHz

G. P. Chernov

Institute of Terrestrial Magnetism, the Ionosphere, and Radio Wave Propagation, Troitsk, Russia

Received January 5, 2004; in final form, March 15, 2004

Abstract—A joint analysis of several recent solar type IV radio outbursts with zebra structures and fiber bursts in their dynamical radio spectra is carried out using all available ground-based and satellite data (Yohkoh, SOHO, TRACE). Zebra structures and fiber bursts were observed at frequencies from 20 to 6500 MHz. The main relative spectral parameters and degree of circular polarization of the zebra structures and fiber bursts are nearly the same. The relative width of the zebra structures varies only slightly with frequency ($\approx$0.003–0.005); the radio emission is radiated in the ordinary mode. New data on centimeter-wavelength zebra structures and fiber bursts testifies that they are analogous to similar structures observed at meter wavelengths. A double-plasma-resonance model for the zebra structures based on the observational dependences for the electron density and magnetic field yields a frequency dependence for the frequency separation between stripes that does not agree with the observations. Fine structure was observed together with the rise into the corona of new, hot magnetic loops, in which instabilities associated with high-frequency and low-frequency plasma waves develop. The frequency range of the fine structure in the dynamical spectra is probably determined by the extent of these new loops in the corona. The continuous transition of the fiber bursts into zebra structures and vice versa testifies to a single origin for these two structures. All the main properties of the stripes in emission and absorption can be explained if they are associated with interactions between electrostatic plasma waves and whistlers. It is possible to obtain realistic values for the magnetic-field strength of $B \approx 160$ G at a plasma level of about 3 GHz in this model. © *2004 MAIK "Nauka/Interperiodica".*

1. INTRODUCTION

Stripes of emission and absorption in the form of the more or less regular zebra-pattern structures or of fiber bursts with an intermediate frequency drift against the continuum emission of type IV radio outbursts at meter or decimeter wavelengths were first classified and studied more than 20 years ago [1, 2]. More recent 2.6–3.8 GHz observations with high resolution (10 MHz in 8 ms) using the new spectrograph of the Beijing Astronomical Observatory testify that this type of fine structure displays the same variety at centimeter wavelengths as well [3].

The interpretation of this complex fine structure has always lagged somewhat behind the detection of new, even more varied observational phenomena. However, the generally accepted mechanism for the radio emission of fiber bursts is interactions between electrostatic plasma waves (l) and whistlers (w), both excited by the same population of fast electrons, which has a conical velocity distribution, with the ordinary waves (t) freely escaping: $l + w \rightarrow t$ [4].

The development of the theory of the zebra-pattern structures has been much more complicated; more than ten different models have been proposed, most of them including some role by the emission of electrostatic plasma waves at the double plasma-resonance frequency [4–7]:

$$\omega_{UH} = (\omega_{Pe}^2 + \omega_{Be}^2)^{1/2} = s\omega_{Be}, \qquad (1)$$

where ω_{UH} is the upper-hybrid frequency, ω_{Pe} is the electron plasma frequency, ω_{Be} is the electron cyclotron frequency, and s is the harmonic number. The model that best describes the observations and the conditions in the corona is the model of [7], which is based on unsaturated electron-cyclotron maser emission by electrons with a conical distribution.

However, all these theoretical models developed to explain the zebra structures encounter a number of difficulties.

(1) Irregular structure in the stripes is often observed, although the frequency separations between the zebra-pattern stripes Δf_s should be approximately equal to the electron cyclotron frequency (depending on the relationship between the density and magnetic-field scale heights), and should decrease smoothly with height in the corona. Estimates of Δf_s are presented in [5] for the case when the magnetic-field scale height is much larger than the

1063-7729/04/4810-0853$26.00

electron-density scale height, $L_B \gg L_N$; i.e., when $\Delta f_s \approx f_{Be}$.

(2) The magnetic fields derived based on Δf_s always turn out to be so low that it is difficult to obtain $\beta \approx (v_s/v_A)^2 \ll 1$ for this plasma parameter (the obvious value for a magnetic trap above an active region, where v_s and v_A are the sound speed and the Alfven speed, respectively). This has led many authors to adopt the opposite relationship between the scale heights, $L_B \ll L_N$, but this does not solve this problem, since the real relationship between the two scale heights remains unknown.

(3) Nearly all the models are devised to explain stripes in emission, although stripes predominantly in absorption are also sometimes observed.

(4) All the models assume the important property that the electrons have a conical velocity distribution. This distribution also generates whistlers, and the interaction of these whistlers with fast particles cardinally changes the velocity distribution—the transverse anisotropy is decreased, and bunching of the longitudinal velocities arises.

In addition, the main spectral properties and radio polarizations of the zebra stripes and fiber bursts coincide, which suggests that these two structures are created by a single mechanism, based on the merging of plasma waves and whistlers, but with different conditions for instability of the whistlers.

An entire magnetic trap is filled by periodic wave packets made up of whistlers excited by a conical distribution of fast electrons at the cyclotron resonance:

$$\omega_w - k_{||} v_{||} - s\omega_{Be} = 0, \qquad (2)$$

where ω_w is the whistler frequency, $k_{||}$ is the whistler wave number, and $v_{||}$ is the velocity of the fast electrons along the magnetic field.

Depending on the form of the distribution function, instability develops either for the normal Doppler effect ($s = +1$), when whistlers propagate toward fast particles along magnetic-field lines, leading to the formation of a fiber burst, or in an anomalous resonance [$s = -1$ in (2)], when the whistlers propagate toward fast particles at a large angle to the magnetic field, forming zebra stripes with a different frequency drift [8–10]. The rapid periodicity of the whistler instability is associated primarily with the quasi-linear nature of the instability (the scattering of whistlers on fast particles), which leads to periodic disruptions of the instability of the electrostatic waves in the volume of the whistler wave packet. This effect gives rise to bands of absorption that accompany both fiber bursts and zebra stripes of emission [11]. Whistlers can contribute to the formation of bands of emission and absorption as a result of their interaction with plasma waves at both the sum and the different frequencies, $\omega_l \pm \omega_w = \omega_t$ [9, 12, 13].

The unsatisfactory lack of a single generally accepted theory for the zebra-pattern structure has unfortunately stimulated many authors to devise new versions of models based on the double plasma resonance [14, 15]. Ledenev *et al.* [14] suggest that the magnetic field falls off with height in the corona much more rapidly than the density. Under the assumption that radiation is emitted at the second harmonic, ω_{UH}, they obtained more realistic values for the magnetic field, comparable to those obtained in [3] for whistler models. However, the zebra structure is usually strongly polarized (it only very rarely has low polarization), which excludes the possibility that this emission is radiated at the second harmonic. Therefore, the B values turn out to be overestimated by more than a factor of two; in addition, the harmonic number s was chosen arbitrarily.

In an attempt to remove the problem of the low magnetic field that is implied by assuming that the radiation is associated with the double plasma resonance, LaBelle *et al.* [16] proposed a new theory for zebra structures based on the radiation of auroral "choruses"—magnetospheric outbursts detected at ground-based stations at frequencies of 2–4 MHz, which have fine structure similar to that of the zebra-pattern structure. This model proposes that the radiation is emitted in the cyclotron-maser Z mode (by analogy with [7]). Although the upper-hybrid-frequency Z-mode radiation itself does not emerge from the source, this radiation can be transformed into ordinary-mode (O-mode) radiation at discrete frequencies (the eigenharmonics) in the presence of density inhomogeneities on the corresponding scales. These discrete frequencies arise due to the quantization in the conditions of the eiconal when the wave passes through an Ellis window for the corresponding azimuthal (m) and radial (n) quantum numbers in the eiconal conditions. The Z mode can be generated in a point source at one level of the double plasma resonance [$s = \text{const} = 2$ in (1)]. The main difference and advantage of this model is that it can explain the formation of a large number of harmonics (up to 100) with a small frequency separation $\Delta f_s \approx 0.01 f_{Be}$. LaBelle *et al.* [16] estimated the degree (<10%) and size (1–100 m) of the density inhomogeneities. Such inhomogeneities could be created by dispersional ion–acoustic waves. However, LaBelle *et al.* [16] do not discuss one important aspect of the problem—the time dependence of the eigenharmonics (the dynamics of the zebra-pattern structure); they only mention the possibiity that the inhomogeneities could be stable over ~10 s. They likewise do not discuss the conditions for the excitation of the ion–acoustic waves and the main condition that

the electron temperature greatly exceed the ion temperature ($T_e \gg T_i$). In addition, the summing of the contributions of numerous inhomogeneities (created by propagating ion–acoustic waves) should lead to blending of the stripes into the continuum. The simultaneous appearance of fiber bursts against the zebra structure is likewise not considered. We will discuss other discrepancies with the observations in Section 3 below.

Observations of zebra structure at the harmonic frequencies 1700 and 3400 MHz were first discussed in [17]. However, the absence of polarization information and the lack of similarity between the zebra structures at the harmonic frequencies casts doubt on the reality of this harmonic structure.

Observations of fine structures have been considerably expanded in recent years, leading to the discovery of new effects in the zebra structure. Analyses of new events now usually include a more complete study of flare processes contributing to the X-ray emission (Yohkoh/SXT) and the ultraviolet lines (SOHO and TRACE). It is therefore important at this stage to identify new properties of the fine structure observed at various frequencies and analyze them in the context of various theoretical models; this is the goal of the current paper.

Zebra-pattern structures and fiber bursts are sometimes not observed simultaneously over a wide range of frequencies spanning decameter to decimeter wavelengths. On the contrary, the frequency bands occupied by the fine structure associated with a single event are usually $\leq$50 MHz at meter wavelengths and several hundreds of MHz at decimeter wavelengths. We will compare the relative parameters of the zebra structures at different frequencies and attempt to answer the question of why these frequency bands are so narrow. We analyze four radio outbursts displaying fine structure at meter wavelengths (the events of May 2, 1998, July 28, 1999, September 23, 1998, and October 25, 1994) and two such outbursts at centimeter wavelengths (October 29, 2000 and April 21, 2002).

2. DESCRIPTION OF THE EVENTS

Several major type IV radio outbursts displaying fine structure in the form of emission and absorption stripes (zebra-pattern structure and fiber bursts) were observed with several radio spectrographs [ARTEMIS (Nancay), 100–500 MHz; IZMIRAN (Institute of Terrestrial Magnetism, the Ionosphere, and Radio Wave Propagation), 25–270 MHz; PHOENIX-2, 220–549 MHz; Nancay, 20–70 MHz; Potsdam (Tremsdorf), 40–800 MHz; Beijing Astronomical Observatory, 2.6–3.8 and 5.2–7.6 GHz], as well as with the Nancay radioheliograph and the Trieste Astronomical Observatory polarimeter at 237, 327, and 408 MHz. We also used all available higher-frequency data for the analysis, including images in UV lines obtained with the SOHO and TRACE satellites and in the soft X-ray with Yohkoh/SXT. This enabled us to carry out a comparative analysis of the zebra structures over a wide range of frequencies from 30 to 6500 MHz.

2.1. Event of May 2, 1998

Zebra-pattern structures were first observed for event of May 2, 1998 at low frequencies between 22–46 MHz (Fig. 1). The radio event was simultaneous with a large 3B X1.1 flare at 13:30–13:42–15:13 UT in the active region NOAA 8210, with coordinates S15W15. The SOHO LASCO telescope detected a major halo-type coronal mass ejection (CME) extending to 26 $R_\odot$.

The radio event included a large group of type III outbursts, two type II outbursts, and type IV continuum radiation. A global dynamical spectrum is presented in [18]. The maximum energy release in the corona occurred at the heights where the decimeter radiation was generated (22 000 s.f.u. at 606 MHz), but the event continued into interplanetary space, expressed via a type II and very weak type III outburst.

Zebra-pattern structure was observed over approximately three minutes, in the form of structure in the flare continuum after the strong type II and type III outbursts. The dynamical spectrum shown in the upper panel in Fig. 1 shows that the zebra structure consists of numerous fragments of stripes with various frequency drifts. The most substantial long fragment resembles a narrow-band braid of stripes (or short-time-scale fiber bursts) with a constant frequency drift. This main braid of fibers, which lasted about two minutes, forms the low-frequency boundary of all the zebra-pattern fragments. These fragments also form braids of fibers occupying various frequency bands at higher frequencies.

The frequency drift of the main braid is approximately -0.13 MHz/s near 37 MHz, which corresponds to a speed for the propagation of the excitation in the outer layers of the corona of about 2200 km/s (if we use a double Newkirk model for the electron density). The frequency-drift rate is approximately -0.04 MHz/s, which corresponds to a motional velocity of 700 km/s. We should note two more important properties of the main braid: its frequency width increased from 0.25 MHz at 43 MHz to 0.8 MHz at 22 MHz, accompanied by an appreciable decrease in the left-circular polarization.

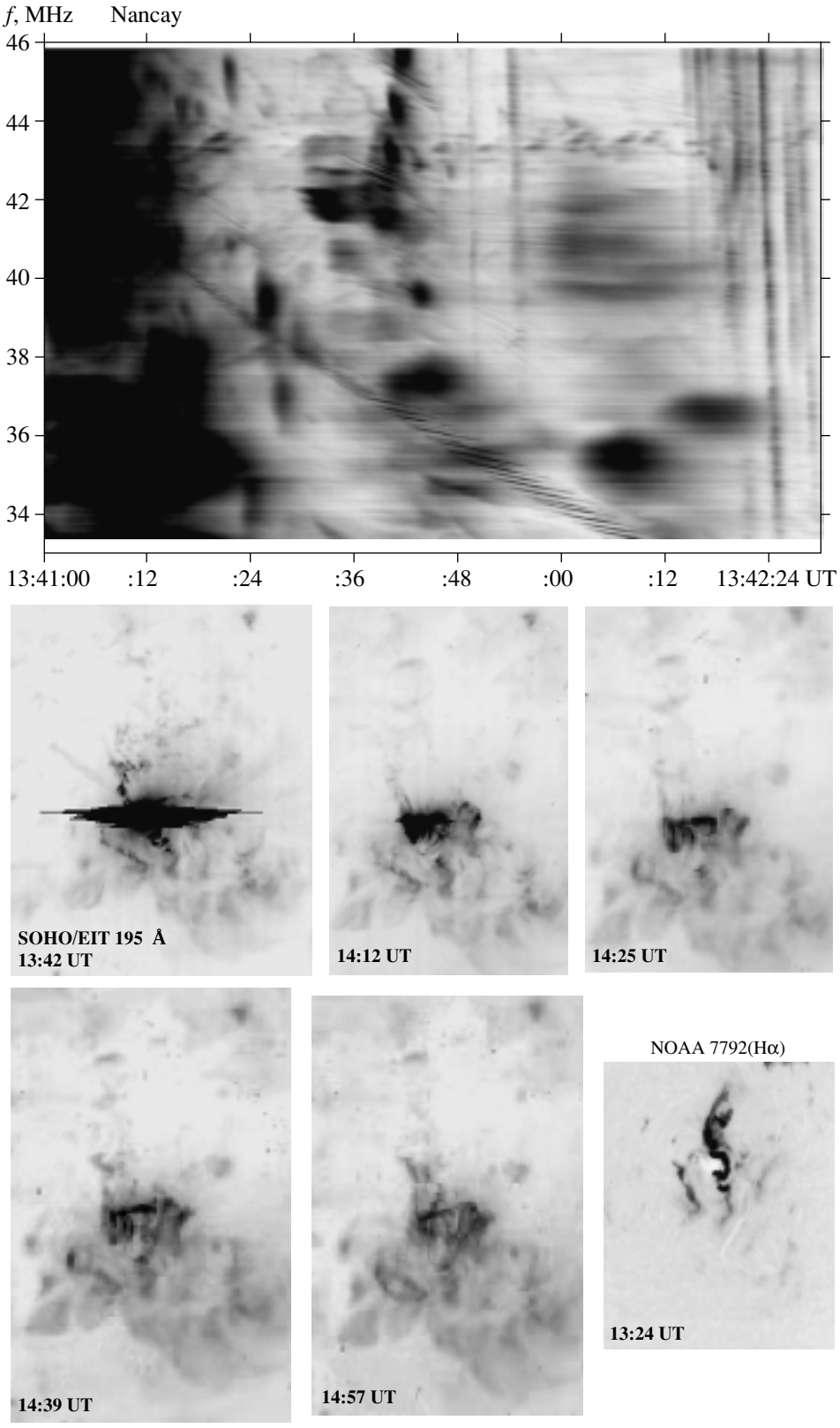

Fig. 1. Event of May 2, 1998. The top panel shows the dynamical spectrum obtained using the DSP decameter spectropolarimeter of the Nancay Observatory (the time resolution is 0.05 s). The lower panels show the development of the outburst in the 195 Å EUV line (SOHO/EIT) and the Hα emission in the active region (NOAA 7792).

The width of the frequency bands for individual stripes of emission was approximately the same for all the zebra-structure fragments, $\Delta f \approx 0.08$ MHz, with the relative width of these bands being $\Delta f/f \approx 0.0024$. However, the frequency separations between the stripes of emission were appreciably different in different fragments ($\Delta f_s \approx 0.08$–0.17 MHz), and the short-time-scale stripes within the main braid are not strictly periodic in frequency. In some fragments, a frequency shift toward lower frequencies is observed between an emission stripe and the neighboring absorption stripe, Δf_{ea}. This shift is approximately equal to Δf.

The radio emission of all components of the type II and type III outbursts was essentially unpolarized, while the main braid displayed strong left-circular polarization. Other fragments of the zebra structure displayed moderate left-circular polarization, while still others even displayed moderate right-circular polarization.

Two-dimensional NRH images of the 164 MHz radio sources obtained show four radio sources above active region NOAA 8210. The complex behavior of the polarization of the fine structure may indicate that different radio sources are located in regions with different magnetic polarities.

The lower part of Fig. 1 displays the evolution of the flare in the 195 Å EUV line (five frames from SOHO/EIT MPEG film), while the fifth lower panel shows the onset of the Hα flare. We can see in this last panel that a helmetlike ejection has already formed over the sigmoid flare ribbon by 13:24 UT. The continuation of this ejection is clearly visible in the first 195 Å frame, which corresponds to the maximum of the flare (13:42 UT). Each subsequent frame contains new fragments of ejected material in projection onto the disk. It is obvious that, after the CME, the energy release proceeded in a vertical current layer, as a magnetic structure with magnetic islands was established.

2.2. Event of July 28, 1999

The radio event consisted of a prolonged type IV outburst with zebra structure in the interval 08:15–10:30 UT, associated with a modest 1B M2.3 flare with its maximum at 08:14 UT in the active region NOAA 8649 (S15E03). The flare was accompanied by a halo-type CME at 09:06 UT. We can identify three main intervals in which fine structure was displayed: 08:15–08:30 UT, in the impulsive phase, 08:50–09:25 UT, at the maximum, and 10:15–10:30 UT, in the decay phase. In the first two intervals, the zebra-pattern structure is chaotic on short time scales (less than one minute) in narrow frequency bands (of 50–150 MHz) between 200 and 1500 MHz. In the decay phase, the zebra structure is displayed nearly continuously at 300–400 MHz.

The upper left panel in Fig. 2 shows the zebra structure at the end of the impulsive phase observed at IZMIRAN at 200–270 MHz. The upper right panel presents the zebra structure obtained on the Phoenix-2 specrograph at 320–385 MHz during the decay phase. We can see in the left panel that the zebra stripes drift toward high frequencies, as is often observed. The right panel displays various drifts, but the overall tendency is for the zebra stripes to drift toward lower frequencies, and the stripes in this part of the spectrum resemble fiber bursts.

A common feature of the stripes observed in these two frequency bands is the presence of absorption relative to the mean continuum level at the low-frequency edge of the emission stripes, as is confirmed by the left- and right-circular polarization profiles for 237 MHz (left) and 327 MHz (right) presented in the central panels of Fig. 2 (data of the Trieste Astronomical Observatory). The degree of left-circular polarization was initially moderate (30–40%), becoming stronger at the end of the event (60–80%). The dips in intensity in the absorption bands were 20–30% of the mean continuum level.

After the maximum of the event at about 08:55 UT, unusual stripes of emission with absorption on both the low-frequency and high-frequency sides began to appear, together with individual bands of pure absorption. Further, after 10:19 UT, nearly all the zebra stripes and individual fiber bursts had their absorption on the opposite (high-frequency) edge. The stripes displayed a continuous variation of the frequency drift in this interval, from negative to positive, in the form of cascades of U flares. In this case, the zebra stripes made a continuous transformation into fiber bursts and vice versa. Two such cascades are visible in the right-hand spectrum in Fig. 2.

The three lower panels in Fig. 2 show the evolution of the flare at 195 Å displayed by SOHO/EIT data. The flare began above a neutral magnetic-field line, with zebra-pattern structure observed at 08:15 UT simultaneous with the rise of a new loop (toward the southwest in projection), shown by the arrow in the left panel. This loop continued to rise until 08:25 UT, and the NRH data show that the 327 MHz radio source was located above this loop. The position of this source is marked by a white plus in the central panel.

At the time of the event's maximum, new bright flare centers were ignited to the west of the main flare. In the decay phase, a new loop began to rise above these centers, and the radio sources that appeared during the decay-phase zebra structure were located above this new loop; the 327 MHz and 164 MHz

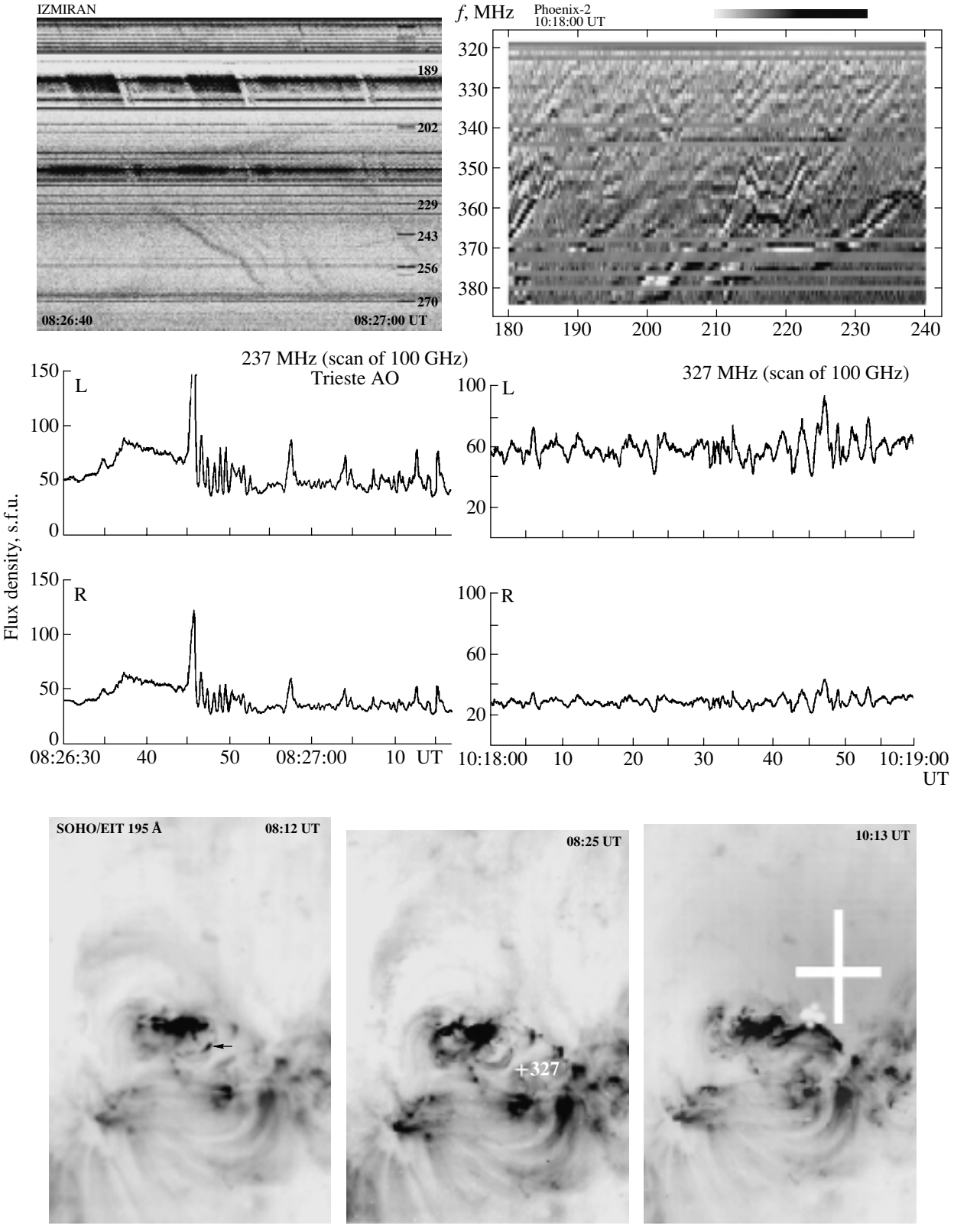

Fig. 2. Event of July 28, 1999. The upper panel shows two spectra of the zebra structure during two active periods at 08:26 UT (left, the IZMIRAN spectrograph,189–270 MHz) and 10:18 UT (right, the Phoenix-2 spectrograph, 320–385 MHz). The central panels show temporal profiles of the L and R chanels of the Trieste Astronomical Observatory polarimeter at 237 and 327 MHz. The lower panels show the evolution in the 195 Å EUV line (SOHO/EIT). The arrow in the left frame shows the rise of a new loop. The white pluses in the other frames show the positions of the centers of the radio sources at 327 MHz (small) and 164 MHz (large).

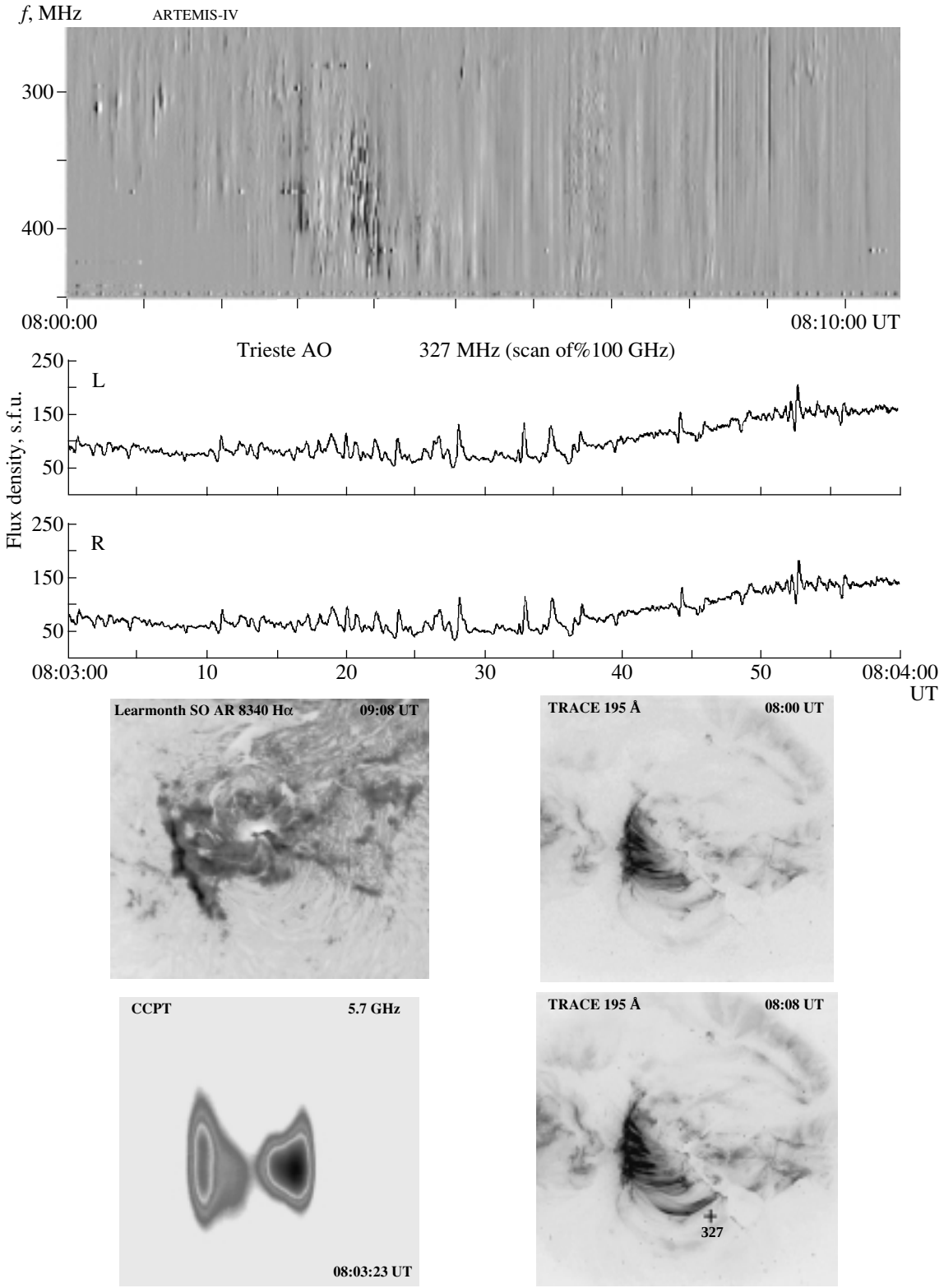

Fig. 3. Event of September 23, 1998. The upper panel shows the fine structure displayed between 08:00 and 08:10 UT at 250–450 MHz (the ARTEMIS-IV spectrograph, Greece). The next panel presents time profiles of the L and R channels of the Trieste Astronomical Observatory polarimeter at 327 MHz, which show weak left-circular polarization. The lower set of panels present the development of the Hα flare (upper left; Learmonth Solar Observatory), two EUV 195 Å frames, which show numerous hot loops between two parts of the neutral line (right; TRACE), and the radio brightness distribution at 5.7 GHz (lower left; CCPT). The position of the center of the radio source at 327 MHz (NRH) is indicated by the cross above the new loop at 08:08 UT.

radio sources are marked by the small and large white pluses in the central and right panels of Fig. 2.

2.3. Event of September 23, 1998

According to Solar Geophysical Data (SGD), a 3B M7.1 flare began at 06:40 UT in the active region NOAA 8340 (N18E09), reaching its maximum at 07:13 UT. The radio event was observed from 06:52–11:00 UT, and included a type II outburst (06:52–07:02 UT) and a prolonged type IV outburst with several maxima. Zebra structure was observed in the interval 08:00–08:10 UT. In the spectrum in the upper panel of Fig. 3, obtained with the new ARTEMIS-IV spectrograph (Greece) at 250–450 MHz, we can see a fiber burst (08:03–08:04 UT), riblike zebra structure (08:05–08:06 UT), and rapid pulsations in emission and absorption (08:08–08:09 UT). Below the spectrum, a rare property of the fine structure is visible in the 327-MHz polarization profiles obtained at the Trieste Astronomical Observatory: the radiation displayed very weak left-circular polarization. These profiles also show that the dips in intensity in the absorption stripes comprise about 20–30% of the mean continuum level. The zebra structure observed at 08:06–08:07 UT was most pronounced in absorption, and the rapid pulsations observed at 08:08–08:09 UT were also purely in absorption (i.e., they were "sudden reductions").

The evolution of the flare is illustrated in four different panels in the lower part of Fig. 3. A two-ribbon Hα flare was observed over three hours along the eastern and western parts of a neutral line of the magnetic field. The two TRACE 195 Å frames show numerous bright loops that appear (and disappear) betwen these two parts of the neutral line. A new bright loop appeared in the southern part of the flare region at 08:00 UT, and the center of the 327 MHz radio source observed at 08:08 UT (NRH) coincides with this new loop in the 195 Å TRACE frame.

Many aspects of the structure of the radio sources and the fine structure of the radio emission at centimeter wavelengths have been studied in [19, 20]. For our analysis, it is important that the 5.7 GHz radio source observed by the CCPT has a double structure, with the source on the right (which was located near the eastern part of the neutral line and was closest to the position of the meter-wavelength source) being brighter at 08:03 UT (Fig. 3, lower left panel). The dynamics of the 195 Å flare loops (TRACE) are impressive: every few minutes over three hours, new loops were ignited and rose high into the corona. The onset of the type II outburst was accompanied by flare ejections toward the southwest observed in the 1550 Å line (SOHO/ZUMER). Several minutes later, a dark region that can be considered a flare coronal hole (or dimming) formed at the location of this ejection, and was subsequently observable for many hours in the 195 Å line (TRACE).

2.4. Event of October 25, 1994

Beginning at 10:00 UT, the meter-wavelength radio event included a type II outburst at frequencies below 90 MHz, which had drifted to 40 MHz by 10:06 UT, and a brief type IV outburst (flare continuum) with fine structure in the form of periodic type III outbursts between 10:05:18 and 10:08:35 UT and zebra-pattern structure between 10:08:00 and 10:09:00 UT. The upper panel of Fig. 4 shows the dynamical spectrum obtained on the ARTEMIS spectrograph (Nancay Observatory) at 100–500 MHz. The type III outbursts have a very high frequency-drift rate (possibly associated with an enhanced plasma density above the flare region). However, this frequency-drift rate is lower at lower frequencies. The main energy release occurred at meter wavelengths. The maximum flux at 204 MHz was 300–400 s.f.u. between 10:08 and 10:09 UT.

A modest centimeter-wavelength flare (a 49 s.f.u. GRF) was observed over an hour, and an even more prolonged C4.7 soft X-ray (1–8 Å) flare was detected by the GOES-7 satellite. According to SGD 608 II, a modest 1N-magnitude Hα flare began at 09:40 (reaching its maximum at 10:04 UT and its end at 12:36 UT) in active region NOAA 7792 (S09W12). An active dark fiber and system of filaments were also visible above this active region.

Some aspects of the type IV radio outburst, which displayed various source positions outside the active region, are discussed in [21]. In the superposition of the 164 MHz radio source and the soft X-ray (Yohkon/SXT) A1.1 image shown in the lower left panel of Fig. 4, the center of the radio source is located outside the active region. At this same time, the main continuum source coincided with the main flare region in the soft X-ray. Each subsequent X-ray frame contains new bright loops, both inside and outside the main flare region, providing evidence for magnetic reconnection occurring in neighboring loops. Thus, it is likely that the repeated radio flares at 327 and 408 MHz had different circular polarizations. The maximum brightening in soft X-rays occurred at 09:59 UT, before the type II outburst, and at 10:08 UT, during the type III outbursts in the same location, at the center of the active region, above the magnetic-field neutral line. The sigmoid shape of the soft X-ray flare repeats the shape of the neutral line. Manoharan *et al.* [22] suggest that the flare acted as a trigger for large-scale magnetic reconnection.

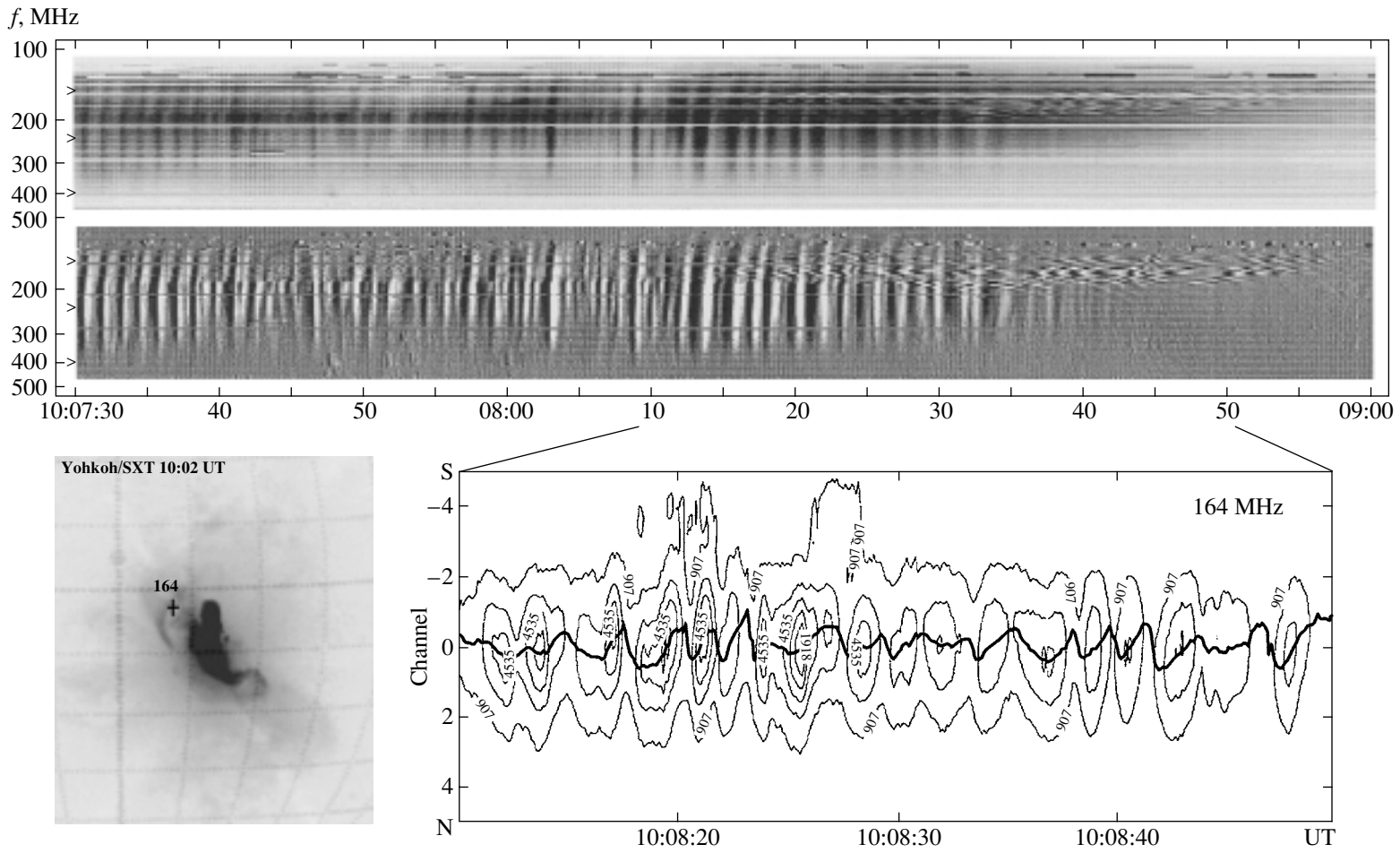

Fig. 4. Dynamical spectrum of the periodic type III outbursts (reminiscent of pulsations) in event of October 25, 1994 over the entire range of the ARTEMIS spectrograph, 100–500 MHz (intensity is shown in the upper spectrum and the derivative of the signal in the lower spectrum), with zebra-pattern structure visible at 135–210 MHz. The lower right panel shows simultaneous S–N contours of the radio brightness distribution at 164 MHz (NRH). The bold line passing through the centers of the sources shows their spatial drift. The lower left panel shows the position of the 164 MHz radio source (marked by a plus) superposed on an X-ray image of the flare (Yohkoh/SXT, the A1.1 thin filter), demonstrating that this radio source is located outside the bright flare region.

In this event, zebra structure was observed at frequencies between 210 and 130 MHz against the background of the type III outbursts, which drifted from 400 to 150–125 MHz (Fig. 4, ARTEMIS data).

We would like to point out certain key features in Fig. 4, which enable us to understand the overall dynamics of the event. The initial frequency of the type III outbursts oscillates between 300 and 450 MHz, with a period that smoothly grows from 10–15 min at the onset to roughly 30–35 min at the end of the series of type III outbursts. This may be associated with slow MHD fluctuations in the region in which the fast particles are accelerated. The low-frequency limit where the drift of the type III outbursts ceases also fluctuates asynchronously with the high-frequency initial frequency: this limit dropped to approximately 125 MHz between 10:08:12 and 10:08:30 UT. A clear sign of a new perturbation is provided by an abrupt break in the frequency drift between 10:07:38 and 10:07:57 UT, with the drift settling at a frequency of 170 MHz. Three seconds later, zebra-pattern structure appears beginning at precisely this frequency and occupying frequencies down to 140 MHz. Over an eight-minute interval, the zebra structure expanded from 130 to 210 MHz, and the type III outbursts gradually disappeared (their intensity and frequency range smoothly decreased). When the zebra structure is most fully developed, at 10:08:17–10:08:24 UT, it is possible to distinguish up to 17 emission stripes, with the frequency separation between the stripes slowly growing from 1.7 MHz at 140 MHz to roughly 2.2 MHz at 170 MHz. The polarization of the radio emission of the zebra structure and the type III outbursts was moderate (25–30%), with the maximum polarization corresonding to the zebra structure without type III outbursts at the end of the eighth minute. The right-circular polarization in the source above the trailing spot of southern polarity corresponds to a predominance of the ordinary wave.

The lower right panel of Fig. 4 shows contours of the one-dimensional S–N radio-brightness distribution at 164 MHz (NRH). The maximum brightness corresponds to the center of a zebra-pattern stripe after approximately 10:08:33 UT or a type III outburst before this time. The solid line passing through the source centers shows the spatial drift of the sources at a fixed frequency. First and foremost, we note that the positions of the sources of type III emission and zebra structure coincide (in both the N–S and E–W directions; i.e., in a disk). It is noteworthy that the type III sources drift in the direction S → N (at the beginning of the spectrum), while the sources of pure zebra structure (at the end of the spectrum) drift in the opposite direction, N → S. In all the zebra-pattern absorption stripes, the drift of the source is the same as for the type III outbursts (for example, at time 10:08:33.4 UT).

The vertical scale for the one-dimensional S–N radio-brightness distributions in Fig. 4 is presented in terms of the number of spatial channels for the Nancay radio interferometer. At 164 MHz at this time, the first channel in the S–N direction corresponds to approximately 3.2′. Therefore, the full widths at half maximum of the sources of both the zebra structure and the type III outbursts are, on average, 1.5 channels (about 4.8′); the maximum spatial-drift rates are $>90\,000$ km/s ($\approx 170\,000$ km/s for the type III outbursts). Since these are projected onto the disk, the real source drift rates will always be $>10^{10}$ km/s (close to the speed of light). Thus, the observed size of the source is essentially the size of the active region, and the observed drift rate can be supplied only by fast (relativisitic) particles. Similar zebra-structure drift rates were obtained earlier for event June 5, 1990 [23].

Let us note another important fact: the zebra structure forms several humps with changing signs of the frequency drift, with the sign changes correlating with changes in the sign of the spatial drift of the source. Negative frequency drift corresponds to the type of drift occurring in type III outbursts, and changes in the sign of the source drift are observed at times when the frequency drift changes sign (for example, at times 10:08:32 and 10:08:36.5 UT). These data enable us to explain the frequency band occupied by the zebra structure in the dynamical spectrum (see the Discussion below).

In interplanetary space, the URAP experiment on the Ulysses satellite detected one type III outburst at 10:10 UT at frequencies below 1000 kHz, due to a beam of electrons accelerated at the onset of the flare.

2.5. Centimeter wavelengths

We selected several dozen cases of zebra-pattern structure and fiber bursts in four events at 2.6–3.8 GHz and one case at 5.2–7.6 GHz. In all cases, the zebra-structure and fiber-burst radiation was strongly polarized near 3 GHz, but weakly polarized at 5.2–7.6 GHz. The most saturated fine structure was observed in the centimeter-wavelength outbursts of April 15, 1998, October 29, 2000, and April 21, 2002. This last event occurred at the limb. Via a comparison of the times when zebra structure was manifest with the positions of radio sources indicated by Nobeyama heliograph observations at 17 GHz and with the development of the flare in the 195 Å line indicated by SOHO/EIT (and SOHO/MDI magnetogram) data for the first two events, it was possible to determine that the ordinary mode dominated in the radiation. Our observations show that

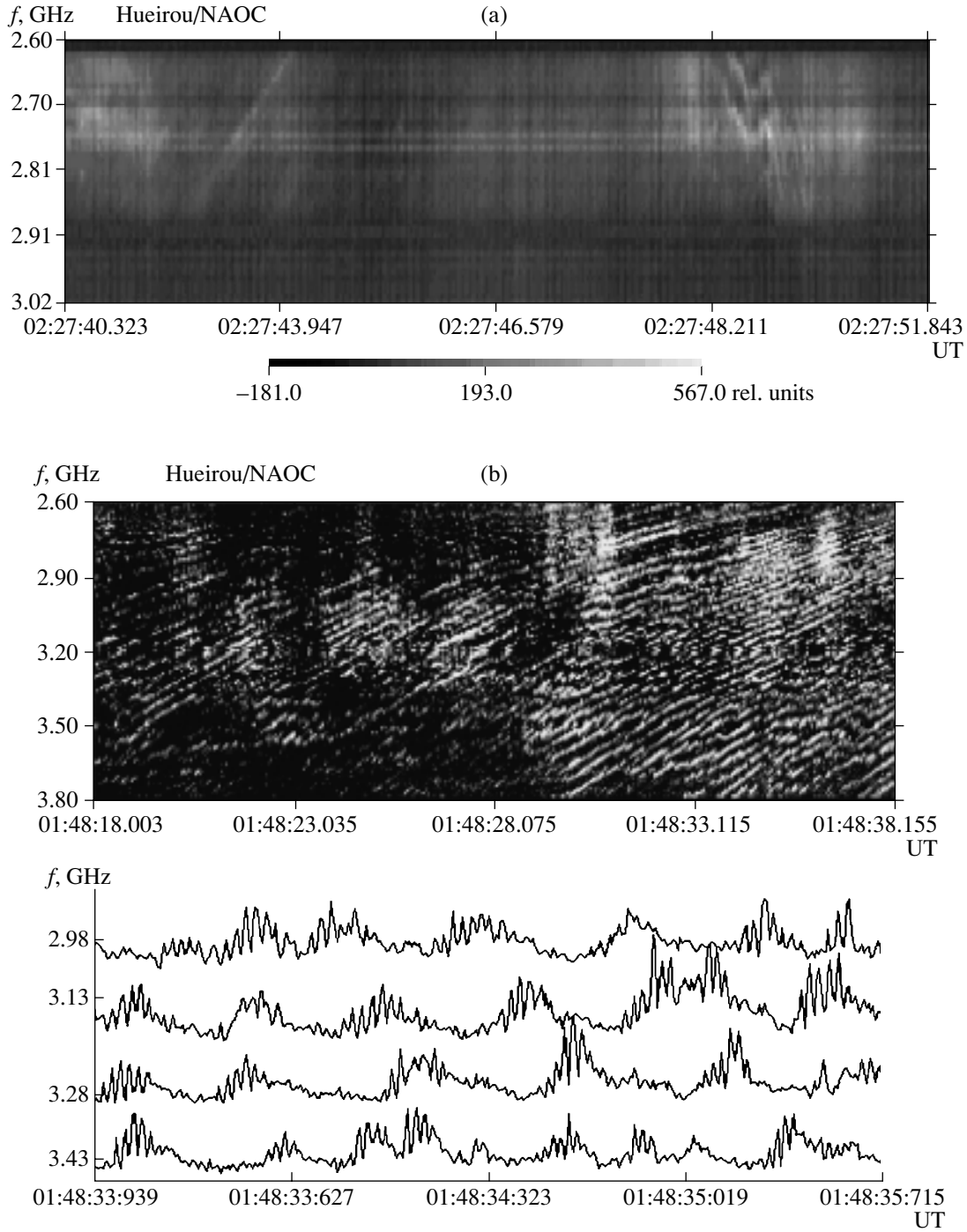

Fig. 5. (a) Zebra structure in a fiber burst in event of October 29, 2000 observed in right-circular polarization by the NAOC spectropolarimeter (Beijing). (b) Zebra structure in event April 21, 2002. The upper panel shows the spectrum in left-circular polarization, in which 34 stripes whose frequency separation grows smoothly with frequency can be distinguished. The lower panel shows profiles of the intensities at four fixed frequencies.

all the variety of zebra structure and fiber bursts known for decimeter and meter wavelengths is also characteristic of events at centimeter wavelengths. Figures 5a and 5b depict the development of zebra structure and fiber bursts in events of October 29, 2000 and April 21, 2002, which were most rich in fine structure. In event of October 29, 2000, series of zebra-pattern structures were present in a pulsating regime for approximately 30 minutes following the maximum of the flare. Each series had a duration of

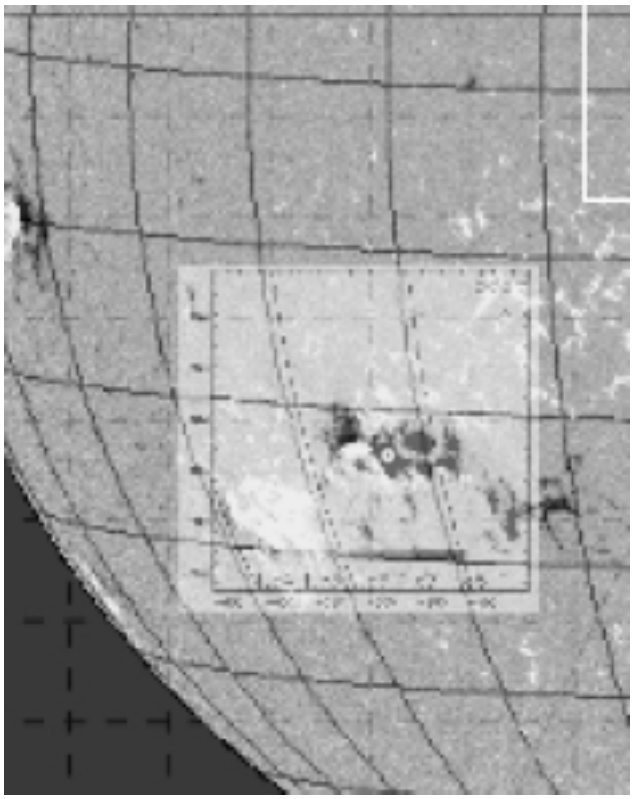

Fig. 6. Position of the center of the radio source in event of October 29, 2000 at 17 GHz, shown by a light circle against the background of the S-polarity magnetic field recorded on the SOHO/MDI magnetogram, on which the radio brightness distribution derived from the Nobeyama radio-heliograph data is superimposed.

about 2–3 s and three to five zebra-pattern stripes, with various frequency drifts; a fiber burst with a constant negative drift sometimes accumulated in the zebra structure (Fig. 5a).

Event of October 29, 2000 was associated with a 2B M4.4 Hα flare in the active region NOAA 9209 (S25E35). The position of the center of the radio source at 17 GHz is shown in Fig. 6 by a light circle against the background of the S-polarity magnetic field detected by the SOHO/MDI magnetogram, on which the radio-brightness distribution obtained using the Nobeyama Radio Heliograph is superimposed. The radio source is located above the S-polarity magnetic field, so that right-circular polarization corresponds to the O mode of the radio emission.

In event of April 21, 2002 (Fig. 5b), up to 34 zebra-pattern stripes can be distinguished in the spectrograph band, 2.6–3.8 GHz, with a barely perceptible growth in the frequency separation between the stripes from 27 MHz at 2.8 GHz to 43 MHz at 3.7 GHz. The moderate degree of left-circular polarization increased appreciably with time and frequency, even within a single series of zebra structures with a duration of 20 s.

A detailed analysis of the multi-channel time profiles shows that the radiation level in the dark bands between bright stripes can be lower than the background level for the flare (see the profiles at several fixed frequencies in the lower panel of Fig. 5b). Thus, the presence of dark stripes is not associated only with an absence of bright stripes (in emission), but with genuine absorption of the centimeter-wavelength background. In this connection, the main characteristic of the zebra structure is the frequency separation between neighboring peaks in emission and absorption, Δf_{ea}, rather than the frequency separation between stripes of emission, Δf_s. While the latter is determined (for example, in double-plasma-resonance models for the zebra structure) by mutual variations of the plasma frequency and electron-gyrofrequency harmonic with height in the corona, Δf_{ea} is determined directly by the mechanism that forms the stripes in emission and absorption. Despite the variety in the zebra-pattern stripes, the mean value of $\Delta f_s/f$ for all the events is about 60–80 MHz at 2.6–3.8 GHz, while the mean value of the parameter $\Delta f_{ea} \approx 30$–40 MHz for both zebra structure and fiber bursts. Fiber bursts do not always display regularity in frequency, and most often each fiber burst is manifest as a weak outburst; but the parameter Δf_{ea} testifies to a related origin for the bands associated with zebra structure and fiber bursts.

The main parameters of the zebra structure and fiber bursts for five events are collected in the Table. The parameters $\Delta f_s/f$ and $\Delta f_{ea}/f$ grow with frequency, clearly in connection with the growth of the magnetic field. The parameter $\Delta f_b/f$ decreases with frequency, which corresponds to a decrease in the size of the radio sources in the lower corona. Only the quantity $\Delta f/f$ remains nearly constant. In four events, the radio fine structure corresponded to the ordinary mode.

3. DISCUSSION

Four radio events with zebra structure and fiber bursts at meter wavelengths were closely associated with flares of various magnitudes or type II outbursts (due to shocks in and CMEs), but, in all the events, the maximum energy release occurred high in the corona as a result of magnetic reconnection. The polarization of the radio emission was moderate in all events, and corresponded to the ordinary mode in three cases.

Parameters of the zebra structure in five events

Date Time (UT)	f, MHz Frequency, MHz	Flare Coordinates	$\Delta f_s/f$	$\Delta f_{ea}/f$	$\Delta f_b/f$	$\Delta f/f$	Magnetic polarity	Sign of the polarization Mode
1998-05-02	35	3B X1.1	0.0036	0.0024	0.88	0.0035	S(N)	LR
14:41	20–70	S15, W15						?
1994-10-25	175	1N C4.7	0.015	0.006	0.4	0.0049	S	R
10:08	100–500	S09W12						O
1999-07-28	360	1B M2.3	0.014	0.006	0.22	0.0054	N	L
08:15	45–520	S15E03						O
1998-09-23	360	3B M7.1	0.064	0.032	0.3	0.014	N	L
08:00	100–700	N18E09						O
2000-10-29	3000	2B M4.4	0.033	0.015	0.16	0.0059	S	R
02:20	1000–3800	S25E35						O

Note: $\Delta f_s/f$ is the relative frequency separation between the zebra stripes; $\Delta f_{ea}/f$ is the relative frequency separation between stripes in emission and absorption; $\Delta f_b/f$ is the relative frequency bandwidth of the fine structure in the spectrum; $\Delta f/f$ is the relative instantaneous frequency bandwidth for a single stripe of emission.

3.1. Event of May 2, 1998

The braids of fibers shown in Fig. 1 strongly resemble similar structures observed earlier at higher frequencies (200–250 MHz) and discussed in [9, 24, 25]. However, these latter structures were repeated multiple times over the entire decay phase of a flare (over more than an hour). They are associated with whistler instabilities in a small magnetic trap that has formed between shock fronts moving away from a magnetic-reconnection X point during the prolonged process of reestablishing the magnetic structure after a CME.

We can see ejections in various directions in five frames in the 195 Å line (SOHO/EIT), but two of these are most prominent: one toward the north from the main flare and the other toward the southwest (a slowly moving front). This is suggestive of a perturbation (shock front) moving toward the observer. It may be that the source of the fiber braids is associated with this shock front, and is located in a narrow trap between the front and the leading edge of a CME: the braids are observed over only three minutes during the type II outburst, and the frequency drift of the main braid is determined by the motion of the shock front with a speed of $\approx$2200 km/s.

Fast particles accelerated in the shock front were captured in this narrow trap (with a width of several thousand kilometers). As a result of the "bounce" effect—the motion of these particles between the two maxima of the magnetic field (in the shock front and the leading edge of the CME)—a conical velocity distribution was formed, giving rise to a periodic conical whistler instability.

It is shown in [8] that the speed of the CME is slightly higher than the speed of the shock front. The increasing distance between the two can explain the smooth expansion of the main braid during the drift toward lower frequencies. In general, the shock front probably propagates at some angle to the magnetic field. In this case, the magnetic field and density of the shock front should have an oscillatory structure. This may be the origin of the presence of a number of other fragments of fiber braids and zebra stripes at higher frequencies, whose sources are located further behind the shock front.

The whistlers propagate in the direction of propagation of the shock front, but the group velocity of the whistlers cannot exceed $\sim 10^8$ cm/s, providing an explanation for the appreciably lower frequency-drift rate of the fibers within the main braid. Thus, these unusual braids of fibers are most likely a manifestation of the simultaneous propagation of a shock front and a CME in the corona with different speeds.

3.2. Event of July 28, 1999

The observations testify that new, hot loops rose before the two intervals of zebra-pattern structure, and that the radio sources were located above these loops (Fig. 2). It is obvious that the frequency bandwidth of the fine structure was determined by the

vertical size of these new flare loops in the corona. The radio sources were located above regions with northern magnetic polarity, and the left-circular polarization of the radio emission corresponds to the ordinary wave.

The inverse position of the absorption stripes in the zebra structure (from the high-frequency edge of the stripes of emission) over roughly ten minutes during the decay phase of the flare provides important information for theoretical models of the fine structure. A similar inverse position of fiber-burst absorption bands was considered in [13], where it was shown that, in this case, we observe radiation at the difference frequency $\omega_l - \omega_w = \omega_t$ as a result of the decay process $l \to t + w$. This variation in the interaction between plasma waves and whistlers is probably associated with variations in the magnetic-field gradient in the source, as are quite expected in regions of magnetic reconnection high in the corona.

The continuous transition between fiber bursts and zebra-pattern stripes (and vice versa) suggests a single origin for these two types of structure, especially since their main parameters are the same. In this connection, we note that the zebra-structure model of LaBelle *et al.* [16] is not able to explain the continuous transition between zebra structure and fiber bursts, since only the stability of a point source is considered. It is not clear what variations of the positions of the absorption stripes should be expected in this model, or what their origin would be.

3.3. Event of September 23, 1998

Analysis of all the available observational data for these event show that fine structure was observed simultaneously with the appearance of new, hot magnetic loops, and that the frequency bandwidth occupied by the fine structure in the spectrum (280–450 MHz) could realistically be determined by the extent of these new loops in the corona.

Again, the data demonstrate that the zebra structure consists not only of stripes of emission, but also of stripes with appreciable absorption, which are sometimes even dominant. For this reason, and also in connection with the simultaneous radiation from zebra structure, fiber bursts, and rapid pulsations, it is difficult to explain the zebra structure in this event with the new model of [16]. It is quite realistic to expect the excitation of electrostatic plasma waves and whistlers trapped by fast particles in new flare loops, but the formation of small inhomogeneities (solitons consisting of ion–acoustic waves) is not obvious (most importantly, the condition $T_e \gg T_i$), and is simply postulated by LaBelle *et al.* [16]. There also remain doubts about the applicability of the model of [16] to meter wavelengths, when the wavelength becomes comparable to the size of the inhomogeneities ($\lambda \sim L$), since $\lambda \ll L$ is a condition for applying geometrical optics to write the eiconal conditions (Eqs. (4) and (5) in [16]).

3.4. Event of October 25, 1994

In this brief event, the source of the zebra structure was located above an active region, as is shown in Fig. 4. A more detailed analysis of the X-ray frames (Yohkoh/SXT) is carried out in [22], where it is shown that there was additional brightening outside the main flare region as a result of magnetic reconnection involving the main flare loop and previously existing loops high in the corona.

The bandwidth of the zebra structure is probably determined by the distance in the corona between the magnetic-reconnection X point above a flare loop and a point high in the corona displaying shear between the rising flare loops and large-scale transequatorial loops, visible in the Yohkoh/SXT frames. Evidence supporting this picture is provided by the coincidence in the spectrum of the low-frequency boundary of the zebra structure and the frequency at which the drift of the type III outbursts ceases after about 10:08:35 UT (Fig. 4).

The spatial drift of the zebra-pattern structure at 164 MHz was toward the south, opposite to the drift of the type III outbursts. In our picture, this testifies that beams of fast electrons accelerated below in a flare current sheet (and responsible for the periodic type III outbursts) are reflected from a region with magnetic-field shear (where the new magnetic reconnection with the X point began). The reflected particles have a conical velocity distribution, generating plasma waves and whistlers, whose interactions give rise to the zebra structure at the corresponding frequencies.

However, the sign change of the spatial drift of the zebra structure that is correlated with the sign change of the frequency drift provides evidence that the spatial drift at a fixed frequency does not represent a real shift in the source position, but instead a shift in the energy maximum in the interval of heights associated with the radiation at that frequency (due to the velocity scatter for the rapid particles) and along the surface of equal density. Such a drift is quite plausible in a whistler model. The reflected particles should display conical anisotropy, and the whistlers should be excited in the anomalous Doppler resonance, when the particles and waves propagate in the same direction. In this case, the whistlers propagate downward with the group velocity, consistent with the positive frequency drift of the zebra-pattern stripes. The scattering of the whistlers on fast particles (quasi-linear effects) deforms the

distribution function: the longitudinal velocities are decreased while the transverse anisotropy grows, and the excitation of whistlers gradually switches to the normal Doppler resonance, when the particles and waves propagate in opposite directions and the group velocity of the whistlers gradually turns upward (this effect is considered in more detail in [11]). This switch in regime is completed at times of sign changes of the frequency drift of the zebra-pattern stripes, which coincide with times of sign changes of the spatial drift of the sources.

Even sharper shifts of the source center occurs at times corresponding to the transition to the zebra absorption stripes. In this case, no particle velocities can explain a shift by about 1.5 channels (each 3.2′) over one-third of a second (for example, at 10:08:41.3–10:08:41.7 UT), which yields a shift velocity of about $2c$, where c is the speed of light. In this case, we do not observe real motion, but instead a shift in the position of the maximum continuum radiation of the source, which indeed shifts by this amount (more than 4′) toward the southwest (above the maximum of the SXR flare in Fig. 4).

Thus, although the centers of the type III outbursts and zebra structure nearly coincide, the emission is radiated by different particles moving in different directions. In the case of the type III outbursts, these are beams of particles propagating from the acceleration region, which is the upper part of a flare current sheet at the height where $f_{Pe} \approx 450$ MHz; in the case of the zebra structure, these are particles reflected from a region with shear, at heights corresponding to the minimum frequency of the type III outbursts, where $f_{Pe} \approx 125$ MHz). The abrupt perturbation that partially stopped the frequency drift of the type III outbursts at 10:07:37–10:07:58 UT shows us the position in the corona of a new magnetic-reconnection X point (where $f_{Pe} \approx$ 170 MHz). At these heights, there was a partial capture of particles from the type III outburst beams, forming a new magnetic cloud (an island above the X point). The size of this new magnetic cloud between the X point and the magnetic-field shear determined the beginning of the frequency range of the zebra structure. Over a minute (10:08–10:09 UT), the whistlers gradually spread downward to levels where $f_{Pe} \approx 210$ MHz.

The large transverse size of the source suggests that the whistler instability developed over the entire width of a level of constant density above the active region, but the emission maximum could be appreciably shifted from the center of the continuum maximum along this level.

In our whistler model, each stripe of the zebra pattern is associated with an isolated whistler wave packet. The periodicity of the stripes most likely reflects periodicity in the instability due to the quasi-linear interactions between the whistlers and fast particles (periodicity in the deformations of the distribution functions). Periodicity in the injection of fast particles and the "bounces" of the particles in the magnetic trap will lead to additional periodicity in the observed phenomena. No obvious trap was observed in this event, and we can see a surprising coincidence in the number of type III outbursts at 10:08–10:09 UT (24) and the number of zebra-pattern stripes along the time axis. Quasi-linear effects lead to additional modulation along the zebra stripes. Such effects operate only when the particles and waves (whistlers) do not diverge in space. The smooth shift of the hump with the sign change of the frequency drift is due precisely to the diffusion of whistlers in rapid particles, when the time when the resonances are switched (see above) does not occur simultaneously at all frequencies (heights in the corona), but instead with a modest delay between frequencies, equal to the time for the diffusion at each level in the corona (for more detail, see [11]).

The double-plasma resonance model proposed in [26] to describe this phenomenon cannot explain the observed effects, even the number of zebra stripes in the observed frequency interval. For example, if we adopt, not some hypothetical distributions with a high density and magnetic field, but more realistic distributions, such as a double Newkirk model above the active region and a dipolar magnetic field whose scale height is much smaller than the density scale height, this model predicts only ten stripes in the observed frequency range of 135–170 MHz instead of the observed 18 stripes, with harmonic numbers s from 10 to 20, as was shown in [27]. Most importantly, instead of a smooth growth in the frequency separation between the stripes with increasing frequency (from 1.7 to 2.2 MHz), the model predicts a sharp growth from 2.5 to 7 MHz. Even larger discrepancies with the observations are obtained for other models (for example, density distributions that obey the barometric formula and magnetic fields that correspond to the model of [28]). Note that, while the field model of [26] is quite realistic (it was derived based on numerous radio observations), a barometric density distribution cannot be applied to magnetic loops with plasma parameters $\beta \ll 1$, since the barometric formula corresponds to a density distribution in a gravitational field with constant temperature and without a magnetic field.

This radio event was typical from the point of view of the activity in interplanetary space, where the groups of type III outbursts make a nearly smooth transition to a single large kilometer-scale type III outburst.

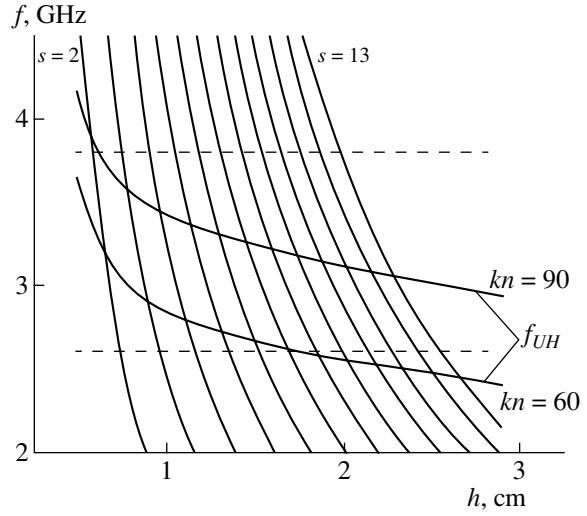

Fig. 7. Dependence of the plasma frequency and gyrofrequency in the magnetic-field model of Dulk and MacLean [28], which is derived from radio data ($B(\mathrm{G}) = 0.5(R/R_s - 1)^{-1.5}$, $1.02 \le R/R_s \le 10$), and a model with a Newkirk electron density multiplied by kn. The horizontal dashed lines delineate the range of the NAOC radio spectrograph, 2.6–3.8 GHz.

3.5. Centimeter Wavelengths (Events of October 29, 2000 and April 21, 2002)

Since the zebra-pattern structure and fiber bursts display similar spectral characteristics, we will consider both structures to be manifestations of whistlers in the radio source, due to their interactions with electrostatic plasma waves, $l + w \to t$, with both waves being excited by the same fast particles in hot flare loops, which have an anisotropic conical loss distribution. The computations of [29] show a growth in the whistler increment with the temperature of the background plasma in the flare region, with the growth in the cyclotron decay being compensated by the decrease in the whistler frequency with the maximum increment to $0.1\omega_{Be}$. The mean duration of a series of zebra structures and fiber bursts was about two seconds, and the propagation of whistlers without damping over this time places a constraint on the whistler increment of $< 0.5\ \mathrm{s}^{-1}$. This constraint can be used to estimate the magnetic-field strength in the region in which the flare is generated. Electron temperatures in the range 2–20 MK yield magnetic fields of $B = 125$–190 G for regions in which the electron density is $(8$–$18) \times 10^{10}\ \mathrm{cm}^{-3}$. These rough estimates coincide with estimates derived from the frequency-drift rate of the fiber bursts observed at the same time at these same frequencies, based on the formula $B = 15.43(\ln f - 3)^{-2} df/dt$ [30], which was obtained for a 60-fold Newkirk model and a whistler frequency of $\omega_w = 0.1\omega_B$. If we estimate the magnitude of B in the new model of LaBelle *et al.* [16], assuming that $\Delta f_s \sim 0.02 f_{Be}$, we obtain for $\Delta f_s = 80$ MHz implausibly high values $B \approx 1500$ G for regions close to the photosphere.

An alternative model based on the generation of plasma waves at the upper-hybrid frequency ω_{UH} under the conditions appropriate for the double plasma resonance was also considered. We can see from Fig. 7 that the main inadequacy of this model is associated with the increase in the frequency separation of the emission stripes Δf_s with increasing frequency: the model predicts an increase from 60 MHz at 2.7 GHz to ~450 MHz at 3.8 GHz, which is not generally observed. Usually, the frequency separation only slightly increases with frequency. In this connection, the example of the zebra structure shown in Fig. 5b is noteworthy, since it shows that the double-plasma-resonance model is not able to explain the presence of simultaneous emission in 34 stripes with virtually identical intensities in the range 2.6–3.8 GHz. At the same time, this situation is quite realistic in a whistler model, where strict periodicity of the stripes is specified by the whistler-excitation mechanism itself—fluctuations in the instability under the action of quasi-linear effects—independent of the models for the density and magnetic field in the corona.

The frequency profiles in Fig. 5b demonstrate rapid pulsations in the bright zebra-pattern stripes with a well defined period of 30 ms. Thus, these new observations support the conclusions of [31] that zebra structure at centimeter wavelengths always has fine spikelike structure, which can be explained in a natural way in whistler models for zebra structure.

Like the large number of zebra-pattern stripes, the stable appearance of series of zebra structures in a pulsating regime cannot be understood in the new model [16], since this model predicts a strong dependence for the frequency separation and the number of zebra stripes on the parameters of the inhomogeneities, while we observe only a very small growth in the frequency separation with increasing frequency. LaBelle *et al.* [16] can theoretically explain any parameters of zebra structure, but the parameters of inhomogeneities such as propagating ion–acoustic waves cannot remain so similar over a wide range of frequencies (interval of heights) over extended periods of time; i.e., the spectrum of the stripes would be expected to blend into the continuum.

Thus, new data on zebra structure and fiber bursts at centimeter wavelengths testifies that they have similar structures to those observed at meter wavelengths. A unified model for zebra structure and fiber bursts involving whistlers can yield realistic values for the magnetic-field strength $B \approx 160$ G at a plasma level of about 3 GHz. Using realistic dependences for

the electron density and magnetic field, the double-plasma-resonance model for zebra structure predicts a frequency dependence for the frequency separation between stripes that is much stronger than is observed.

4. CONCLUSION

We have analyzed several of the most recent zebra-structure events using a multi-faceted approach to study the flare processes based on all available new data from the Yohkoh, SOHO, and TRACE satellites. Zebra structure and fiber bursts are observed at frequencies from 20 to 6500 MHz. The radiation of electrostatic plasma waves at higher frequencies is probably suppressed in the dense flare plasma. The main relative spectral parameters and degree of circular polarization of zebra structure and fiber bursts are nearly identical. The relative width of the zebra-pattern stripes in emission varies very little with frequency ($\approx 0.003-0.005$); the radio emission corresponds to the ordinary mode.

New data on zebra structure and fiber bursts at centimeter wavelengths shows that they are similar to the corresponding structures at meter wavelengths. A unified model for zebra structure and fiber bursts involving whistlers can yield realistic values for the magnetic-field strength $B \approx 160$ G at a plasma level of about 3 GHz. Using realistic dependences for the electron density and magnetic field, the double-plasma-resonance model for zebra structure predicts a frequency dependence for the frequency separation between stripes that is much stronger than is observed.

Fine structure was observed simultaneous with the ascent into the corona of new, hot magnetic loops, and the frequency range occupied by the fine structure in the dynamical spectrum is determined by the extent of these new loops in the corona. The continuous transition from fiber bursts to zebra structure and vice versa testifies to a single nature for these two structures. All the main properties of the emission and absorption stripes can be explained in a model involving interactions between electrostatic plasma waves and whistlers. The mechanism at double plasma resonance can be invoked to account for the large-scale bands in the radiation whose duration is comparable to that of the entire event, as was shown, for example, in [10] for the EEL filament oscillating for two hours. A detailed analysis of the behavior of the radio sources corresponding to individual zebra stripes in event 1994-10-25 at meter wavelengths shows that analogous studies at centimeter wavelengths require new positional observations of the radio-source dynamics obtained on instruments such as the CCPT simultaneous with spectral observations.

ACKNOWLEDGMENTS

The Phoenix-2 spectral data were kindly presented by P. Messmer, and the ARTEMIS-IV data (Greece) by A. Hilaris. The author thanks K.L. Klein for the preparation and discussion of the Nancay radioheliograph data, M. Poquerusse for the ARTEMIS spectrograph data (Meudon), and P. Zlobec for the data from the Trieste Astronomical Observatory polarimeter. The SOHO and TRACE data were obtained from the SOHO and TRACE databases (EIT, LASCO), and the X-ray data from the Yohkoh/SXT database (ISAS, Japan). The author is grateful for support from the Paris Observatory in Meudon (the project CNRS 4994) and the Chinese Academy of Sciences (NAOC, Profs. Q. Fu and Y. Yan). This work was supported by the Russian Foundation for Basic Research (project no. 02-02-116201).

REFERENCES

1. C. Slottje, *Atlas of Fine Structures of Dynamic Spectra of Solar Type IV-dm and Some Type II Radio Bursts* (Utrech Observatory, 1981).
2. A. Krüger, *Introduction to Solar Radio Astronomy and Radio Physics* (Reidel, Dordrecht, 1979).
3. G. P. Chernov, L. V. Yasnov, Y. Yan, and Q. Fu, China Astron. Astrophys. **1**, 525 (2001).
4. J. Kuijpers, *Collective Wave-Particle Interactions in Solar Type IV Radio Sources* (Utrech Univ., 1975).
5. V. V. Zheleznyakov and E. Ya. Zlotnik, Solar Phys. **44**, 461 (1975).
6. L. Mollwo, Solar Phys. **116**, 323 (1988).
7. R. M. Winglee and G. A. Dulk, Astrophys. J. **307**, 808 (1986).
8. O. A. Mal'tseva and G. P. Chernov, Kinemat. Fiz. Neb. Tel **5**, 44 (1989).
9. G. P. Chernov, Astron. Zh. **66**, 1258 (1989) [Sov. Astron. **33**, 649 (1989)].
10. G. P. Chernov, A. K. Markeev, M. Poquerusse, *et al.*, Astron. Astrophys. **334**, 314 (1998).
11. G. P. Chernov, Astron. Zh. **73**, 614 (1996) [Astron. Rep. **40**, 561 (1996)].
12. G. P. Chernov, Astron. Zh. **53**, 1027 (1976) [Sov. Astron. **20**, 582 (1976)] .
13. G. P. Chernov, Astron. Zh. **67**, 126 (1990) [Sov. Astron. **34**, 66 (1990)].
14. V. G. Ledenev, M. Karlicky, Y. Yan, and Q. Fu, Solar Phys. **202**, 71 (2001).
15. M. Karlicky, M. Barta, K. Jiricka, *et al.*, Astron. Astrophys. **375**, 638 (2001).
16. J. LaBelle, R. A. Treumann, P. H. Yoon, and M. Karlicky, Astrophys. J. **593**, 1195 (2003).
17. H. S. Sawant, M. Karlicky, F. C. R. Fernandes, and J. R. Cecatto, Astron. Astrophys. **396**, 1015 (2002).
18. Y. Leblanc, G. A. Dulk, I. H. Cairns, and J.-L. Bougeret, J. Geophys. Res. **105**, 18215 (2000).

19. A. T. Altyntsev, R. A. Sych, V. V. Grechnev, *et al.*, Solar Phys. **206**, 155 (2002).
20. Z. Ning, Y. Yan, Q. Fu, and Q. Lu, Astron. Astrophys. (2002, in press).
21. H. Aurass, B. Vršnak, A. Hofmann, and V. Ruždjak, Solar Phys. **190**, 267 (1999).
22. P. K. Manoharan, L. van Driel-Gesztelyi, M. Pick, and P. Demoulin, Astrophys. J. **468**, L73 (1996).
23. G. P. Chernov, K.-L. Klein, P. Zlobec, and H. Aurass, Solar Phys. **155**, 373 (1994).
24. G. Mann, K. Baumgaertel, G. P. Chernov, and M. Karlicky, Solar Phys. **120**, 383 (1989).
25. G. P. Chernov, Pis'ma Astron. Zh. **23**, 949 (1997) [Astron. Lett. **23**, 827 (1997)].
26. V. V. Zaitsev and E. Ya. Zlotnik, in *Proceedings of the Scientific Conference "Active Processes in Sun and Stars"* (NIIRF SPbGU, St. Petersburg, 2002), p. 257 [in Russian].
27. G. P. Chernov, in *Proceedings of the Conference "Modern Problems of Solar and Stellar Activity"* (NIRFI, Nizhni Novgorod, 2003) [in Russian].
28. G. A. Dulk and D. J. McLean, Solar Phys. **57**, 279 (1978).
29. L. V. Yasnov, G. P. Chernov, Y. Yan, and Q. Fu, *Proceedings of the 10th European SPM, Solar Variability: from Core to Outer Frontiers, Prague, 2002*, ESA SP-506, 791 (2002).
30. O. Elgarøy, *Intermediate Drift Bursts* (Oslo Univ., Oslo, 1982), Rep. No. 53.
31. G. P. Chernov, Y. Yan, and Q. Fu, Astron. Astrophys. **406**, 1071 (2003).

Translated by D. Gabuzda

Astronomy Reports, Vol. 48, No. 10, 2004, pp. 871–875. Translated from Astronomicheskiĭ Zhurnal, Vol. 81, No. 10, 2004, pp. 956–960.

The Helioseismological CORONAS-F DIFOS Experiment

N. I. Lebedev[1], V. D. Kuznetsov[1], V. N. Oraevskiĭ[1], J. Staude[2], and R. I. Kostyk[3]

[1] *Institute of Terrestrial Magnetism, the Ionosphere, and Radio Wave Propagation, Troitsk, Russia*

[2] *Astrophysical Institute, Potsdam, Germany*

[3] *Main Astronomical Observatory, Kiev, Ukraine*

Received October 21, 2003; in final form, March 15, 2004

Abstract—The CORONAS-F DIFOS experiment continues the CORONAS-I studies started in 1994, devoted to investigations of solar global oscillations. CORONAS-F was launched July 31, 2001. Variations in the intensity of the solar radiation are measured in the six spectral intervals of the multi-channel photometer: 350, 500, 650, 850, 1100, and 1500 nm, with the bandwidths being about 10% of the central wavelength of each interval. The scientific goals of the experiment, a brief description of the instrument, and observational conditions are presented, as well as the data processing techniques. The first observations of the low-order p eigenmodes of the solar oscillations are presented for various wavelength ranges. A decrease in the relative amplitudes with observing wavelength is indicated. The amplitude ratios for various spectral ranges agree well with those detected earlier in ground- and space-based experiments.

1. INTRODUCTION

The CORONAS-F DIFOS experiment is intended for observations of global solar oscillations and studies of the internal structure of the Sun. The DIFOS multi-channel photometer can detect variations in the intensity of the solar radiation simultaneously in six spectral intervals from the ultraviolet to the near-infrared.

CORONAS-F was launched into a circular high-latitude (82.5°) orbit with an altitude of about 500 km on July 31, 2001. The anticipated long-term, high-quality measurements of the intensity of the solar radiation are aimed at realizing the following research program: to determine the frequencies, amplitudes, and phases of the p modes of solar oscillations at frequencies from 0 to 5 mHz; to study variations in oscillation parameters associated with the 11-year solar-activity cycle; to try to detect the g modes of solar oscillations; to use the oscillation properties derived to construct a model for the internal structure of the Sun; and to determine the distributions of the sound speed, density, and rotational velocity in the solar interior.

The first stage of the DIFOS experiment was accomplished using the CORONAS-I satellite, launched into a high-latitude, circular orbit with an altitude of about 500 km on March 4, 1994. Continuous series of data on variations of the intensity of the solar radiation in three spectral intervals were obtained over 52 days using the DIFOS photometer [1–3]. The spectral properties of 50 eigenmodes of the solar oscillations have been determined and studied. The frequencies and amplitudes of the identified p modes were consistent with the results of ground-based observations. The amplitude ratio for green and red wavelengths was in agreement with that detected earlier in ground-based observations [4]. Frequency splitting for the p modes attributed to the solar rotation was observed.

2. THE CORONAS-F DIFOS PHOTOMETER

By taking into consideration the results obtained with the CORONAS-I DIFOS photometer and SOHO studies on helioseismology (the SPM photometers of the helioseismological VIRGO [5] device are rather similar to the DIFOS photometer), we were able to significantly modernize the photometer for CORONAS-F. The main aspects of this modernization are that the photoreceivers have a considerable increase in sensitivity (by more than an order of magnitude), and the spectral range is almost twice as broad, with the number of spectral channels also being increased from three to six.

The CORONAS-F DIFOS photometer (a block diagram is presented in Fig. 1) can detect the radiation intensity simultaneously at 350, 500, 650, 850, 1100, and 1500 nm, with the corresponding bandwidths being 10% of the central wavelengths, forming

1063-7729/04/4810-0871$26.00

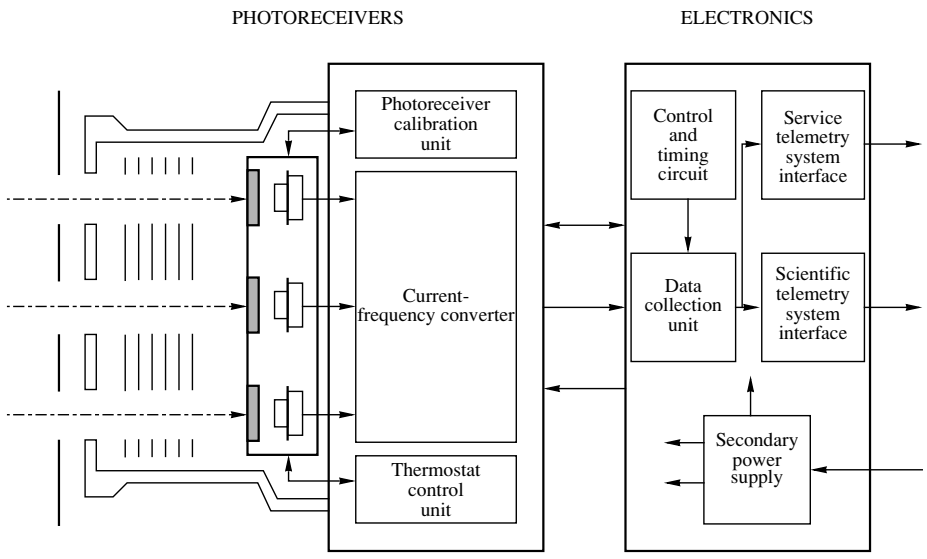

Fig. 1. Block diagram for the multi-channel photometer.

a broad spectral interval from the ultraviolet to the near-infrared.

The relative resolution of the DIFOS photometer is 2×10^{-6} of the total solar radiation intensity, the time spacing is 33.5 s, the field of vision is $-2°$, and the accuracy with which the optical axis can be pointed toward the center of the solar disk is no worse than $10'$ (this is determined by the attitude control of the spacecraft); there is no spatial resolution capability (i.e., only low-order oscillation modes with $l \leq 3$ can be studied). Figure 2 shows the relative arrangement of the spectral channels of the CORONAS-F DIFOS photometer and the SOHO detectors.

The DIFOS photometer can be used to (1) study the wavelength dependence of the relative power of the solar oscillations and test theoretical calculations indicating a significant increase in the oscillation power in the ultraviolet [6]; (2) study the interaction of acoustic and thermal waves in the upper layers of the convective zone (observations at 1500 nm, which represents the emission radiated from the deepest layers of the photosphere, are most interesting in this regard); (3) study variations in the solar irradiance, and separate the contributions of sunspots, faculae, the network, and other manifestations of solar activity to variations of the solar constant [7]; (4) determine the relations between the parameters of eigenmodes (spectrum, power, lifetime, frequency variations) and various manifestations of solar activity, and find the conditions necessary to excite the oscillations; (5) study the relationship between the observed parameters of the global oscillations and the 11-year solar-activity cycle; (6) determine the distributions of the sound speed, density, and rotational velocity in the solar interior.

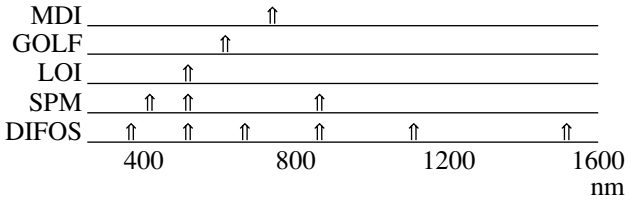

Fig. 2. Comparative arrangement of the DIFOS spectral channels and the spectral channels of the SOHO helioseismological devices: (MDI) Michelson Doppler Imager of the solar oscillations, (GOLF) Global low-degree velocity, (LOI) Luminosity Oscillation Imager, and (SPM) SunPhotoMeter.

3. MEASUREMENTS AND DATA PROCESSING

The CORONAS-F DIFOS photometer has been operating since August 22, 2001. The intensity data are transmitted through two independent telemetric channels, and lost data can be recovered via a comparison procedure. Our analysis of the data has verified their high quality. Data are lost during no more than 10% of the operational time of the photometer and are mainly associated with failures in the telemetry link.

Figure 3 shows the solar radiation intensity in all the measurement channels as a function of time

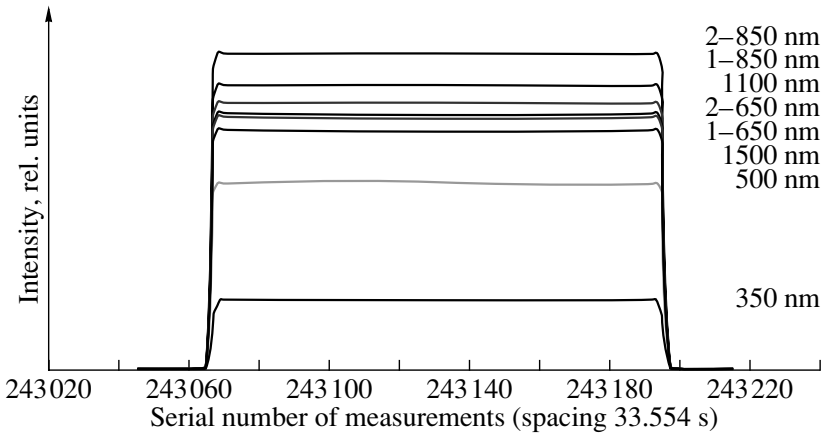

Fig. 3. Intensity of the solar radiation in eight channels (six spectral ranges) of the DIFOS photometer (December 1, 2001, orbit 1878).

for orbit 1878. The data form a series of equidistant measurements with a time spacing of 33.554 s and a duration of about an hour, followed by a half-hour break due to the spacecraft being in the Earth's shadow. The zero intensities at the beginning and end of each record correspond to the shadowed portion of the satellite orbit. The different intensities during the illuminated portion of the orbit are associated with the different sensitivities of the photoreceivers and different transparencies of the spectral filters in different channels.

Figure 4 presents the photometer data detected in one measurement channel for the illuminated portion of the orbit. The observed trend is due to scattering of the solar light reflected from the Earth's surface. An analytical curve approximating the trend is also shown.

Figure 5 shows variations of the solar radiation intensity used to examine the amplitude spectra at 0–5 mHz, obtained via a cleaning of the recording presented in Fig. 4 (subtraction of the photoreceiver dark currents, subtraction of trends, normalization, etc.). The variations of the solar radiation intensity in this plot do not exceed 0.02% of the total flux.

4. AMPLITUDE SPECTRA FOR VARIOUS WAVELENGTH RANGES

Figure 6 presents the amplitude spectrum obtained at 650 nm for a two-day observation. Similar spectra were obtained for the other photometer channels. The analysis of these spectra enables the reliable identification of p modes for orders $l = 0, 1$, and 2. We have detected 10–15 harmonics in the range 2.5–3.5 mHz for each similar spectrum. The numbers above the spectral peaks indicate l and n for each oscillation mode. The mean relative amplitudes of the oscillations vary from 10^{-6} to 10^{-5}, depending on the wavelength of the observations.

We used the two-day amplitude spectra to determine the wavelength dependence of the relative amplitudes. The mean amplitudes of the p modes at 2.5–3.5 mHz were calculated for each such spectrum. These amplitudes were then averaged over all two-day spectra. We applied this procedure to all six wavelength bands observed. Figure 7 presents the wavelength dependence of the relative amplitude derived using this procedure. There is a significant increase in the oscillation amplitudes at short wavelengths, in agreement with theoretical calculations.

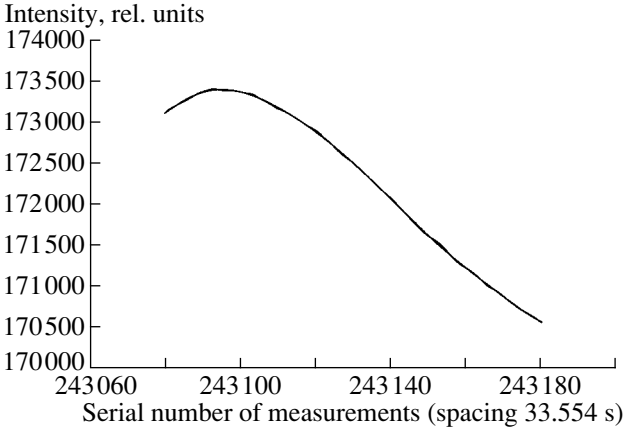

Fig. 4. Solar radiation intensity at 350 nm for the illuminated portion of the orbit. The trend is due to light reflected and scattered in the Earth's atmosphere. An analytical curve approximating the trend is also shown.

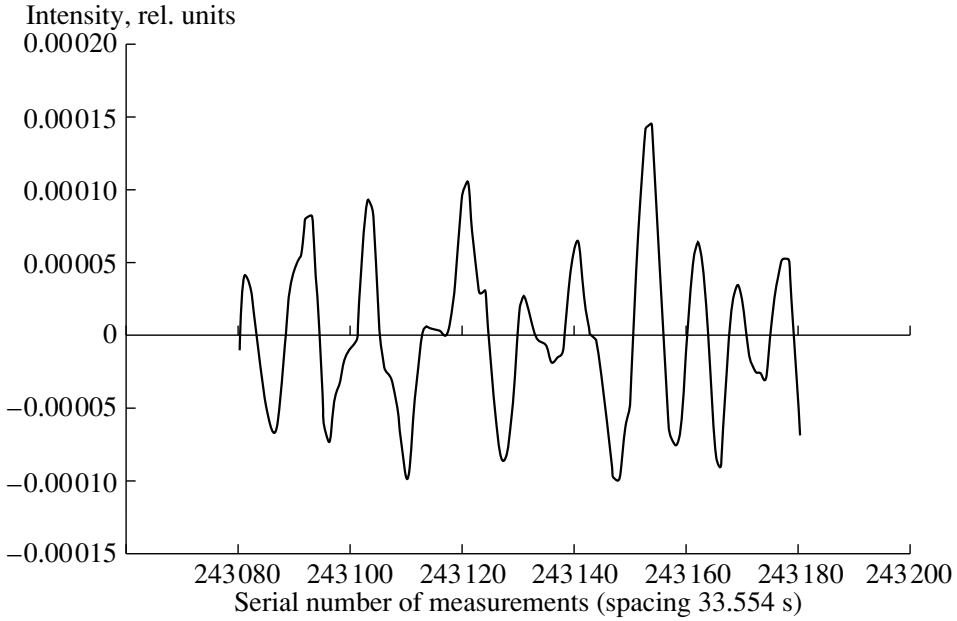

Fig. 5. Variations of the solar radiation intensity at 350 nm.

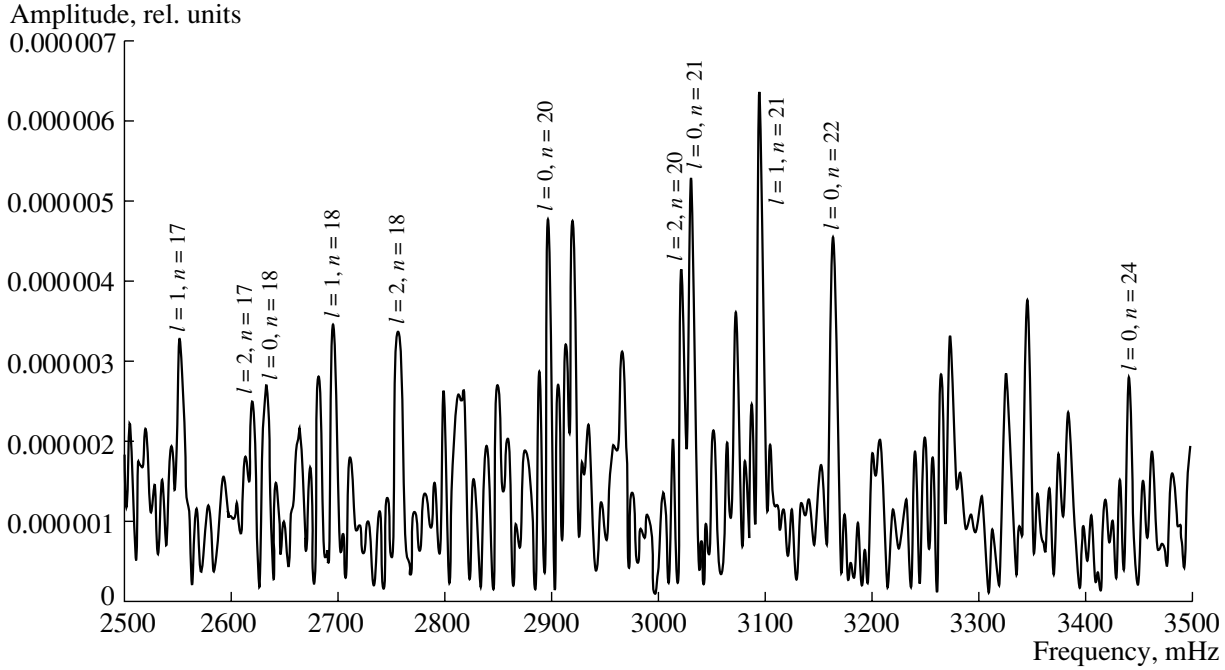

Fig. 6. Amplitude spectrum for 5-minute solar oscillations detected in two days of data from the CORONAS-F DIFOS photometer obtained at 650 nm (November 29–30, 2001, orbits 1831–1860).

A comparison with ground-based [4] and SOHO [5] observations also shows a close agreement.

The amplitude of each individual mode is wavelength dependent, and is determined by the depth in the solar atmosphere at which the radiation at this wavelength is formed. The dependence obtained provides an observational basis for testing theoretical

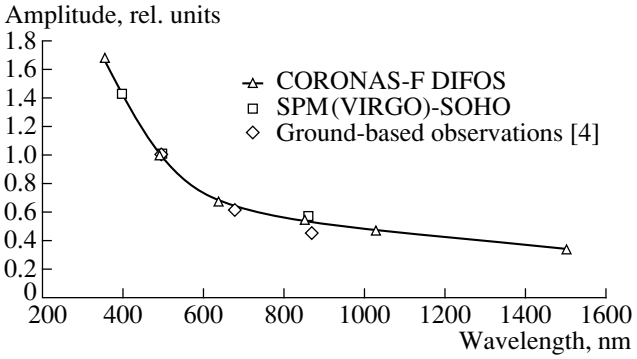

Fig. 7. Relative amplitude of the solar oscillations as a function of wavelength.

calculations and modeling the conditions for the formation of radiation at wavelengths of 350–1500 nm.

5. CONCLUSIONS

The CORONAS-F DIFOS multichannel photometer provides extensive information on the global solar oscillations at wavelengths of 350–1500 nm near the maximum of the current (23rd) solar-activity cycle. The data obtained enable us to construct the amplitude spectra for p modes at 2.5–3.5 mHz and to identify the oscillation harmonics. The wavelength dependence of the relative amplitude shows an appreciable increase in the oscillation amplitudes in the ultraviolet. This dependence agrees well with ground-based data obtained at Tenerife (Spain) in 1984–1986 and with SOHO observations (in overlapping bands). To date, the DIFOS experiment has accumulated data continuously over more than two years, and the results are being extended and refined as new scientific information becomes available.

REFERENCES

1. K.-H. Hasler, Y. D. Zhugzhda, N. I. Lebedev, *et al.*, Astron. Astrophys. **322**, L41 (1997).
2. N. I. Lebedev, V. N. Oraevsky, Y. D. Zhugzhda, *et al.*, Astron. Astrophys. **296**, L25 (1995).
3. V. N. Oraevsky, Y. D. Zhugzhda, I. M. Kopaev, *et al.*, The DIFOS Experiment: Observations of Solar Eigen Oscillations aboard the CORONAS-I Satellite, CORONAS Inform., No. 8 (1994).
4. A. Jimenez, P. L. Palle, T. Roca Cortes, and V. Domingo, Astron. Astrophys. **193**, 298 (1988).
5. C. Frohlich, Bo. N. Andersen, T. Appourchaux, *et al.*, Solar Phys. **170**, 1 (1997).
6. V. N. Oraevsky and I. I. Sobelman, Astron. Lett. **28** (6), 401 (2002).
7. K. Pflug, V. N. Obridko, K. Arlt, and N. I. Lebedev, Astron. Astrophys. **317**, 925 (1997).

Translated by V. Badin